Mechanical alloying Ti-Ni based metallic compounds as negative electrode materials for Ni-MH battery

Xianda Li

SPIM

Thèse de Doctorat

Thèse N° 256 **Année 2015**

école doctorale sciences pour l'ingénieur et microtechniques

UNIVERSITÉ DE TECHNOLOGIE BELFORT-MONTBÉLIARD

THÈSE

Présentée pour obtenir le grade de

Docteur de l'Université de Technologie de Belfort-Montbéliard en Science des Matériaux

Par

Xianda LI

Mechanical alloying Ti-Ni based metallic compounds as negative electrode materials for Ni-MH battery

Soutenance publique le 9 Février 2015

Jury:

M. Rabah HAMZAOUI, HDR	Reviewer	ESTP, Paris
M. Bernard NORMAND, Prof.	Reviewer	INSA de Lyon
M. Nicolas MARTIN, Prof.	Examiner	Institute FEMTO-ST, ENSMM, Besançon
M. Ghislain MONTAVON, Prof.	Examiner	Université de Technologie de Belfort-Montbéliard
M. Salim-Mourad CHERIF, Prof.	Examiner	Université Paris 13
M. Omar ELKEDIM, HDR	Supervisor	Université de Technologie de Belfort-Montbéliard

Acknowledgements

As this thesis work is mainly done in the MN2S unit of FEMTO-ST supported by China Scholarship Council and UTBM in the framework of UT-INSA (2011), my thanks first go to all the collaborating parties which made this work possible at all.

I would express my greatest gratitude to my thesis supervisor Prof. Omar Elkedim, who has been extremely supportive along this journey of scientific research, where difficulties are only the stairs for one to climb up. It is not only the knowledge I could learn from him, but also the confident and cheerful attitude toward obstacles is of great inspiration to me on this road of science in the future. I would also like to say thanks to him for his patience to guide me through all this work.

I am very thankful for Mr. Hamzaoui and Mr. Normand to take the time to be the reviewers and help improve the thesis.

I feel honored to have Mr. Martin, Mr. Montavon, and Mr. Cherif to be present in the jury of the thesis defense session.

I owe greatly to Prof. Fermin Cuevas, who has contributed a lot to this work in the first place. I was already lucky enough to meet him in person in a young researchers' conference after I had read several of his journal articles, but he also kindly accepted my request to help me work shortly in the lab ICMPE at Paris. Today I can still recall his detailed teachings from mathematic equations to data manipulation using software during my stay in the lab. His enthusiasm toward science will always be my inspiration and spur me to pursue excellence when doing science.

I must appreciate the collaboration with Monsieur Jurczyk, Monsieur Rémi Chassagnon, and Monsieur Nowak on co-completing this work. Contribution from you is invaluable to this work.

I have received countless help from many nice working fellows, peers from different labs. They are: Virginie Moutarlier, Marine Ponthieu, Amina Lamraoui, and my colleagues in the lab, Saoussen Tria, Yangzhou Ma, Zhao Zhang and Liwu Huang.

My thanks go to all the people that make my life in France a wonderful experience. Especially Madame Nathalie Sementery, thank you for giving me the opportunity to have all the pleasant time with your students in the university. It will always be the good memory to recall.

Finally, I owe to my parents at the moment, who have been the ones standing firmly behind my back, despite the physical distance between us. Like always, during my study in France, they have been giving me wise advice and are always helping me to be a better person.

Table of Contents

Introduction

World Health Organization (WHO) reports that air pollution was linked to the death of seven million people globally in 2012. The Environmental Protection Ministry in China reported that, only three of the 74 Chinese cities monitored by the central government met the national standard for healthy air in 2013. Air pollution has become "the world's largest single environmental health risk" according to WHO. While the discussion regarding depletion of energy on earth continues, environmental hazard has already cut its short. As a matter of fact, one quarter of China's electricity is generated from hydroelectric, wind and solar sources, but demand of energy is still too overwhelming with current pace of development of the country. Unfortunately, the gap is being filled by fossil fuels. Today, the crucial role that green energy plays can never be stressed enough in this era of modern civilization.

However when one investigates further, it appears that clean energy itself is in fact not hard to find, such as solar, wind, geothermal heat, tides, waves, rain and so on, but the problem lies in the fact that energy generation and consumption are not always concurrent. Therefore, the ultimate goal is the method of storing energy, which can be used in an on-demand manner.

When it comes to energy storage, one naturally thinks of battery, as the most common form of energy is electricity. By definition, battery is a device consisting of one or more electrochemical cells that convert stored chemical energy into electrical energy. Compared to fossil fuels that release their chemical energy by combustion, batteries have lower specific energy. However the advantage of batteries is the higher energy conversion efficiency. It is also where fuel cell comes into play, as it converts the chemical energy stored in the fuel to electricity instead of heat. Therefore it has lower impact on environment. Moreover, if the fuel cell uses hydrogen as its fuel, the by-product is only water and some heat. Ideally the footprint to environment in this case is negligible.

Nickel-Metal Hydride (Ni-MH) battery is the type of fuel cell, in which hydrogen is used as the fuel. Furthermore, unlike traditional fuel cells, the principle reaction in Ni-MH batteries is reversible, meaning that the battery can be recharged after discharge (use). When the battery is charged, it is equivalent to say that hydrogen is stored (as metal hydride in the case of Ni-MH battery). The hydrogen production and consumption both take place in Ni-MH battery itself. While charging requires energy, it can very easily source energies that are normally not unreliable or inconsistent, but store them for on-demand use.

Patented in 1986 by Stanford Ovshinsky, Ni-MH batteries have been put to use on many applications nowadays. Besides the batteries on portable devices, they play also a major role on electric powered vehicles, competing with Li-ion batteries on the market. In general, Ni-MH batteries are attributed to exhibit properties such as high energy density, high rate capacity, good overcharge/overdischarge capability, low maintenance, and environment friendliness. Nevertheless, much room is left for improvement, especially in regard to specific energy density.

The materials used for the negative electrode of Ni-MH batteries are key to battery performance, namely discharge capacity, high-rate capability (both charging and discharging), initial activation, cycle life, self-discharge rate. A metal hydride is expected to form when the negative electrode is charged. Therefore the amount of hydrogen a material can store is reasonably the first to evaluate as the candidate for the negative electrode material of Ni-MH batteries. In the same time, a method to store hydrogen is also a hot research topic. Since metal hydride is one approach besides high pressure gas, liquid hydrogen and other solid storage solutions, it may appear confusing to some due to overlapping study area covered by researchers from both fields.

There are mainly three kinds of metal hydrides under extensive research currently, Mg-based metal hydride, complex hydride and intermetallic compounds. Each has their own advantages and drawbacks. Mg-based metal hydrides are known for high hydrogen-storage capacity by weight and low cost [1], but the hydrides are found to be too stable, having poor desorption kinetics for reversibility. The hydrogen content in complex hydrides reaches as high as 18 wt% ($LiBH_4$). The limitation of those hydrides comes as well as kinetic and thermodynamic problem upon desorbing hydrogen. Another class is intermetallic compounds, which has a long study history and a big family, classified as AB_n (n = 5, 2, 1, 0.5) type. $LaNi_5$-based (AB_5) alloys exhibit excellent electrochemical performance, and have been put to commercial production in a large scale nowadays. But like it is said before, a higher specific energy density for these batteries is desired, however cannot be met due to its low theoretical hydrogen capacity (372 mAh/g [2]).

As an intermetallic compound, Ti-Ni based alloys have also been studied as the candidates for hydrogen storage materials. Both TiNi and Ti_2Ni are capable to store hydrogen. TiNi can crystallize to a typical CsCl type structure known as austenitic phase as well as martensitic phase due to its polymorphic property. It was found that TiNi can react with hydrogen by solid-gas and absorbs up to 1.4 hydrogen atoms per formula unit at room conditions [3]. In an electrochemical reaction, 230 mAh/g was measured by Gutjahr et al. [4]. Element doping and substitution for TiNi were reported to improve the electrochemical performance as the negative electrode materials for Ni-MH batteries [5-7]. Ti_2Ni is the other Ti-Ni type alloy found to store hydrogen. It was reported to be able to form $Ti_2NiH_{2.9}$ (~500 mAh/g) in a gaseous hydrogen absorption reaction [8]. However, highest capacity reached in an electrochemical reaction for Ti_2Ni was 280 mAh/g in the first cycle, and dropped to less than 100 mAh/g after 50 cycles [9]. Element substitution was

tried on Ti_2Ni to improve performance [10-12]. In the meantime, non-conventional alloying approaches are also combined with element substitution to improve the alloy properties, including mechanical alloying, solid sintering and so on. Mechanical alloying are frequently applied to produce nanocrystalline alloys of metal hydrides, when it is found that nano-structured materials enhance absorption and desorption kinetics significantly [13, 14].

The objective of this study is to using new method and element substitution to improve the Ti-Ni system with the aim to improve its hydrogenation properties, hence the performance of its application for Ni-MH batteries. The thesis studied the Ti-Ni system with element doping or substitution, using mechanical alloying as the synthesis method.

In chapter 1, the Ni-MH system as a new form of energy storage and its relationship with fuel cell is presented, followed by an introduction of the Ti-Ni system and its recent research as the negative electrode material for Ni-MH batteries. Mechanical alloying as the synthesis method in this study is introduced with examples of its application on the research of Ni-MH battery materials.

Chapter 2 gives the experimental details used in this study. This includes the principle of the synthesis method high energy ball milling (HEBM), and the parameters applied for the synthesis. The structural characterization of the milled method and the instruments for the characterization are introduced. The measurement methods for hydrogen capacity are explained, which include both solid-gas reaction with the hydrogen and the electrochemical approach. Density functional theory (DFT) calculation is explained with the introduction of its application CASTEP (Cambridge Serial Total Energy Package).

In Chapter 3, we have mechanically alloyed two groups of samples to study the Mg effect on the Ti-Ni alloy, namely $(TiNi)_{1-x}Mg_x$ and $(TiH_2)_{1.5}Mg_{0.5}Ni$. The study includes its structural influence and hydrogenation

properties of the milled sample, with DFT calculation to explain the experimental results.

Chapter 4 studies the Zr influence on the milling of Ti_2Ni, where a composition of $Ti_{2-x}Zr_xNi$ is synthesized in comparison with milled Ti_2Ni.

Chapter 5 has concluded the main points of this study, which concerns the products preference of milling Ti-Ni based powders, and the hydrogenation properties of the obtained structures were summarized. The chapter gives also a perspective view of the current research as how it can be continued for further investigation in the search of ideal materials for the negative electrode of Ni-MH batteries.

Chapter 1 Overview of Ni-MH System and Ti-Ni Alloys as Hydrogen Storage

This chapter gives a brief review from principles of Ni-MH system to the batteries on the market. As the basis of the present study, Ti-Ni alloy system is introduced and discussed, including the Ti-Ni phase diagram, TiNi, and Ti_2Ni studies as the negative electrode materials in Ni-MH batteries.

1.1 Fuel cell and Ni-MH secondary battery

The concept of fuel cell is usually compared to traditional use of fuels, in which the chemical energy stored is released in the form of heat. While as a matter of fact, the first fuel cell model appeared as early as 1838, when Welsh physicist and barrister William Grove published a letter in the December 1838 edition of *The London and Edinburgh Philosophical Magazine and Journal of Science* about the development of his first crude fuel cells. In the model of William Grove, the chemical energy of the fuel (hydrogen) is consumed via electrochemical reaction instead of combustion. This has resulted in tremendous improvement in energy efficiency. According to the World Energy Council, the maximum theoretical efficiency of internal combustion engines is about 50%, while theoretically the efficiency of a fuel cell is 83% (dG/dH of hydrogen oxygen reaction). Despite the relative long history of fuel cell concept, fuels are mainly consumed in the manner of burning in reality, and the energy is converted mostly to heat. Fuel cell is still an advanced technology people strive for today.

Ni-MH secondary battery is one particular genre of fuel cell, which displays three major features that distinguish it from other traditional fuel cells: 1) The fuel for the cell is hydrogen. In principle, hydrogen is consumed through a hydrogen oxidation reaction. This is also the reason why Ni-MH secondary battery is categorized into fuel cell. 2) Although Ni-MH battery does not need fuel supply as in traditional fuel cell, they however are charged using electric power, during when energy is stored in the form of hydrogen. 3) As a secondary

battery, the discharge process in Ni-MH battery is reversible. Figure 1-1 presents the principle of the Ni-MH battery. As hydrogen is cycled within the cell, it can be seen how it is different from traditional fuel cell, since the charging process does not involve the input of hydrogen from outside sources.

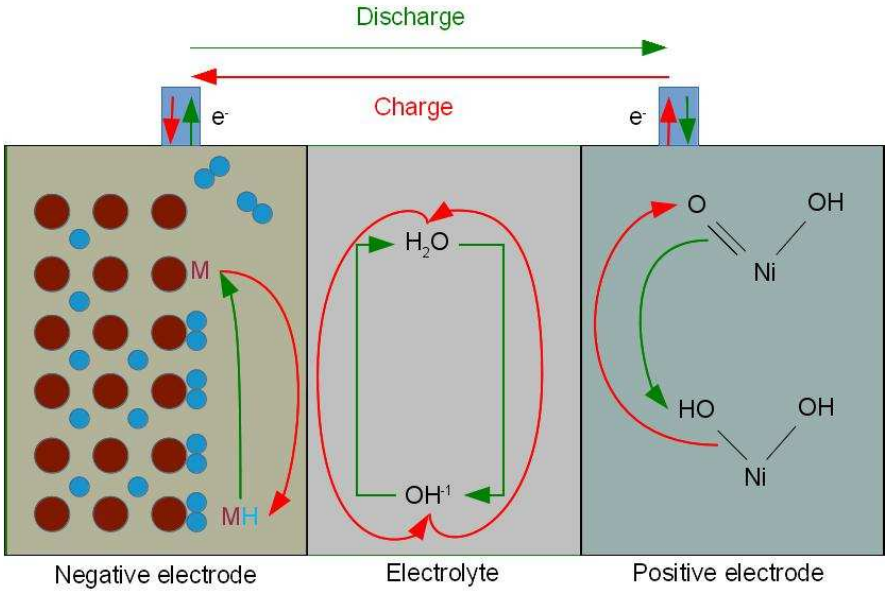

Figure 1-1 Scheme of a working Ni-MH battery

Ni-MH battery uses nickel(II) hydroxide as its positive electrode and the negative electrode is a hydrogen-absorbing alloy, which is also the essential part of a Ni-MH battery. M stands for the metal/alloy that is able to store hydrogen and ideally form a hydride. The recent development of Ni-MH battery has replaced the largely obsolete nickel-cadmium cell in the market with dominating advantages over the latter, while competing with lithium-ion cell. The specific energy for NiMH cells ranges from 75 W·h/kg to 100 W·h/kg, which is absolutely an improvement to the energy densities of NiCd, and approaches that of a lithium-ion cell. The volumetric energy density of NiMH is around 300 W·h/L, significantly better than NiCd and similar to lithium-ion cell.

A single NiMH cell operates at 1.2 V, and the batteries are very common for AA batteries. Examples of commercial NiMH batteries on the market today are listed in Table 1-1.

Table 1-1 Examples of commercial Ni-MH batteries (Size AA) performance today

	No. 1	No. 2	No. 3
Usage scenario	High power consumption	Low power consumption	All
Life cycle	~500	~3000	~2100
Self-discharge	~85% after 1 year	~75% after 5 years	~70% after 5 years
Capacity	2550 mAh	1000 mAh	2000 mAh

1.1.1 Metal hydride as a hydrogen storage material

The negative electrode is the key to a favored performance of NiMH batteries, since it is where metal hydride forms. A high weight hydrogen percentage in the material is the first sign of a potential candidate for the negative electrode in NiMH batteries. In the meantime, this kind of material is also considered and sought for to be ideal for hydrogen storage material.

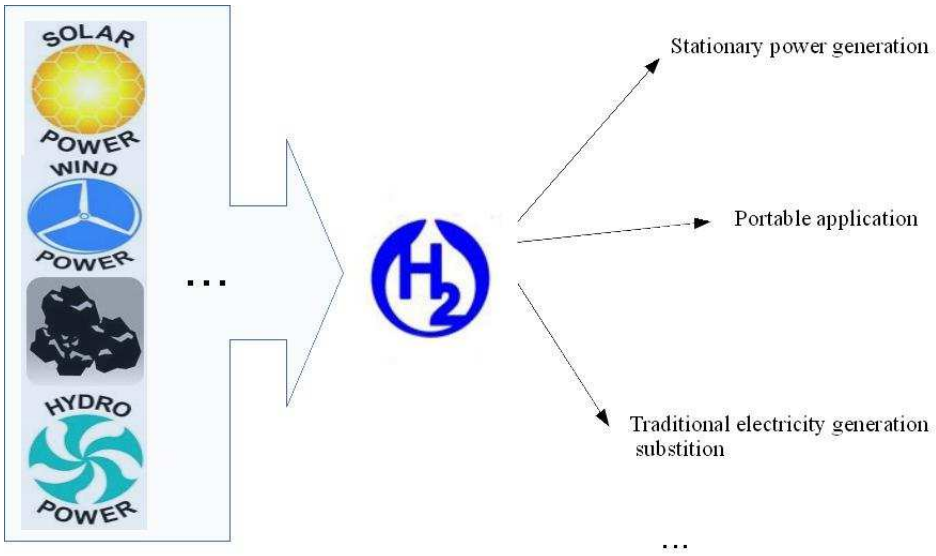

Figure 1-2 Hydrogen as the secondary energy

Hydrogen storage method is one of the ultimate solutions for clean energy, because as a secondary energy, hydrogen can be the carrier of energy, which is illustrated in Figure 1-2.

Several approaches are used to store hydrogen, which can be classified as physical storage or chemical storage. The physical storage method includes high pressure hydrogen gas, liquid hydrogen, while the chemical approach means to form hydride with the storing material.

1.1.1.1 Hydrogen in compressed gas

The physical storage approach is the most direct way, which is to store hydrogen gas under high pressure. As it depends on the actual application (stationary or vehicular), pressure in hydrogen tanks ranges from 35 MPa to 70 MPa.

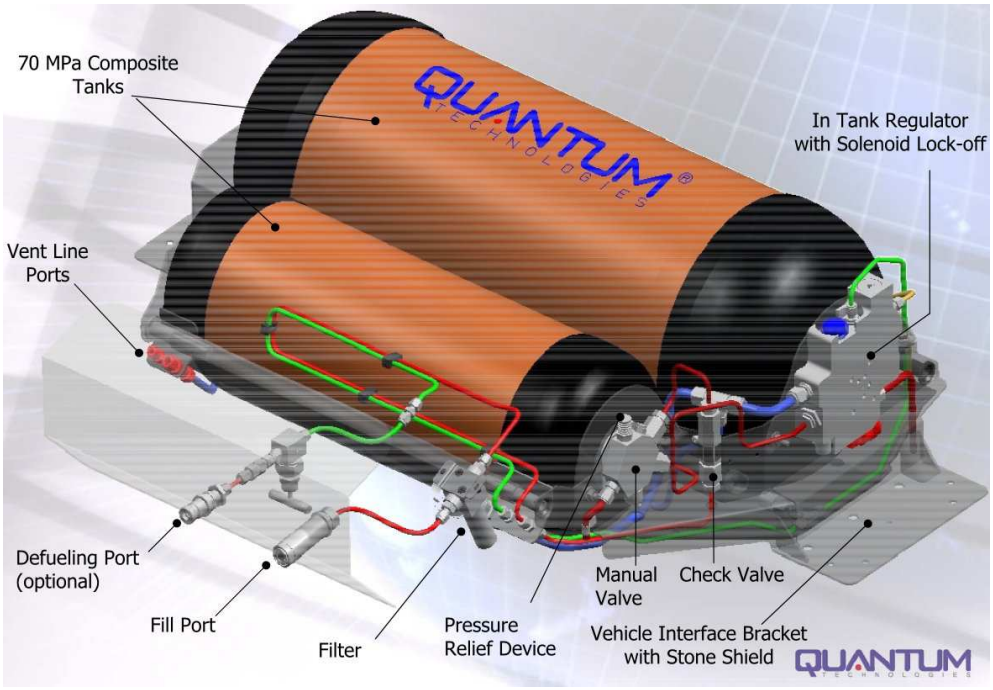

Figure 1-3 Commercialized compress hydrogen tank

The major advantage of this method is its fast filling-releasing simplicity. Due to the demand of higher energy density, its technical simplicity advantage is

however not true anymore, as high pressure requires appropriate material support. There are several safety concerns about hydrogen stored in vessels, including hydrogen embrittlement of metals at room temperatures, temperature rise in hydrogen fast filling, and potential risks like diffusion, deflagration, and detonation after hydrogen leakage are introduced. Especially for the use in vehicles, the challenge in both energy density and safety is overwhelming. These challenges lead to high cost materials for the building of the tanks, which need to be not only strong but light in the same time. Carbon fiber, among many other used fibers, is currently deployed, but the price has been the drive to further develop this method into broader use. Figure 1-3 shows the structure of a compress hydrogen tank from commercial company.

1.1.1.2 Liquid hydrogen storage

Liquid hydrogen is naturally an improved method from gas formed hydrogen in the aim with increasing energy density. The volumetric density of compressed gas form and liquid form of hydrogen are 0.030 kg/L and 0.070 kg/L for respectively under ~ 70 MPa.

Under atmosphere pressure, H_2 needs to be cooled down to at least 33 K to exist in liquid form. Therefore, high pressure can compensate the low temperature requirement. However, the problems with liquid hydrogen tanks include hydrogen boil-off, the energy required for hydrogen liquefaction, volume, weight, and tank cost. Hydrogen liquefaction consumes about 30% of the lower heating value of hydrogen, in comparison with hydrogen compression which requires 5% of lower heating value of hydrogen up to 35 MPa. New approaches for liquefaction are needed to lower these energy requirements and thus the cost of liquefaction. Hydrogen boil-off must be treated for efficiency and safety considerations. Insulation that is usually required for the liquid

hydrogen tanks need to be improved for system gravimetric and volumetric capacity reasons too.

1.1.1.3 Hydrogen storage in solid state

Nowadays, the chemical approach draws extensive interests, which is basically the solid state storage method. Figure 1-4 shows how solid state storage of hydrogen leads in volumetric density among the three major solutions.

Figure 1-4 Hydrogen storage methods volumetric comparison [22]

There are many approaches for solid state storage of hydrogen, such as metal hydrides [15], amine borane complexes [16], carbon nanotubes [17], metal-organic frameworks [18] and so on. For metal hydrides approach alone, researches have been reaching different directions, including Ti-Ni based [5], Mg-Ni based [19], La-Ni based [20], complex hydrides [21] etc. The current situation can be clearly seen from Figure 1-5, which compares the gravimetric energy density and volumetric energy density from different hydrogen storage sources, as well as the equivalent hydrogen energy density of common fossil fuels. In the figure, it shows that compressed hydrogen is the least favored concerning volumetric density, whereas liquid hydrogen dominates when gravimetric density is solely what is sought for. As for metal hydrides, volumetric density needs improvement for the ones that work under high

temperature condition, however if lower temperature condition is met, the gravimetric density becomes too low. Neither of these two kinds has yet reached the goal of U.S. DOE (Department of Energy). Energy density is crucial especially to the portable applications, EV (Electric Vehicle) as the best example. The advantage of solid state hydrogen storage can be seen clearly in Figure 1-5. So far, there has not been a solution that achieves the U.S. DOE target.

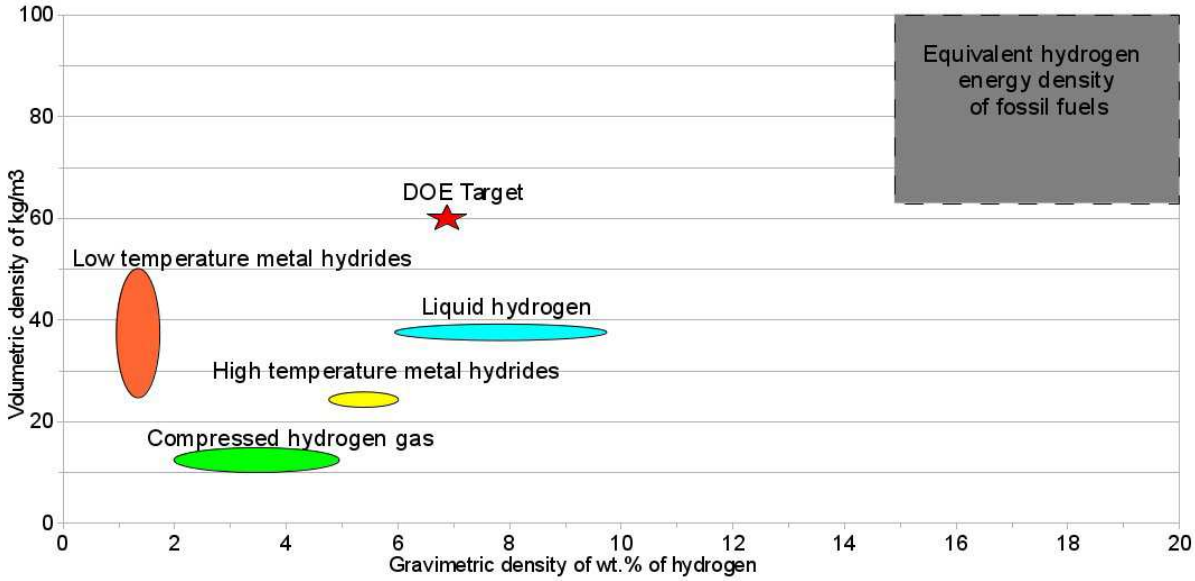

Figure 1-5 Energy density comparison chart between different methods.

As a matter of fact, hydrogen as the first element is not difficult to form hydrides with the majority of metals in the element tables. Nevertheless, the solution people are looking for is always the reversible capacity. Extensive study has been put on metal hydrides like $NaAlH_4$ [23], MgH_2 [24], $LaNi_5H_6$, LiH [25], and $TiFeH_2$ [26]. The most successful commercialized Ni-MH battery have been using $LaNi_5$ as the base system, despite its low theoretical hydrogen storage capacity, however the fast kinetic in electrochemical performance has determined its dominance in the market. Therefore, thermodynamic stability of the hydrides is another attribution people choose as an ideal candidate, which is closely related to the electrochemical properties of the materials.

1.1.2 Ni-MH electrochemical reactions

The electrochemical reactions at positive and negative electrodes in Ni-MH batteries are as follows:

(Positive) $Ni(OH)_2 + OH^- = NiOOH + H_2O + e^-$ (1)

(Negative) $M + H_2O + e^- = MH + OH^-$ (2)

And therefore the overall reaction is represented as:

(Overall) $Ni(OH)_2 + M = NiOOH + MH$ (3)

M and MH in the formula represent the metallic alloy and the metal hydride. The key to the whole reaction is in the negative electrode material where metal hydride is formed, and is also where all the research in the field has focused on.

First of all, the thermal dynamic stability of the hydride needs to be studied. The equations that need to be well understood are the following:

$M + x/2\ H_2 = MH_x + \Delta H_f$ (4)

$\ln [P_{H_2}/P^\circ] = \Delta H/RT - \Delta S/R$ (5)

$\Delta G = \Delta H - T\Delta S$ (6)

The Gibbs free energy of formation (*ΔG*) is calculated according to Eq. (6), which involves both the enthalpy change (*ΔH*) and entropy change (*ΔS*) in the reaction. While the entropy change with hydride formation is mainly caused by a standard entropy loss of the hydrogen gas, it may be considered as independent upon the metal hydride alloy. This has left the enthalpy change to be the decisive factor to the thermal dynamic stability of the metal hydride. It is suggested by Kleperis et al. [27] that a viable candidate should have a *ΔH* value between -25 and -50 kJ mol^{-1}, indicating that too little the value would render the alloy not sufficiently stable for charging at room temperature, whereas a

high value of ΔH predicts a difficult discharging process at room temperature, caused by the excess stability of the hydride. Secondly, the charging and discharging process in reality is much more complicated than it is shown in the reversible reaction Eq. (2), which can be decomposed to several following procedures:

$$M + H_2O + e^- \leftrightarrow MH_{ads} + OH^- \quad \text{(initial hydrogen adsorption)} \qquad (7)$$

$$MH_{ads} \leftrightarrow MH_{abs} \quad \text{(hydrogen diffusion)} \qquad (8)$$

$$MH_{abs} \leftrightarrow MH_{hydride} \quad \text{(metal hydride formation)} \qquad (9)$$

$$2MH_{ads} \leftrightarrow M + H_2 \quad \text{(hydrogen evolution)} \qquad (10)$$

$$MH_{ads} + H_2O + e^- \leftrightarrow M + H_2 + OH^- \quad \text{(hydrogen evolution)} \qquad (11)$$

where H_{ads}, H_{abs} represent adsorbed hydrogen on the alloy surface, absorbed hydrogen in solid solution. The steps of hydrogen adsorption/desorption, hydrogen diffusion, and formation/decomposition of metal hydride can be illustrated by the reaction Eq. (7) - (9). Hydrogen is firstly produced by Eq. (7), known as Volmer reaction. Afterwards, the produced hydrogen can either be absorbed further into the alloy as solid solution, or starts the hydrogen evolution reactions, which are the Tafel reaction (Eq. (10)) or even Heyrovsky reaction (Eq. (11)). The negative electrode potential against charging time plot can illustrate the charging process clearly shown in Figure 1-6.

The charging starts with the company of Eq. (7), and when the hydrogen on the surface H_{ads} begins to diffuse into the alloy represented by Eq. (8), the solid solution of hydrogen H_{abs} known as α phase is formed. Further charging slows down with the saturation process of α phase, and triggers the transformation from α phase to β phase ($MH_{hydride}$). In the transformation stage,

the potential of the negative electrode does not change since the input of hydrogen content does not increase. Larger the scale of this plateau, the more hydrogen can form into metal hydride. By the time the conversion of α phase to β phase finishes, the balance is broken and the curve mounts again with more intake of hydrogen into the system. Above all, the plateau is critical to look into when one looks for the characteristics of a potential metal hydride candidate.

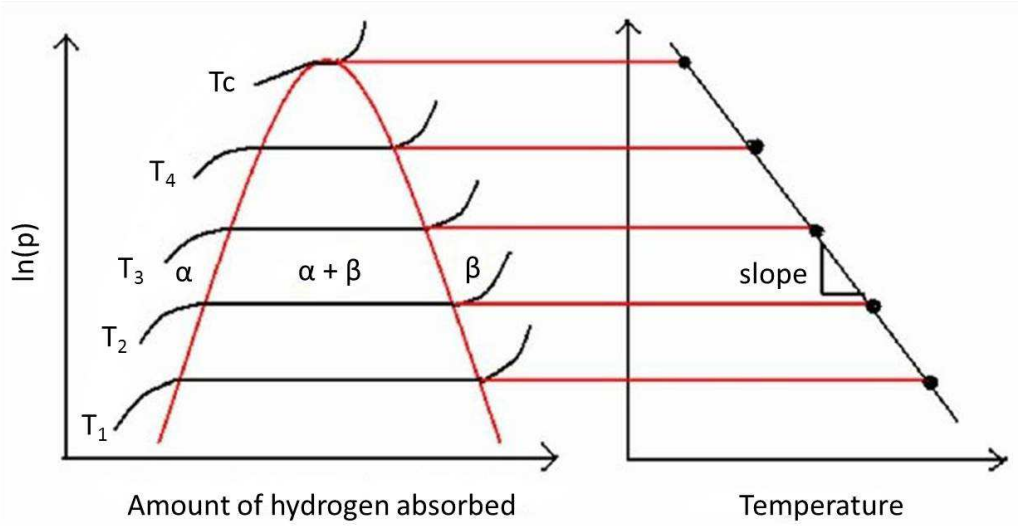

Figure 1-6 Schematic PCT diagram at different temperature (T1<T2<T3<T4<Tc) and the Van't Hoff plot [28]

In fact, the behavior of the negative electrode material in the electrochemical reaction is not only decided by the thermal dynamic energy alone, but also the kinetic energy, which many authors have studied to explain the mechanism [28-30]. There are several energy barriers for the formation of metal hydrides, such as physisorption and chemisorption of hydrogen molecules, hydrogen atom penetration and diffusion in the metal bulk, nucleation and growth of metal hydride (β phase), and the diffusion of hydrogen atoms though the hydride phase.

In general, the battery performance can be measured by the indicators like the reversible discharge capacity, the initial activation, the high-rate capability

and the cycle life, which is heavily influenced by the exchange current density and hydrogen diffusion factors.

1.2 Ti-Ni system

1.2.1 Ti-Ni phase diagram

The Ti-Ni system has been extensively studied as attractive functional material, mainly because of its practical shape memory properties. The source of its unique physical properties is the transformation behavior between the martensitic structure and the austenitic structure the TiNi can form. The different Ti-Ni binary alloys are many, which made the phase diagram still controversial until the late 1980s. However, despite the reports of a few metastable phases such as Ti_3Ni_4 [31], Ti_2Ni_3 [32], the essential phases of the Ti-Ni system are well known as TiNi, Ti_2Ni, and $TiNi_3$ (Figure 1-7). As for the metal hydrides research, the most studied ones are TiNi and Ti_2Ni.

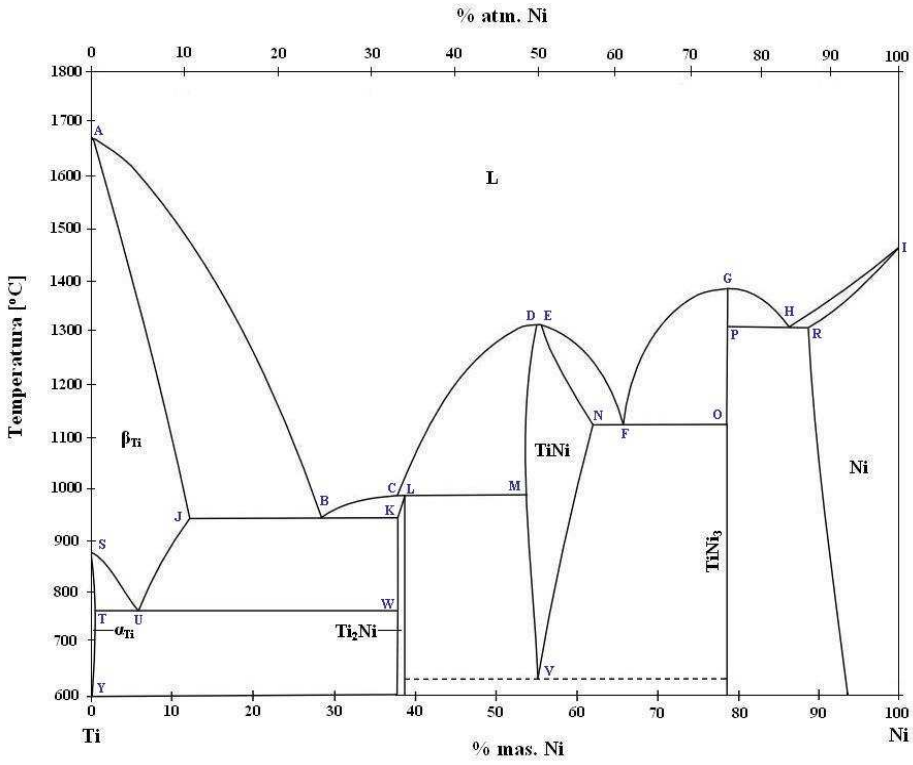

Figure 1-7 Ti-Ni phase diagram above 600 °C

1.2.2 TiNi in Ni-MH battery system

The TiNi alloy has been studied as metal hydrides as early as 1979 [33], and is still an active research candidate as the potential hydrogen storage materials nowadays [34-36]. TiNi phase that has a CsCl type structure (space group *Pm*-3*m*-221), with a lattice constant of 0.315 nm at room temperature [37], is also referred to as the high temperature phase or austenitic phase. The other type of TiNi is the martensite phase with a monoclinic B19' structure (space group $P2_1/m$) [38].11

Besides its popularity in the research of SMA (shape memory alloy), TiNi is also the first alloy studied as a hydrogen storage material. It was reported that TiNi compound can absorb hydrogen as much as 1.4H/f.u. (formula unit) under room temperature and pressure, which is about 230 mAh/g capacity in the electrochemical reaction [39-41]. Improvement for both the discharge capacity and electrochemical performance is expected.

Large numbers of experimental works with element substitutions and dopes for both Ti and Ni are investigated to improve the general electrochemical performance, e.g. Mg, Mn [34], Zr [34, 35], Pd [42], B [43]. Among these substitutions, most targeted Ni because Ti is essential for the formation of metal hydride, whereas Zr was also to replace Ti due to that they are in the same group in the periodic table. In a series of element substitution experiments (Mg, Mn, Zr), Szajek et al. [34] found that both discharge capacity and cycle life of the negative electrodes made by TiNi were improved after element substitution. They gave the explanation following the band structure calculations, which showed that the introduced impurities cause decrease of the width of the valence bands. The partial substitution of B for Ti and Ni realized by ball milling showed a formation of solid solutions of B in TiNi after milling, and subsequent

annealing produces TiNi and $TiNi_3$ phases. The discharge capacity was found lower than TiNi.

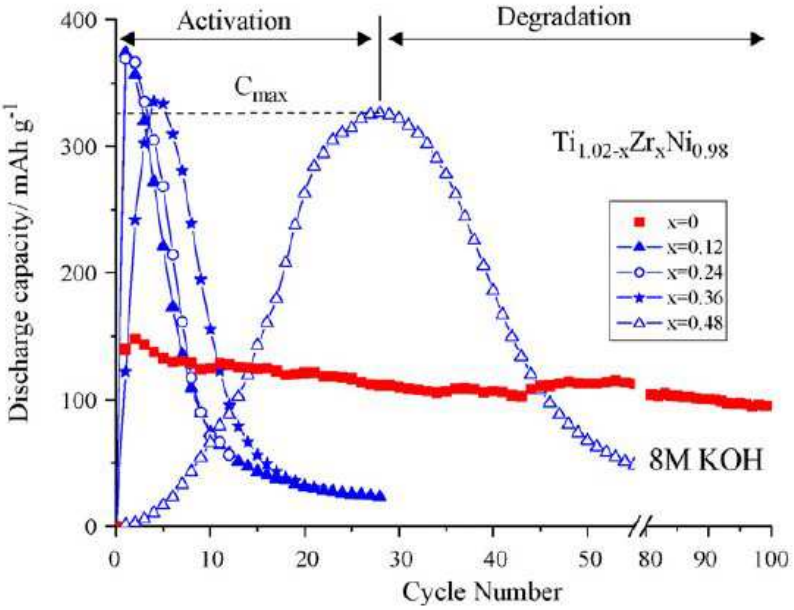

Figure 1-8 Cycle-life behavior of $Ti_{1.02}Zr_xNi_{0.98}$ ($0 \leq x \leq 0.48$) compounds [46].

Several studies of Zr substitution and the influence of morphology for TiNi from the group of Cuevas et al. are especially interesting and significant [35, 44-47]. There studies can be summarized to the following key points: 1) $Ti_{50-x}Zr_xNi_{50}$ (x = 0, 6, 12, 18 and 24) were obtained either as austenite or as martensite by induction melting or melting-spinning respectively. 2) The parental crystal structure on the hydrogenation of $Ti_{0.64}Zr_{0.36}Ni$ influences the structure on the hydrogenation. As for austenitic type (CsCl-type structure), the hydride preserves its metal sublattice and forms $Ti_{0.64}Zr_{0.36}NiH_{1.6}$ (P_{H_2} = 1 MPa and T = 373 K), whereas the monoclinic TiNi-type structure of martensitic $Ti_{0.64}Zr_{0.36}Ni$ is hydrogenated into two coexist hydrides, $Ti_{0.64}Zr_{0.36}NiH$ and $Ti_{0.64}Zr_{0.36}NiH_{2.2}$, both of which have an orthorhombic CrB-type structure. 3) Martensitic transformation in TiNi-alloys is easily influenced by Zr addition, hence can be used to tailor the final product of alloying Ti-Ni-Zr. 4) Martensitic type structure can increase the hydrogenation percentage of TiNi significantly

with an obvious PCI plateau, while the austenitic type shows no plateau on the PCI curve. 5) Despite the increase in discharge capacity Zr substitution for Ti brings up, it also causes severe degradation issue to the system, the reason of which was explained as the loss of electrical contact due to the alloy pulverization (Figure 1-8) [46].

1.2.3 Ti_2Ni in Ni-MH battery system

Ti_2Ni is the other Ti-Ni binary alloy that is able to store considerable amount of hydrogen. It was first reported that hydride of Ti_2Ni had a capacity as high as 500 mAh/g in a gaseous hydrogen absorption reaction [48]. Later, a Ti_2Ni alloy prepared by arc melting obtained only 160 mAh/g with poor cycling stability [49], and the cause of capacity loss was suggested to be the formation of irreversible $Ti_2NiH_{0.5}$ upon hydrogenation. Zhao et al. [50, 51] conducted investigations on the performance of amorphous Ti_2Ni alloy. They found that amorphous phase of Ti_2Ni helps to stabilize cycling performance. The alloy was synthesized by solid-state sintering and then ball milling to obtain an amorphous phase, which had a rather stable discharge capacity that ranges from 100 mAh/g and 125 mAh/g. In comparison, the discharge capacity of non-milled Ti_2Ni (alloyed by solid-state sintering) reached 280 mAh/g in the first cycle, but dropped to less than 100 mAh/g after 50 cycles.

Element substitutions were also applied on Ti_2Ni alloy in order to improve its performance as the negative electrode for Ni-MH batteries. Luan et al. [10, 11] studied Al and B substitution for Ni respectively, but the improvement was not satisfactory. Takeshita et al. [52] experimented on the hydrogenation process of the ternary compound Ti_4Ni_2X (X = O, N, C). They found that these alloys all had higher hydrogen desorption pressure compared to Ti_2Ni, and presented a hydrogen pressure plateau.

Zr is also attempted to apply on Ti substitution for Ti_2Ni by Zhao et al.

[53], which was prepared by solid-state sintering, followed by ball milling and subsequent annealing. The discharge capacity against cycle number is presented in Figure 1-9. Zr was found to enhance the discharge capacity of non-equilibrium Ti_2Ni alloy at electrolyte temperatures of 313 and 333 K. In terms of structure influence, large content of Zr in the Ti-Zr-Ni alloy promotes the formation of Laves phase. While mild addition of Zr (x = 0.2) could reach the highest discharge capacity of about 250 mAh/g, alloy with larger content of Zr has a lower but stable discharge capacity. A rather special substitution of Vanadium for Ti ($(Ti_{1-x}V_x)_2Ni$) drew much attention for its particular quasi-crystalline structure [54]. The alloys were prepared by arc-melting and subsequent melt-spinning. The discharge capacity reached ~270 mAh/g (for x = 0.3), and the cycling capacity retention rate was about 80% after 30 cycles.

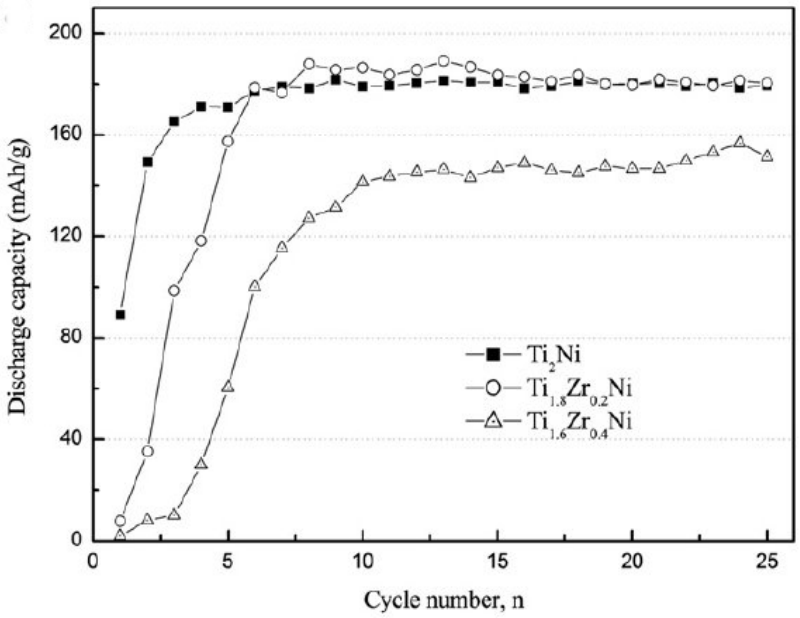

Figure 1-9 Cycling performance of $(Ti_{1-x}Zr_x)_2Ni$ (x = 0, 0.2, 0.4) [53].

1.2.4 Elemental substitution/doping for the Ti-Ni system

As a conventional approach for material property modification, elemental substitution/doping is also one of the main methods that are applied on the

improvement of Ti-Ni based materials for Ni-MH batteries. Due to the complexity of the binary Ti-Ni system and its variety of structure possibility, element substitution/doping influence is often significant, considering as well the interaction with hydrogen atom during the charging/discharging process. In the meantime this has made elemental substitution/doping effective to alter the properties of the alloy.

1.2.4.1 Zr influence

Since Zr is in the same group with Ti in the periodic table, it shares a lot in common with Ti properties. Besides, Zr and hydrogen have more than enough affinity. It was first used to substitute Ti to study its influence on the SMA property of TiNi [55], and Zr was reportedly to increase the MT temperatures.

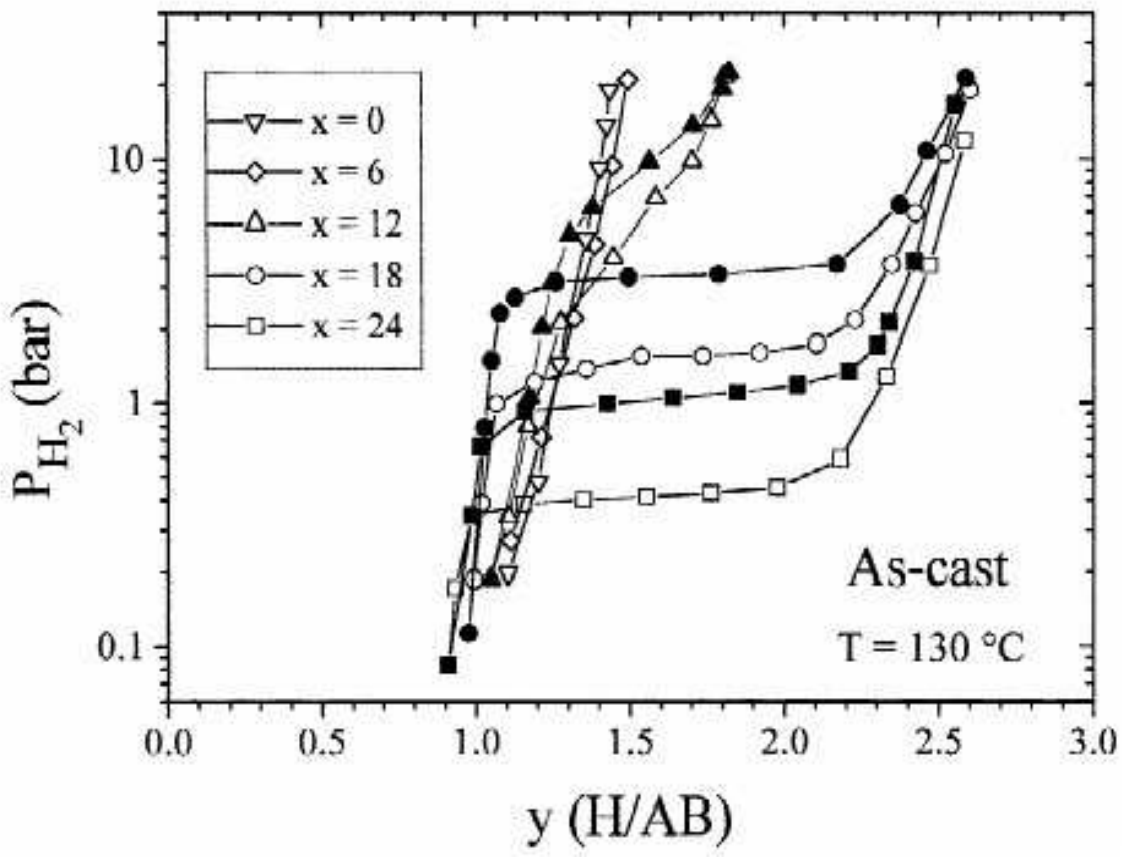

Figure 1-10 PCI-curves of as-cast $Ti_{50-x}Zr_xNi_{50}$. Full symbols and empty symbols correspond to absorption and desorption respectively [44]

In Figure 1-10, two different patterns can be seen before and after x reaches 18. When Zr content increases till x = 18, a clear plateau in the PCI curve appears, which is credited to the martensitic structure of TiNi. Since the alloys were all synthesized by casting, it also implies that the increase in Zr brings about the formation of the martensitic TiNi structure, which was later confirmed by Cuevas et al. [45]. Secondly, it was reported that Zr substitution for Ti increases the lattice constant, which may consequently increase the hydrogen capacity of TiNi [5, 44]. Hsieh et al. [55] studied the composition of Ti-Zr-Ni alloy as $Ti_{2-x}Zr_xNi$ (x = 0, 0.2, 0.4), they observed the phase transition as follows with the increase in Zr: η phase → η + λ_1 → λ_1 phase → λ_1 + θ phase → θ phase. The reference [56] is shown in Figure 1-11.

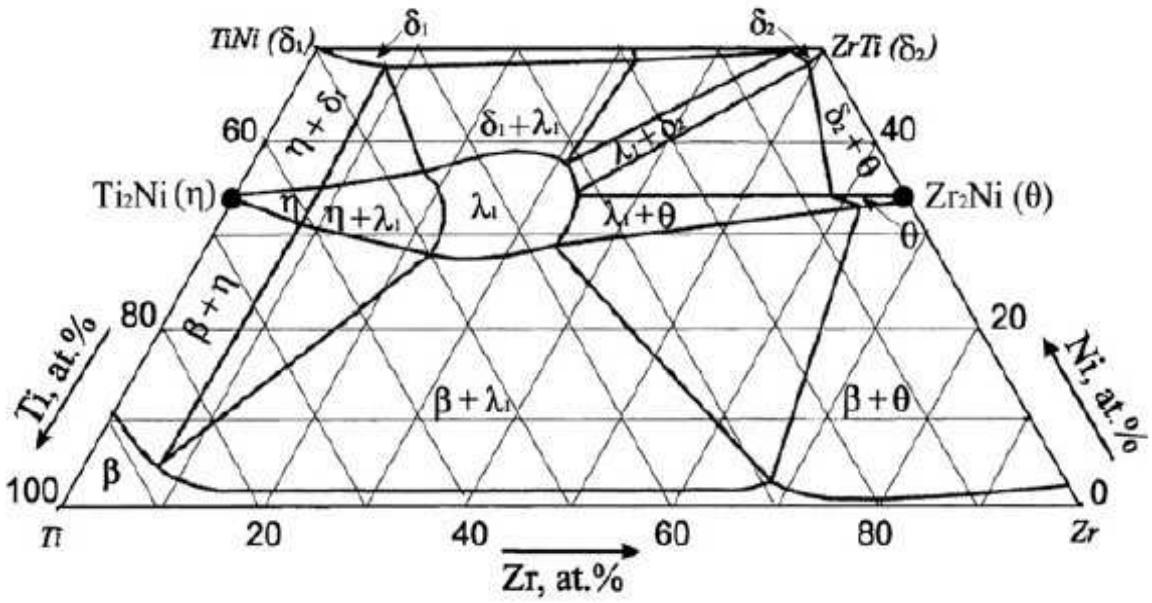

Figure 1-11 A partial isothermal section of the Ti-Zr-Ni phase diagram at 700 °C [56].

They found that Zr hinders the formation of amorphous phase for Ti-Ni but helps increase capacity as well as the cycling performance of amorphous Ti_2Ni.

1.2.4.2 Mg influence

Mg itself is being studied extensively for hydrogen storage materials due to its abundance, light weight and an extremely high theoretical hydrogen capacity (2200 mAh/g [15]). Therefore, substitution or doping of Mg for Ti usually happens in large quantity, and Ti is sometimes used to substitute Mg in Mg-based alloys for hydrogen storage materials [57]. Szajek et al. [5] experimented small quantities of Mg substitution for Ti and prepared $TiNi_{0.75}Mg_{0.25}$. They reported an increase in hydrogen discharge capacity of the BCC TiNi as a result of lattice constant increase (from 3.018 Å to 3.048 Å). In the stable solid state, the pure metals of Ti and Mg both have an HCP structure, nonetheless they are thermodynamically immiscible. Therefore, if the Mg content is high in the alloy, traditional melting technique is not applicable, as even the boiling point of Mg is lower than that of Ti. As a result, Ti-Mg alloying is done successfully through mechanical alloying by Kalisvaart et al. [58, 59]. They reported two structures after milling several different compositions of Ti, Mg and Ni. In another milling practice of Ti-Ni-Mg ($Mg_{0.5}Ni_{0.5}Ti$, $MgTi_{0.5}Ni_{0.5}$ and TiMg), no FCC structure was observed but a BCC structured phase. It is quite interesting to see however that Ti and Mg started alloying first in this experiment, while in the phase diagram there are more than one possibility for Ti-Ni alloy but Ti-Mg phase is non-existent. While this result is striking in a way, it is understandable when one realizes that mechanical alloying may produce metastable phases. The product of milling Ti-Ni-Mg is still unresolved when several other phases were found in the practice of alloying Ti, Mg (and Ni) including BCC, FCC, HCP and BCT [60-62]. These different results are summarized in Table 1-2.

Table 1-2 Products of alloying Ti-Mg with different approaches

Composition	Synthesis	PCA/Balls	Products for Ti-Mg
$Mg_{0.75}Ti_{0.25}$ [63]	MA of Ti, Mg powders	Steel/Stearic acid	FCC a = 4.42 Å | a = 4.26 Å
	MA of Ti powders, Mg ribbons, Pd as catalyst	Steel/Non	FCC a = 4.42 Å
$(Mg_{0.75}Ti_{0.25})_{0.95}Ni_{0.05}$ [59]	MA of Mg ribbons, Ti, Ni powders	Steel/Non	
MgTi [64]	MA of Ti, Mg powders, Pd as catalyst	Steel/Non	BCC (84%) a = 3.39 Å HCP (16%) a = 2.97 Å, c = 4.86 Å
$(Mg_{0.80}Ti_{0.20})_{0.95}Ni_{0.05}$ [58]	MA of Ti, Mg powders	Steel/Graphite	FCC a = 4.44 Å | a = 4.25 Å
$Mg_{0.75}Ti_{0.25}$ [59]	As deposited to thin film	N/A	HCP a = 3.11 Å, c = 5.02 Å
$Mg_{0.65}Ti_{0.35}$ [62]	MA of Ti, Mg powders	Steel/Non	HCP a = 3.17 Å, c = 5.15 Å BCC a = 3.42 Å
$Mg_{0.65}Ti_{0.35}$ [62]	MA of Ti, Mg powders	Zirconia/Non	HCP a = 3.19 Å, c = 5.20 Å FCC a = 4.23 Å

As for the performance of the Mg influence, the conclusions are not conclusive as many research practice are not closely connected, making it difficult to compare the results from different authors. In the study of Rousselot et al.[65], in which the compositions $Mg_{0.5}Ni_{0.5}Ti$, $MgTi_{0.5}Ni_{0.5}$ and TiMg were mechanically alloyed, they found that the $MgTi_{0.5}Ni_{0.5}$ electrode showed the highest discharge capacity (536 mA/g) compared to 401 and 475 mAh/g for the $Mg_{0.5}Ni_{0.5}Ti$ and MgTi electrodes, respectively, while they attribute the higher rate dischargeability of the $Mg_{0.5}Ni_{0.5}Ti$ electrode to its better H-diffusion kinetic properties compared to $MgTi_{0.5}Ni_{0.5}$. However, the relationship between the electrochemical performance and the structures were not fully discussed, as they were not sure the actual phase of the milling products. In the study of Kalisvaart et al. [59], in which they reported two FCC phases with similar lattice constant (a = 4.25 Å and a = 4.44 Å) when they mill a composition of $(Mg_{0.80}Ti_{0.20})_{0.95}Ni_{0.05}$, they further suggest that the FCC structure with the larger

lattice constant may be the one providing hydrogen storage as its abundance decrease with milling time, which caused a decrease in electrochemical capacity.

1.2.4.3 Other elements influence

Besides the most popular element substitution like Zr and Mg, several other elements were attempted, among which are mostly transition metals. These doping metals may expand the DOS (density of states) so as to improve the thermodynamics or kinetics of the alloys during the charging/discharging process, or they rather increase the discharge capacity, by increasing the original lattice constant as an example. A few elements that are found positive in general for the improvement of the electrochemical performance are Fe [66], Mn [5], while B [43], Sn [67] and Pd [42] have been reported negative. Co showed a lower discharge capacity when it was solely mechanically alloyed with the composition $TiNi_{0.8}Co_{0.2}$, it however performed better after annealing [67]. Above all, one should be noted that due to different synthesis techniques, the influence from the same element may vary. Thus it is crucial to assess the effect of certain element on the performance of the alloy with consideration of the alloy preparation method.

1.3 Mechanical alloying

1.3.1 Mechanical milling as alloying technique

As a new mechanical alloying method, mechanical milling has drawn extensive attention as an alloying process. First of all, mechanical milling is very different from most traditional alloying method as it is common to produce non-equilibrium phases, which does not necessarily appear in a phase diagram.

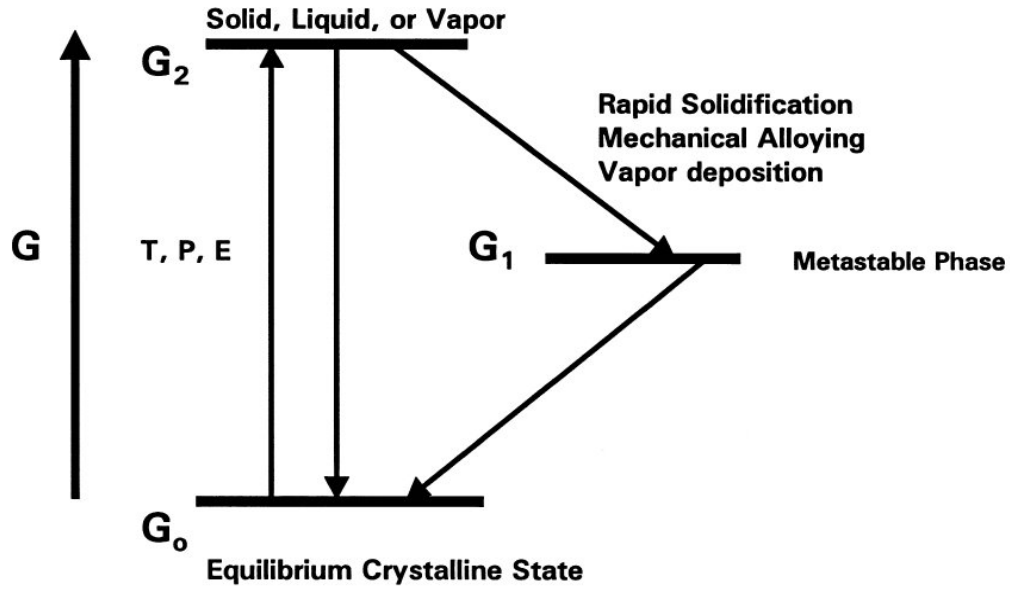

Figure 1-12 Basic concept of the non-equilibrium material.

By means of mechanical milling, some immiscible alloys may be synthesized. Furthermore, mechanical milling can reduce the grain size substantially, resulting in the formation of nanocrystalline or amorphous phase, which is essential to many material characteristics sought after.

As it is compared to rapid solidification and vapor deposition (Figure 1-12), the departure energy from equilibrium for mechanical alloying was reported at 30 kJ/mol [67], which is higher than rapid solidification (24 kJ/mol) and lower than condensation from vapor (160 kJ/mol) [68].

1.3.2 Mechanical milling in hydrogen storage material application

Several research groups applied mechanical activation methods for the synthesis of hydrides [69]. They first operated the milling of mixtures of elements under inert gas atmosphere to synthesize intermetallic compounds, and the products of the milling were exposed to hydrogen to form hydrides. It is found that mechanical milling improves hydrogenation kinetics due to its nanocrystalline structure. In recent years, mechanical milling has been widely

applied in the hydrogen storage materials research, especially due to its efficiency to alloy several elements.

There are generally two steps that are frequently applied for the synthesis of the alloys for metal hydrides. The initial elements were first mechanically alloyed, which produces a nanocrystalline/amorphous phase, and then subsequently follow a heat treatment, such as annealing or melting.

Zaluski et al. [70] investigated the hydrogen storage absorption properties of Mg_2Ni prepared by mechanical alloying. They found that Mg_2Ni in nanocrystalline phase obtained by ball milling shows significantly enhanced hydrogen absorption characteristics, and the activation is much quicker because of the active surfaces of the powder created in the ball milling process. Another example of comparing the mechanical alloying samples and arc-melted samples was done by Wang [71], who did an experiment of comparing the hydrogen storage properties of $Ti_{0.37}V_{0.38}Mn_{0.25}$ prepared by mechanical alloying and vacuum arc melting. He found that the alloy prepared by vacuum arc melting has a single phase BCC crystal structure, and the maximum hydrogen absorption is 3.62 wt%, compared to samples prepared by mechanical alloying which has an amorphous crystal structure, with a maximum hydrogen absorption of 1.76%. Nevertheless, although the hydrogen storage powders prepared by mechanically alloyed samples show better cyclic performance, the total hydrogen-absorption capacity of vacuum arc samples are higher than that of the mechanically alloyed samples. It is common to find that as-milled alloys which feature a nanocrystalline/amorphous phases exhibit better activation and cycling stability characteristics, while suffers capacity loss in general (Figure 1-13). For more details of the comparison of MA with other synthesis methods, please refer to appendix 1 “methods of preparing hydrogen storage materials”. Zhao et al. [50] explained the improvement of amorphous phase by stating that the metal hydrogen interaction within the bulk amorphous alloy is weakened, and there is

a lower energy barrier of hydrogen penetration through alloy surface for the amorphous phase.

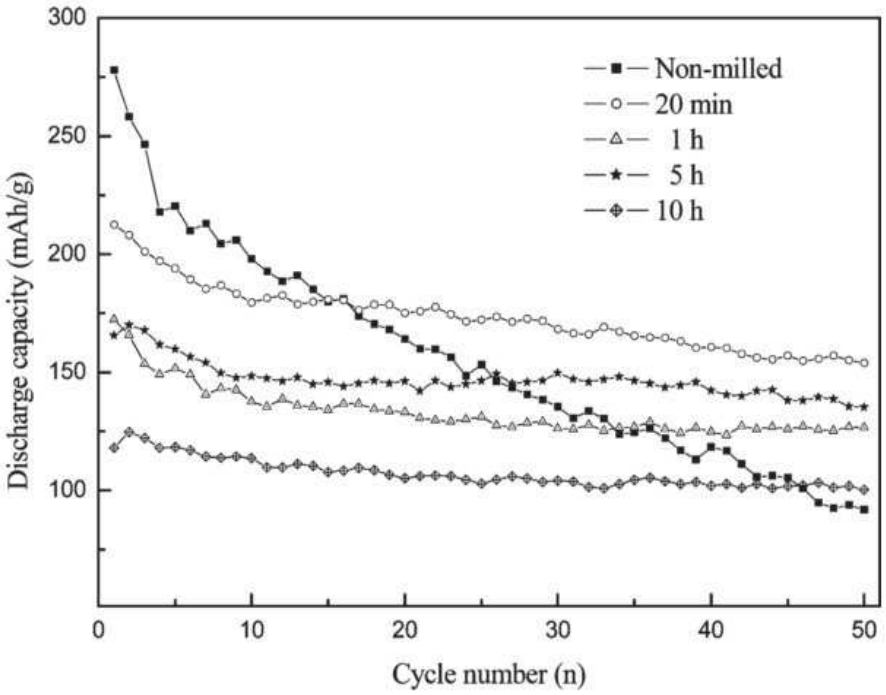

Figure 1-13 Discharge capacities of Ti_2Ni electrodes as a function of the cycle number. [49]

Another main reason to apply mechanical alloying is to take advantage of its possibility to alloy immiscible elements that traditional synthesis method cannot. A good example is Ti-Mg. Despite the non-existence of Ti-Mg alloy in their binary phase diagram, Ti-Mg has been successfully alloyed by several teams in research for Ni-MH battery materials [36, 58, 59, 63].

Chapter 2 Experimental and Density Functional Theory

This chapter describes the experimental techniques used in this study, including the means of preparing samples (HEBM), microstructure characterization (XRD, SEM, TEM), hydrogenation properties measurement (solid-gas and electrochemical approaches) and a brief introductory to the DFT (Density Functional Theory).

2.1 Material preparation: mechanical alloying

Developed by Benjamin et al. in the 1960s, aiming to produce homogeneous materials from element powder mixtures, mechanical alloying (MA) has become an advanced material alloying method, which processes powders in solid state. The straightforward advantages derive from MA include synthesis of immiscible element by traditional alloying approach, mass product yielding, and extremely fine crystalline (grain size in nanometer) production. Nowadays, MA is frequently used to improve mechanical, chemical and physical properties of the material [73].

2.1.1 Principle

MA (mechanical alloying) generally refers to the process of MM (mechanical milling), except that mechanical milling can equally be used on pure metals, intermetallics or pre-alloyed powders, which does not necessarily produce new alloys.

MA starts with mixing of the powders with desired proportion of different powders. The loading of powder mix into the mill can be done under an inert gas atmosphere if necessary, during when the grinding balls and PCA (process grinding agent) are also put in the vial. The essential factor that plays often a decisive role is the energy input to the milling, which is controlled by several milling conditions, such as B/P (ball to powder ratio), speed, time etc. A milling

should be considered to be complete until it reached a steady state when particles share the same composition.

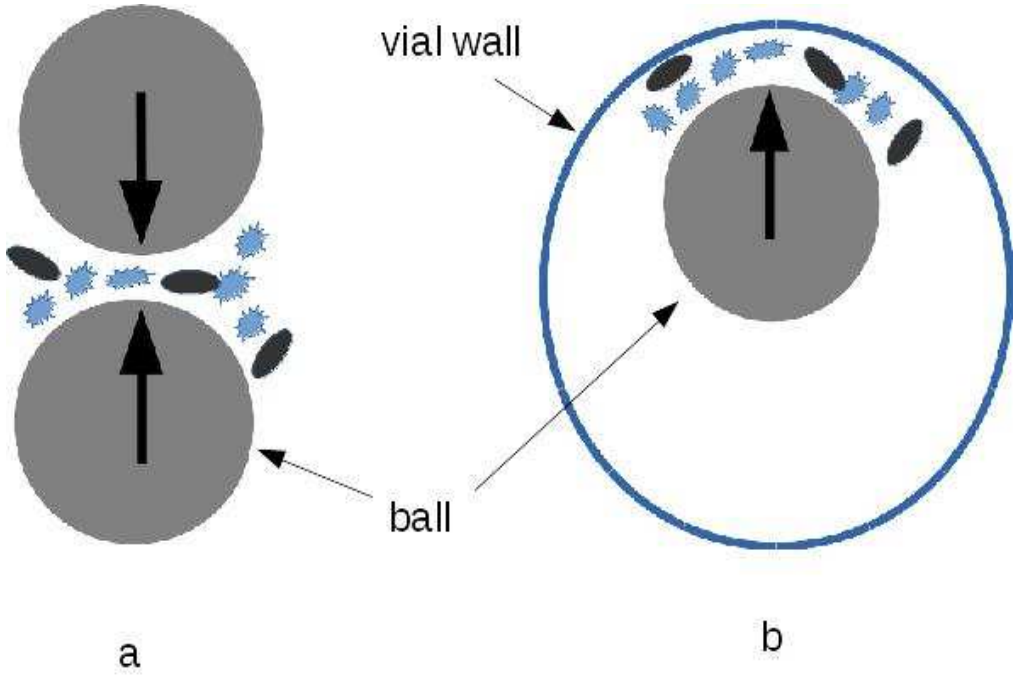

Figure 2-1 Mechanical stress during ball milling

Figure 2-1 shows two types of pressing the submitted materials undergo during milling, clashing of two balls (Figure 2-1 a) or clashing of the ball and the vial (Figure 2-1 b). The pressing induces physiochemical reaction by introducing mechanical stress, which leads to an elastic deformation of reagent at first, continued by an irreversible plastic deformation, and consequently results in fracturing.

The fracturing stage brings about defects of the material including cracks, new surfaces, dislocations, vacancies, grain and others. At this stage, it usually yields ultra-fine grain size. With prolonged milling, the second stage named “cold welding” becomes dominating, accompanied by crystallinity breaking, alloying or amorphization [72].

Several key variables that affect the outcome of milling include:

- type of mill,
- milling container,
- milling speed,
- milling time,
- type, size of the grinding ball,
- ball to powder weight ratio,
- extent of filling the vial,
- milling atmosphere,
- process control agent, and
- temperature of milling. [72]

Changing the parameters increases or decreases the energy input into the system in general. A higher value of milling speed, time or B/P ratio gives more energy. Other parameters also play crucial or even decisive roles in a milling setup. For examples, Nouri et al.[73] studied the influence of different types of PCA on milling product. Milling atmosphere is usually either inert gas or reactive gas added purposely. The former prevents the reaction between the milling powder and air, whereas the latter is expected to react with the milling powder, which is also called “reactive ball milling (RBM)”. Extent of filling the vial is suggested to be around 50% to have optimal efficiency. Material of the

vial and ball should be picked so that it does least contamination to the milling product, and it was reported to affect the final product of the milling as well [64]. There have been some studies on the influence of temperature of milling, in which it showed that temperature has a significant effect in an alloy system as expected [74]. Therefore temperature rise induced by long time of milling should not be neglected.

2.1.2 Milling conditions

In the present study, a planetary type mill Retsch PM 400 is used with steel vials and steel balls. The details of the milling setup is illustrated in Figure 2-2, where two steel balls (d = 20 mm) are placed in 50 ml volume steel vials. The filling of the starting powder was carried out in a glove box filled with argon as the protective gas. 2 wt. % of ethanol was added to all starting powders to prevent otherwise sticking milling products on the vial wall or the balls. The rotation speed was fixed at 400 rpm. In order to dissipate heat, all millings were scheduled a 30 mins pause every 30 mins. Table 2-1 lists all the samples studied and their milling details.

Table 2-1 Milling regime for individual composition

Composition	Starting powder	Milling time (hours)	B/P
$Ti_{2-x}Zr_xNi$ (x = 0, 0.1, 0.2)	**Ti** (99%, ≤ 150 µm), **Zr** (≤ 45 µm), **Ni** (99.5%, ≤ 250 µm)	20 , 40 , 60 (*x = 0*) **60** (x = 0, 0.1, 0.2)	3.3:1
$(TiNi)_{1-x}Mg_x$ (x = 0, 0.1, 0.2, 0.3)	**Ti50-Ni50** (≤ 150 µm), **Mg** (99.8%, ≤ 50 µm)	0, 10, 20, 40 (*x = 0*) **40** (x = 0, 0.1, 0.2, 0.3)	4.4:1
$(TiH_2)_{1.5}Mg_{0.5}Ni$	**TiH_2** (98%, ≤ 44 µm), **Mg** (99.8%, ≤ 50 µm), **Ni** (99.5%, ≤ 250 µm)	10, 20, 30, 40	4.4:1

Figure 2-2 Retsch PM 400, vials and balls and present planetary mill setup

2.2 Structural and chemical characterization

Structural characterization used in this study includes XRD (X-Ray diffraction), SEM (Scanning electron microscopy) and TEM (Transmission electron microscopy). Chemical analysis was done by the Energy-dispersive X-ray spectroscopy method.

2.2.1 X-Ray diffraction

Developed as early as 1920s, XRD analysis has been one of the most common and powerful tool for the examination of the powder sample microstructure. Obtainable data of a given sample include crystal structures, phases, preferred crystal orientations, as well as structural information such as average grain size, strain and so on.

The principle of XRD is the Bragg's law (Figure 2-3 [75]), which is used in combination with the wave interference theory. In the formula: $n\lambda = 2d\sin\theta$, λ, d and θ represent the wavelength of the X-ray, interplanar distance and incident angle respectively, while n is any integer number which leads to a constructive interference.

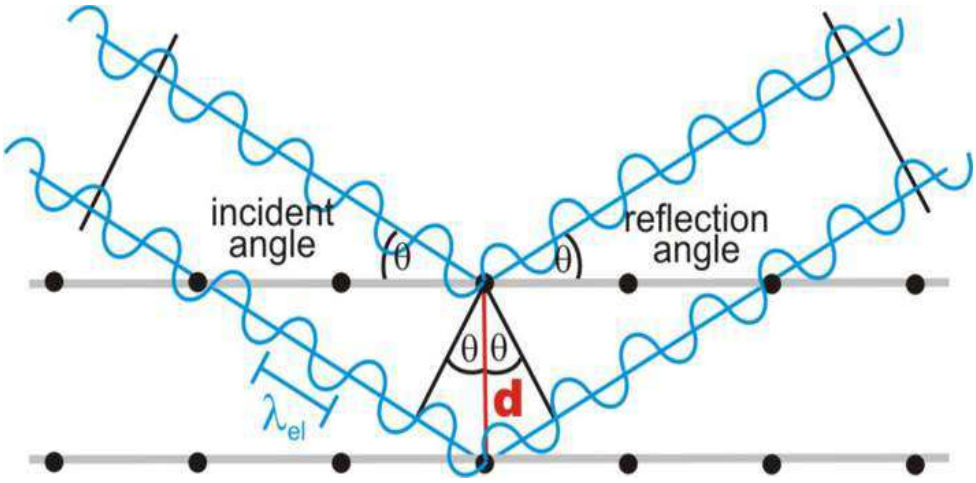

Figure 2-3 Illustration of Bragg's Law of Diffraction [75]

As illustrated in Figure 2-3, rotated incident beam scans the flat surface of the prepared powder, and collect the information of the (h, k, l) plane of the sample with the help of the formula $\lambda = 2d_{hkl}\sin\theta_{hkl}$. Eventually, it generates a pattern for each crystalline structure type, namely cubic, tetragonal, hexagonal, rhombohedral, orthorhombic, monoclinic, triclinic. By comparing the pattern of the examined sample with the database of the known material structures, one may identify the peaks obtained hence infer the content of the sample. Specifically for the milled powder sample, the peak often look much broadened than a standard crystalline peak. This can be explained by the Scherrer equation $B_L = K\lambda/L\cos\theta$, where L is the mean crystallite size, B_L is a standardized width of a peak, λ is the wave length of the incident light and θ is the Bragg angle. Due to the nature of MA processed powder, which often contains several structures

in one sample, the XRD pattern can be a complex. In this case, Rietveld or profile fitting method can be used when analyze the XRD data. Rietveld refinement is the procedure which simulates the XRD patterns of using the theoretical or known systems, and calculates the difference of fit with measured data, whereas profile fitting fit experimental data empirically with a series of common mathematical equations.

Figure 2-4 Bruker D8 Advance X-ray diffractormeter (left) and Bragg-Brentano geometry (right)

In the current study, XRD was performed on a Bruker D8 Advance X-ray diffractometer with Cu Kα radiation (λ = 0.15418 nm) filtered by nickel. The device can be seen in Figure 2-4 (left), and the bragg-Brentano geometry is shown on the right, which consists of: (1) goniometer, (2) X ray tube, (3) primary optics, (4) sample platform (5) secondary optics, (6) detector. Note that the focus of the X-ray tube, the specimen, and the detector slit are located on a single circle. A simplified scheme of the goniometer is illustrated in Figure 2-5

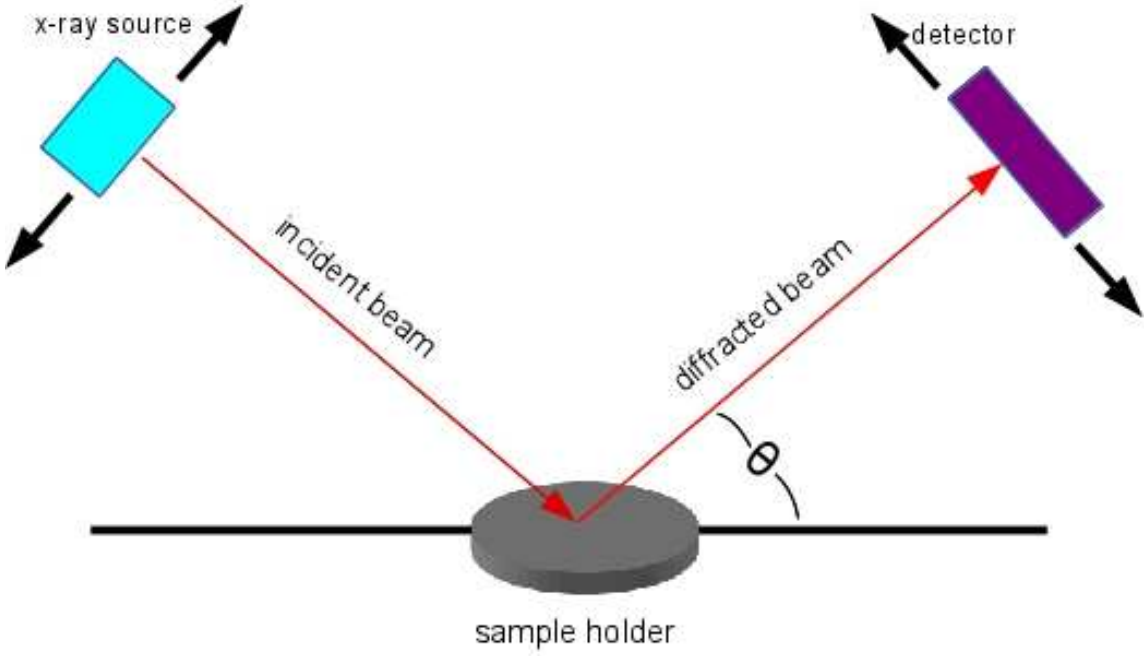

Figure 2-5 Illustration of an XRD device

2.2.2 Scanning electron microscopy

SEM (scanning electron microscope) is a type of electron microscope that uses high energy electron beam to hit (scan) the surface of the sample to produce a SEM image through different types of emitted electrons. In practice, the most common SEM images are the secondary-electron type, which are used to show the morphology or the topography of a surface. Typical SEM equipment can be illustrated as in Figure 2-6 (left), and on the right, is the model JSM-5800LV.

SEM can be installed as standalone equipment with (or without) EDX (Energy-dispersive X-ray spectroscopy) support, or installed as an addition to TEM for a synthetic analysis. EDX (or EDS) analysis is used for chemical characterization (elemental analysis) purposes. As each element has a unique atomic structure, the X-ray emission characteristic is then unique. The report of this technique usually comes with the relative atomic composition of the examined samples.

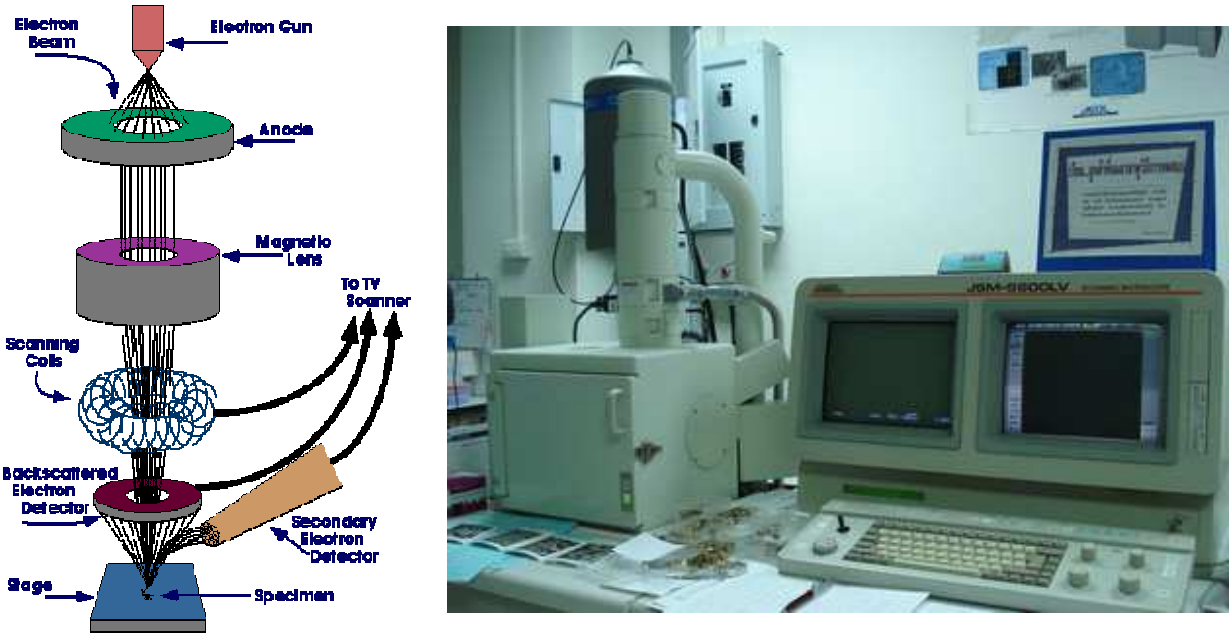

Figure 2-6 Scanning electron microscope scheme (left) and machine (JSM-5800LV) (right)

We have used the model JEOL JSM-5800LV with Energy-dispersive X-ray spectroscopy support in this study, which operate at magnifications from 18x to 300000x and with an accelerating voltage of 0.3 to 30 kV. There are both a high-vacuum and a low-vacuum mode. The sample chamber can hold multiple normal SEM samples using the rotating sample holder or a single sample as large as 8 inches in diameter.

2.2.3 Transmission electron microscopy

TEM uses electrons that have passed through a thin specimen and are focused to create the image with a spatial resolution, which is significantly higher than light microscopes. Provided the prepared sample is thin enough, all electrons are expected to be transmitted through. However, the electrons are scattered by the atoms of the specimen. In any part of the field of view where no specimen is present, and the electrons remain unscattered, it appears bright relative to the specimen. And this results in a bright-field image. Considering the

wave nature of the incident electron beams, TEM can also be used to obtain diffraction images of a crystalline material. In this case, it is very similar to the XRD technique, and it also features the Bragg's law: $n\lambda = 2d\sin\theta$. Take Figure 2-7 as an example, the relationship between the radius R of a given diffraction ring and scattering angle θ is given by:

$$R = L\tan\theta \qquad (2\text{-}2)$$

where L is the distance from where the diffraction pattern were recorded to the specimen (ignoring the presented imaging lenses in the purpose of simplification.) [76]

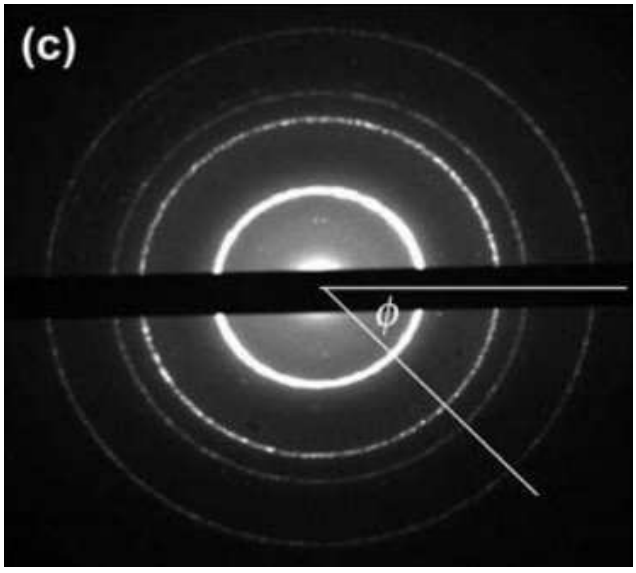

Figure 2-7 Example of TEM diffraction image

The lateral resolution of the best microscopes is down to atomic resolution. A schematic presentation of the microscope is shown in Figure 2-8. With an electron gun an electron beam is formed, which is accelerated by an electric field formed by a voltage difference of, typically, 200 kV. By condensor aperture, the electron beam is focused to a spot of 1 mm on the thin film, and the

first image is formed by the objective lens, magnified typically x25. The following lenses give a final magnification of the image of more than $x10^6$. The thin-sample images, electron diffraction patterns can be formed on the final image screen. In bright field imaging, the image of a thin sample is formed by the electrons that pass the film without diffraction, as the diffracted electrons are stopped by a diaphragm. In the corresponding dark field imaging mode, a diffracted beam is used for imaging. The grain size and lattice defects can be studied with the image mode, while the crystalline structure is studied by the diffraction mode. If the device is supported by EDX, the chemical composition of small volumes can be obtained by detection of x-rays emitted from the film.

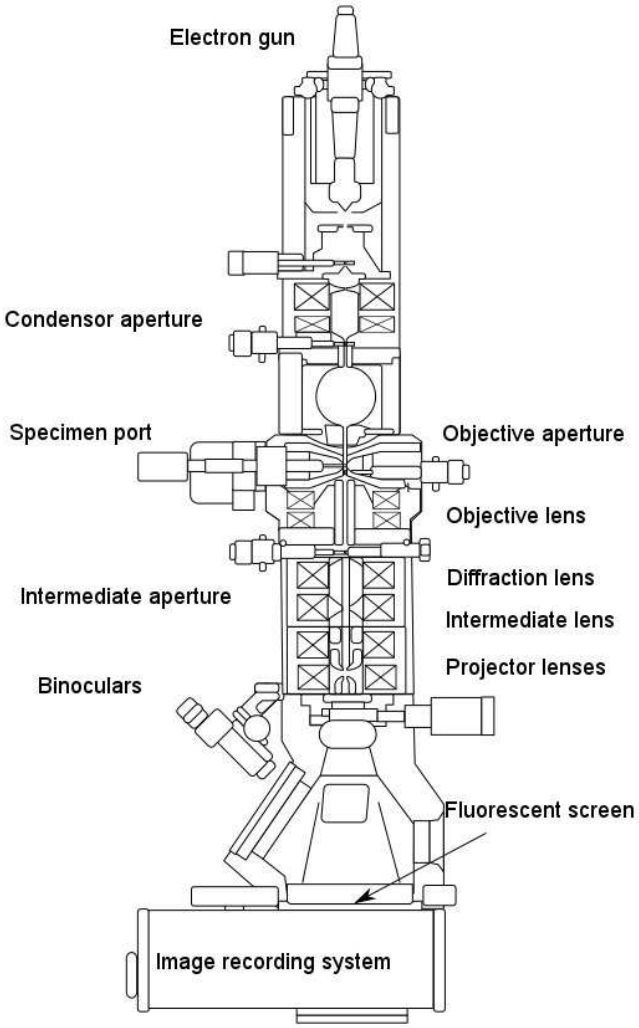

Figure 2-8 Schematic TEM presentation

In the current study, the TEM images were created using the model JEOL JEM-2100 (Figure 2-9), which operated at 200 kV accelerating voltage). The specifications of this device are as follows:

- Thermal electron emission gun type, LaB_6
- Accelerating voltage, 80kV, 200kV
- HTP polepiece, point resolution 0.25 nm, lattice 0.14 nm
- Energy Dispersive X-Rays Spectroscopy (EDS JEOL JED 2300T 30 mm^2, resolution 133 eV on Mn K)
- Gatan Erlangshen ES500W camera (1350 x 1040), port 35mm
- Gatan slow-scan camera USC 1000 (2000 x 2000)

Figure 2-9 TEM model JEOL JEM-2100

Its capability includes: crystallographic and chemical analysis, nanomaterials (nanotubes, nano-ribbons), catalysis nanoparticles, steels, alloys and compounds.

TEM sample preparation is also considered to be highly demanding, as electron microscopy in form of films mounted on fine-meshed grids must be very thin. The equipped sample preparation is presented in Figure 2-10.

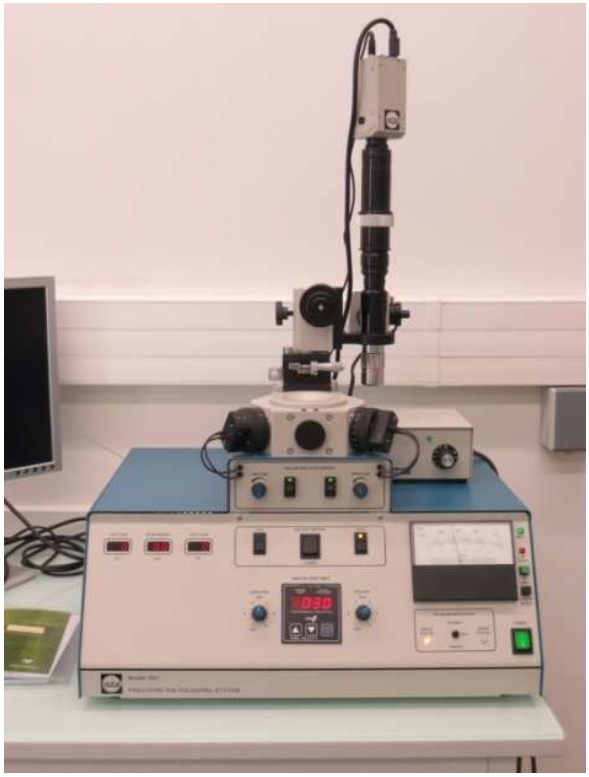

Figure 2-10 Equipped TEM sample preparation platform

2.3 Measurement of electrochemical and physical hydrogenation

2.3.1 Sievert's manometric measurements and PCI

Sievert's manometric measurement is a system to measure the amount of hydrogen that the tested sample can absorb/desorb in solid-gas reaction, which is widely adopted by the metal hydride researchers. The scheme of the

experimental device is shown in Figure 2-11 [77], and the principle follows the ideal gas law:

$$PV = nRT \tag{2-3}$$

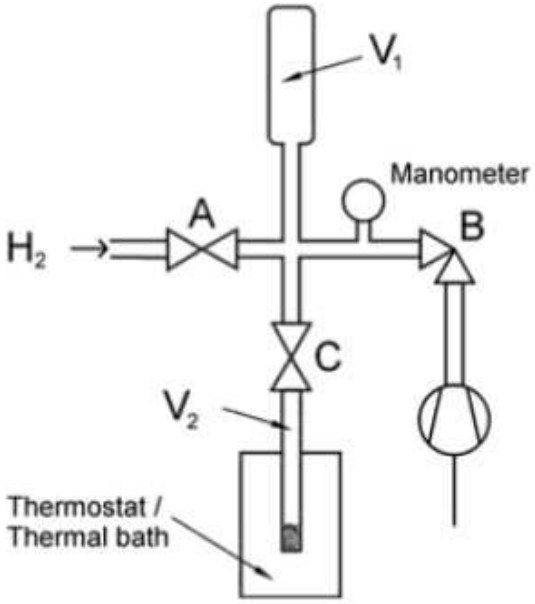

Figure 2-11 A schematic diagram of a basic manometric sorption measurement system [77].

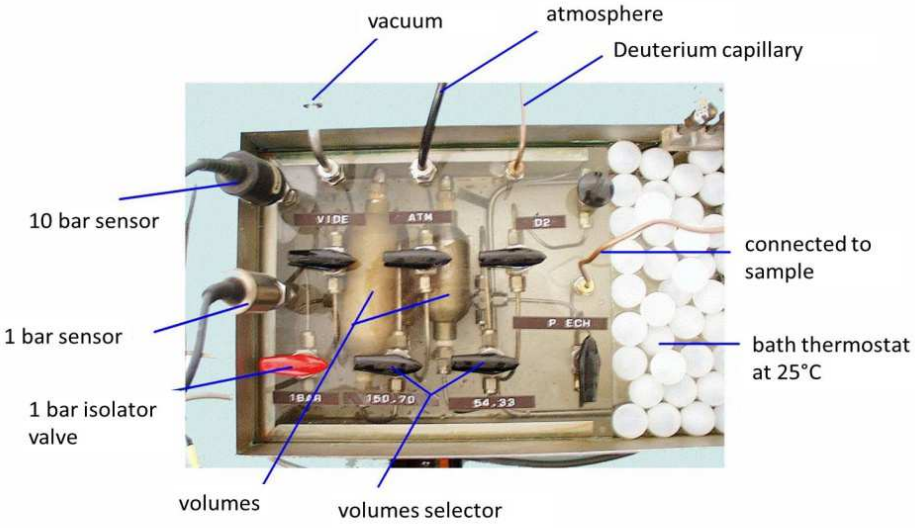

Figure 2-12 Sievert's manometric device for PCI curve

In the initial state, V_1 is filled with hydrogen and the pressure is P_i. When V_2 is open for hydrogen access, the sample is expected to absorb hydrogen till a stable final pressure is reached at P_f. The amount of hydrogen absorbed is given by the formula:

$$\Delta n = \frac{P_i V_1}{Z_{i,T} RT} - \frac{P_f (V_1 + V_2)}{Z_{f,T} RT} \quad (2\text{-}4)$$

at the measurement temperature T. $Z_{i,T}$ and $Z_{f,T}$ are the hydrogen compressibility considering the real gas properties rather than ideal gas, which is realized using Hemmes method [78]. To continue the test in an iteration manner, the final state can be the initial state for the next step. Eventually a PCI curve can be obtained. A Sievert's manometric device is presented in Figure 2-12.

In the current work, the samples with the composition $(TiH_2)_{1.5}Mg_{0.5}Ni$ were tested using the Sievert's method. ~0.5 g of powder sample was introduced into the sample holder closed with a stainless steel filter. The temperature was measured by a thermocouple fixed on the external wall of the sample holder. Every hydrogenation was preceded by 3 activation cycles at 620 K under 3 MPa of hydrogen pressure (absorption) and primary vacuum (desorption). PCI (pressure composition isotherms) curves were obtained by successive addition of hydrogen in the sample. Hydrogen content is read when the equilibrium pressure is reached. The temperature ranged from 298 K to 473 K and absorption and desorption pressures used were 0.8 MPa and 0.03 MPa. H-content was calculated from volumetric measurements.

2.3.2 Charge/discharge under galvanostatic conditions

The electrochemical performance of the metal hydrides is measured under galvanostatic conditions at room temperature using a one compartment open-cell.

For the test of the sample $Ti_{2-x}Zr_xNi$ and $(TiNi)_{1-x}Mg_x$, discharge capacity cycling were operated under galvanostatic conditions with a Multi-channel Battery Interface model ATLAS 0461. Working electrodes were prepared by compressing the milled powder and 10 wt% of Ni powder under 326 MPa pressure to produce a small pellet, which was then put in between the nickel nets that act as current collectors. $NiOOH/Ni(OH)_2$ was used as the counter electrode and cut-off potential versus the reference electrode Hg/HgO was set at 0.7 V. The electrodes were measured in an H-type shape glass cell. Before the test, the electrodes were soaked in 6 M KOH electrolyte at room temperature before they were soaked in the same solution for 1 h at 100°C. An illustration of the experimental components is shown in Figure 2-13.

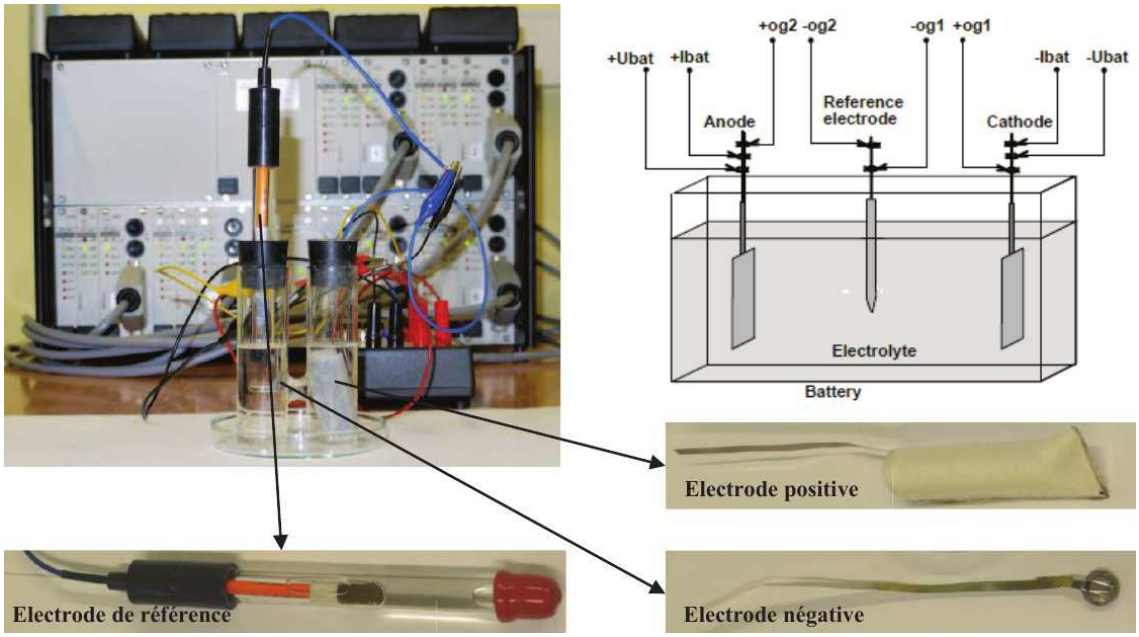

Figure 2-13 Experimental components for the electrochemical cycling test for the sample $Ti_{2-x}Zr_xNi$

For the sample $(TiH_2)_{1.5}Mg_{0.5}Ni$, the cell consist of a negative working electrode pellet made by hard pressed the milled powder, a positive $Ni(OH)_2/NiOOH$ counter electrode and a Hg/HgO reference electrode (Figure 2-14). The working electrodes were made of a mixture of the sample powder,

conductive carbon, and Polytetrafluoroethylene (PTFE) in the weight ratio 90:5:5, which was rolled onto a Ni grid acting as the current collector. The discharged capacity was calculated corresponding to the active material. 6 M KOH solution was used for both electrochemical cell and reference electrode. The cycling tests were performed at C/5 regime with cut-off potential at 0.7 V versus the reference electrode in discharge session. To obtain electrochemical isotherms, Galvanostatic Intermittent Titration Technique (GITT) was performed at room temperature with 5 h relaxation time. The electrochemical experiments were completed on a Mac Pile II device.

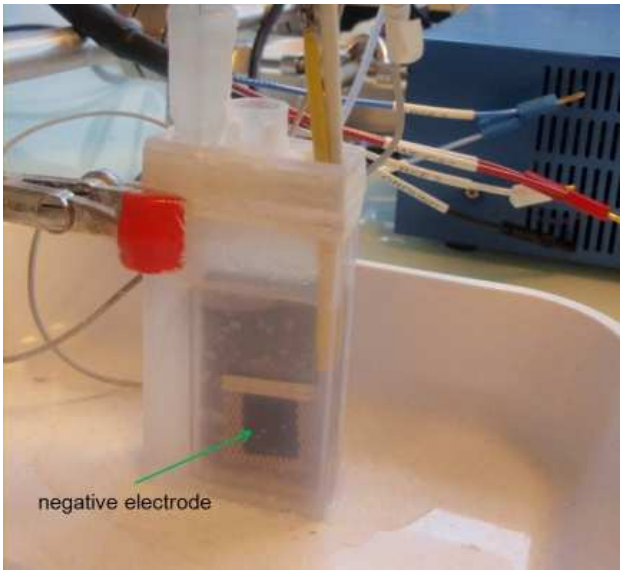

Figure 2-14 The battery set-up using the $(TiH_2)_{1.5}Mg_{0.5}Ni$ sample as the negative electrode

2.4 Density functional theory

Density functional theory was developed to investigate the electronic structure in atoms, molecules and condensed phases as a computational approach nowadays. Heavily relied on computer nowadays, it is frequently used in solid state physics and quantum chemistry to solve the time-independent, non-relativistic Schrödinger equation:

$$\hat{\mathrm{H}}\Psi(r_1, r_2, r_3, \ldots, r_n; R_1, R_2, R_3, \ldots, R_M) = E\Psi(r_1, r_2, r_3, \ldots, r_n; R_1, R_2, R_3, \ldots, R_M) \quad (2\text{-}5)$$

where $\hat{\mathrm{H}}$ is the Hamiltonian for a system consisting of M nuclei and n electrons, r_i is the position of the electron, R_1 is the position of the nuclei. To solve this extremely complicated equation in a many-body electronic structure calculation, Born–Oppenheimer approximation which treats nuclei of molecules or clusters as fixed is applied. Thus the above equation becomes:

$$\hat{\mathrm{H}}\Psi(r_1, r_2, r_3, \ldots, r_n) = E\Psi(r_1, r_2, r_3, \ldots, r_n) \quad (2\text{-}6)$$

Nevertheless, the task of solving the above equation is still formidable after the simplification due to the interactions between the massive numbers of electrons. This is where DFT kicks in, which uses the electronic density distribution, n(r) and a universal functional of the density $E_{xc}[n(r)]$. The key theory consists of two parts:

1) The ground state electron density uniquely determines the potential and therefore all properties of the system.

2) A functional F[n(r)] can be found for the ground state energy for any given $V_{ex}(r)$

The above theorems are also known as the Hohenberg-Kohn theorem, which has turned the many-electron problem to self-consistent one electron form. It is still left to decide the $E_{xc}[n(r)]$ (exchange-correlation energy functional), which can be calculated by

$$n(r) = \sum_i |\Phi_i(r)|^2 \quad (2\text{-}7)$$

where Φ_i is the concerning wave function. There are several approximation methods, and are still being improved. E.g. the local spin density approximation (LDA) is expressed as:

$$E_{xc}^{LDA} = \int n(r)\, \varepsilon_{xc}[n(r)] d^3r \qquad (2\text{-}8)$$

Simple as LDA is, it is mostly accurate when describe atomic structure for many systems, but it suffers inaccuracy when trying to describe energetics of chemical reactions. Another approximation method named GGA (generalized gradient approximation) was developed, which depends on not only the local density but also the spatial variation of the density. It is written as:

$$E_{xc}^{GGA} = \int n(r)\, \varepsilon_{xc}[n(r)] F_{xc}[n(r), \nabla n(r)] d^3r \qquad (2\text{-}9)$$

DFT is realized by many quantum chemistry and solid state physics software packages, including vasp, castep, quantum ESPRESSO etc.

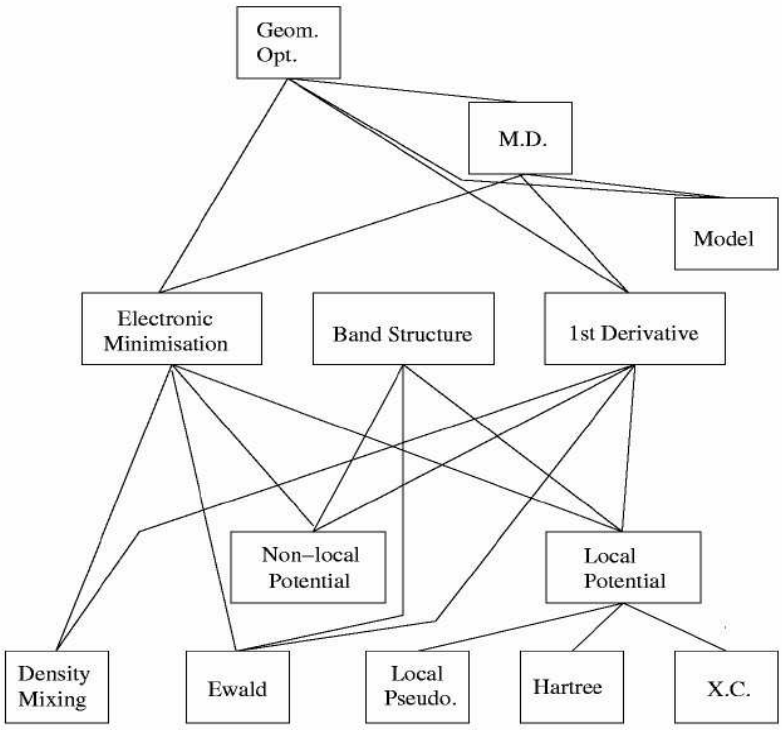

Figure 2-15 Functional modules of castep

Castep is a versatile first principles electronic structure code for predicting properties of materials. Some of its function include: total energies (forces, stresses, elastic constants), electronic structure (electronic charge, potential, band structure, DOS, atomic popluations), geometry optimization (atomic positions, cell parameters, external pressure/stress), transition state searches (chemical reaction pathways, diffusion barriers). The relationship between its functional modules can be illustrated as in Figure 2-15. In the current study, castep [79] is used for both the geometry optimization and energy calculation. The detailed parameters of calculation will be given with each instance in the following chapters.

Chapter 3 High Energy Ball Milled $(Ti\text{-}Ni)_{1-x}Mg_x$ and $(TiH_2)_{1.5}Mg_{0.5}Ni$

Alloys of Ti, Ni, and Mg have drawn extensive interests as one of the most studied metal hydrides [60-62, 65, 80], since Ti and Mg potentially possess large amount of hydrogen storage capacity. Nonetheless, due to different preparation techniques and parameters, as well as the various products after synthesis, a conclusive explanation on how the alloying actually progresses and the true phases obtained are lacking. Among the three elements, Ti and Mg are in fact thermodynamically immiscible, whereas different structures of them have been reported without revealing the true compositions [81, 61, 63].

In the current chapter, different amount of Mg doped Ti-Ni samples were submitted to high energy ball milling with the composition $(TiNi)_{1-x}Mg_x$ (x = 0, 0.1, 0.2, 0.3). The milling time is fixed at 40 h for the sample with Mg addition. Effect of Mg on both the microstructure and reversible hydrogen capacity was studied. A DFT calculation was carried out and a Ti-Mg FCC structure is proposed. In the second step, powders of TiH_2, Mg and Ni with the molar ratio of 3:1:2 ($(TiH_2)_{1.5}Mg_{0.5}Ni$) are mechanically milled for different hours (10-40 h). The evolution of microstructures with milling time helps further understand the formation of Ti-Mg alloy and its hydride. Solid-gas reaction of the milled sample with hydrogen and electrochemical cycling under galvanostatic conditions reveal the hydrogenation properties of the Ti-Mg alloy.

3.1 Microstructures of the milled $(TiNi)_{1-x}Mg_x$

To have a better understanding of the Mg influence on the milling of Ti50-Ni50, the XRD patterns of Ti50-Ni50 powders milled 10 h, 20 h, 40 h and non-milled samples are displayed in Figure 3-1. Note that in the as-purchased Ti50-Ni50, Ti, Ni element peaks are not observed except for those of the Ti-Ni compounds (TiNi and Ti_2Ni), which means that the Ti50-Ni50 is not a mix of pure element powders but Ti-Ni compounds with the Ti, Ni atoms ratio of 1:1.

In all mille samples, a typical peak centered at 42° can be observed as this peak is common for the TiNi alloy [68, 51]. What is interesting is however the Ni element peaks spotted for the 20 h milled sample, which implies the decomposition/recrystallization for the Ti-Ni compounds. As mechanical milling can induce dynamical recrystallization during nano-crystal formation at high milling intensity [75], it appears that after about 20 h of milling, dynamical recrystallization has taken place. Trace of Ti-Fe-O compound was also found uniquely for the 20 h milled sample, in which iron contamination should be from the steel milling balls. This further confirmed the recrystallization during milling. As milling time is prolonged to 40 h, the Ni peaks seen in the 20 h disappear while the prominent peak at 42° becomes smoother, showing a sign of amorphization of TiNi phase. This indicates Ni has re-alloyed with Ti in the following 20 h of milling.

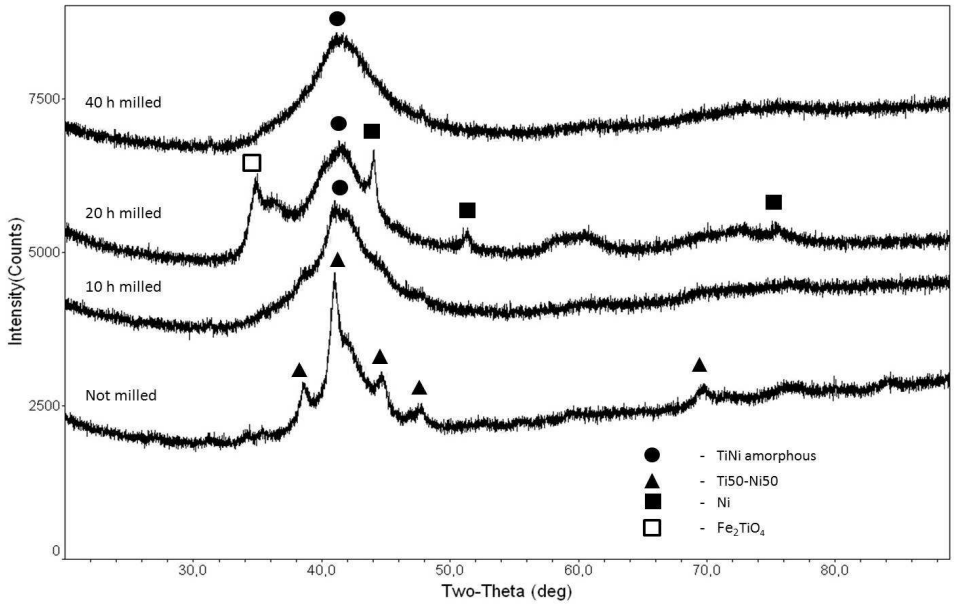

Figure 3-1 XRD patterns of Ti50-Ni50 milled 0 h, 10 h, 20 h, 40

Comparable XRD patterns of the Mg doped samples were shown in Figure 3-2. Although all these samples were milled 40h, addition of Mg has apparently hindered the amorphization progress since all phases incline toward

crystallization with the increase of Mg content. When x reaches 0.3 the peaks become much narrower than the samples with less Mg. On the other hand, all Mg doped samples consist of peaks appear in the same angle, indicating the samples share the same phases. Particularly, no known Ti-Ni binary structure could be found that corresponds to the peak at 37° except that the other three peaks at the higher angles fit well into the TiNi BCC profile. It is therefore inferred that the peak at 37° corresponds to a phase containing Mg. Intensity of this very peak increases with Mg content further confirms this assumption.

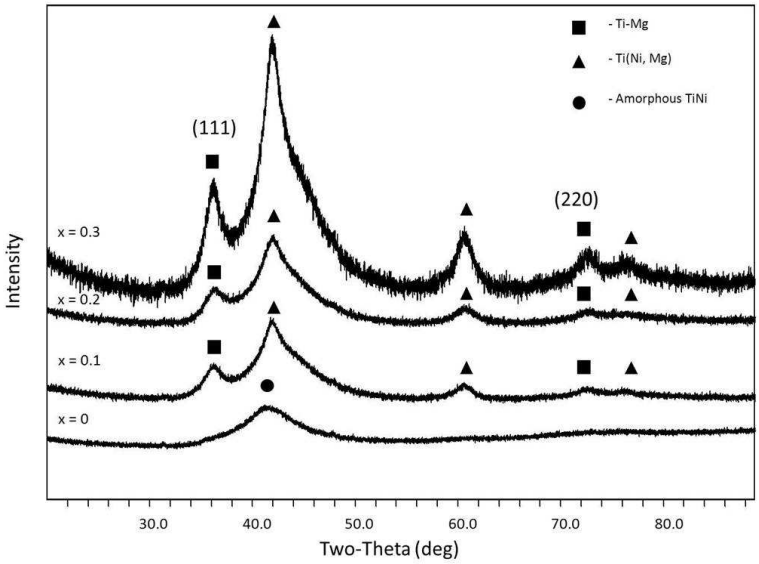

Figure 3-2 XRD patterns of $(TiNi)_{1-x}Mg_x$ (x =0, 0.1, 0.2, 0.3) milled 40 h.

Therefore, XRD profile fitting was performed on the sample $(TiNi)_{0.7}Mg_{0.3}$ shown in Figure 3-3. After multiple steps of careful profiling, the peak at 42° was found to be composed of two individual peaks. One is a considerably broad peak identified as the TiNi BCC nanocrystalline/amorphous phase, while the other is a much sharper peak that appears to be rather crystalline phase. It also reveals that the peak at 37° belongs to an FCC phase. Indexation of the peaks is presented in Table 3-1. It is necessary to note that the

peaks starting from 60.6° to higher angles are two phases heavily overlapping each other. This Mg-rich peak at 37° in the Ti-Ni-Mg ternary has been reported by both Rousselot et al. [65] and Kalisvaart et al. [59]. The former suggested that this peak should belong to a Ti-Mg HCP structure, which could transform to FCC when hydrogenated, while the latter reported that the peak originates from an FCC structure of Ti-Mg with a lattice constant *a* of 4.26 Å. In our case, the XRD pattern fits perfectly to an FCC structure with the lattice constant *a* of 4.325 Å, labeled as the β phase in Figure 3-3. The BCC pattern labeled as the α phase with the lattice constant *a* of 3.044 Å is determined to be TiNi (CsCl type), whose lattice constant is slightly larger than the frequently reported value 3.015 Å. This may be caused by inaccuracy of profiling, or substitution of Mg for Ni in the Ti-Ni BCC cell [5]. The average crystallite size for $(TiNi)_{0.7}Mg_{0.3}$ is ~3 nm according to calculation with Wilson formula following Williamson–Hall style plot [81].

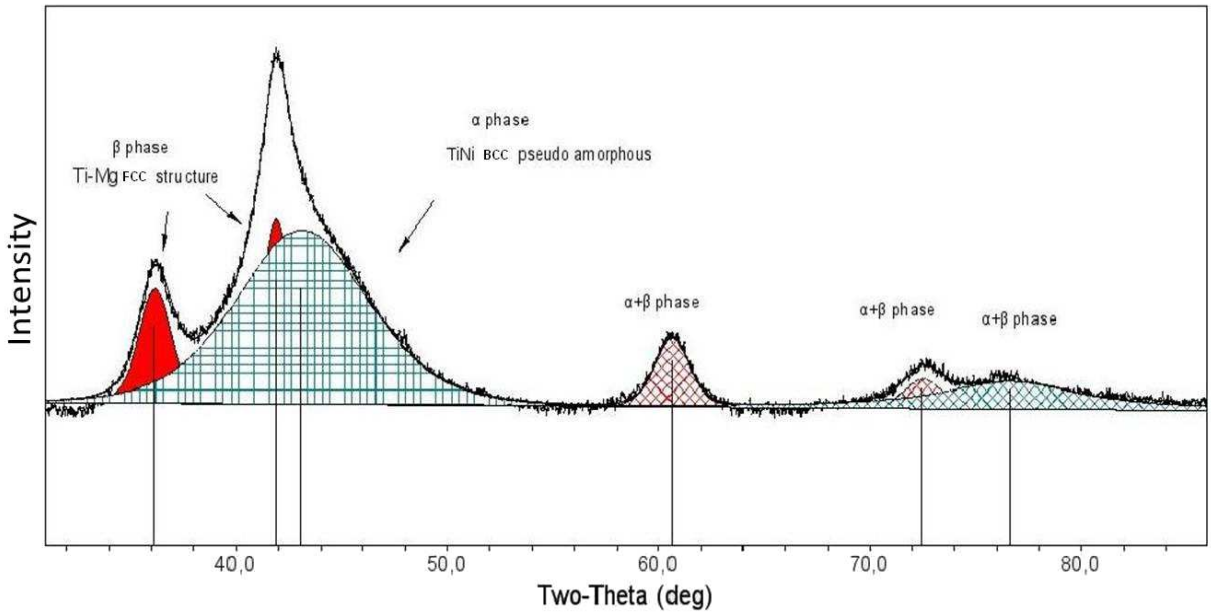

Figure 3-3 XRD profiling for $(TiNi)_{0.7}Mg_{0.3}$ (milled 40 h).

Table 3-1 Peak indexing for the $(TiNi)_{0.7}Mg_{0.3}$ milled 40 h (* indicates overlapping of peaks from the two phases)

Phases	2θ (°)	Reflection (hkl)
TiMg FCC	36.1	(111)
	41.9	(200)
	60.6*	(220)
	72.4*	(311)
	76.4*	(222)
TiNi BCC	43.2	(110)

Despite the scarcity of Mg compared to the relatively abundant Ti or Ni, it appears that Ti favored Mg to alloy instead of Ni. Interestingly, this was also reported by Rousselot et al. [65] when they ball milled Ti, Ni, Mg element powders. The morphologies of the milled samples are shown in the SEM micrographics (Figure 3-4). In Figure 3-4 (a), the morphology presented implies a cold welding state or amorphous state to be exact, which usually occurs as the consequence of particles being excessively refined by fracturing and subsequent agglomeration. In comparison, two distinct types of particle can be found in Figure 3-4 (b): the bulky particles which are the same type as in Figure 3-4(a), and the small ones residing on the surface of the former. Since the bulky particles correspond to amorphous TiNi, the smaller particles have to be the new phase containing Mg, the β phase. Relate the analysis of SEM and XRD, we can deduce the events in chronological order during the milling of Ti-Ni-Mg alloy. During the 0 h - 20 h period, Ti50-Ni50 decomposes as the result of dynamical

recrystallization and Ti-Mg β phase starts to form. This recrystallization process does not exclude the formation of TiNi, which is refined and evolves into the nanocrystalline/amorphous state with further milling. When the milling time reaches 40 h, there coexist the amorphous TiNi and FCC Ti-Mg phase. We must stress that we have observed the "coating" effect by Ti-Mg β phase on TiNi α phase in all SEM micrographs for Ti-Ni-Mg ternary alloys, as this seems to have considerable influence on the hydrogen capacity of the alloy.

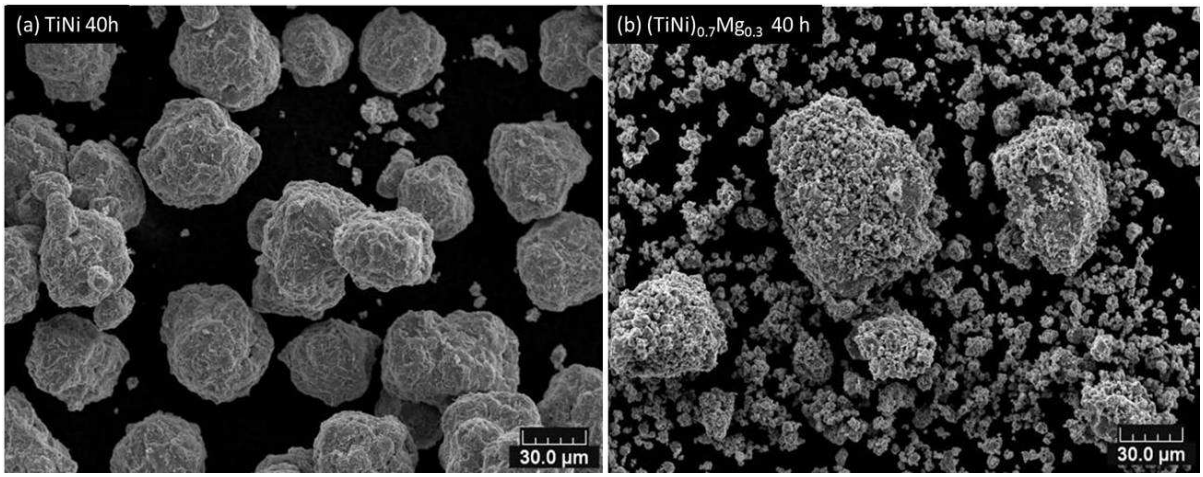

Figure 3-4 SEM micrographs of (a) TiNi and (b) $(TiNi)_{0.7}Mg_{0.3}$ milled 40 h.

In order to understand the milling products of Ti-Mg-Ni, the results of ours are compared with other groups using different synthesis conditions in Table 3-2. It can be seen that for the samples with PCA addition during milling, Ti-Mg FCC structure with the lattice constant *a* 4.42 Å is always present. However if PCA is not used but the milling balls change from steel to Zirconia, the same FCC structures is present. TiC was once suspected to be the source of this FCC structure for it has a similar lattice constant (4.37 Å), however formation of TiC has been proved false [61]. The formation of FCC was also suggested be triggered by the impurity of starting powders, such as oxidized Mg. Nonetheless, EDX assisted SEM analysis shows that for all the Ti-Ni-Mg

samples, they are homogeneous in composition, and the amount of oxygen is too low to be detected at all.

Table 3-2 Products of alloying Ti-Mg with different approaches

Composition	Synthesis	PCA/Balls	Products for Ti-Mg
$Mg_{0.75}Ti_{0.25}$ [63]	MA of Ti, Mg powders	Steel/Stearic acid	FCC *a* = 4.42 Å / *a* = 4.26 Å
	MA of Ti powders, Mg ribbons, Pd as catalyst	Steel/Non	FCC *a* = 4.42 Å
$(Mg_{0.75}Ti_{0.25})_{0.95}Ni_{0.05}$ [59]	MA of Mg ribbons, Ti, Ni powders	Steel/Non	
MgTi [64]	MA of Ti, Mg powders, Pd as catalyst	Steel/Non	BCC (84%) *a* = 3.39 Å HCP (16%) *a* = 2.97 Å, *c* = 4.86 Å
$(Mg_{0.80}Ti_{0.20})_{0.95}Ni_{0.05}$ [58]	MA of Ti, Mg powders	Steel/Graphite	FCC *a* = 4.44 Å / *a* = 4.25 Å
$(TiNi)_{0.7}Mg_{0.3}$ (present work)	MA of Ti-Ni, Mg powders	Steel/Alcohol	FCC *a* = 4.325 Å
$Mg_{0.75}Ti_{0.25}$ [59]	As deposited to thin film	N/A	HCP *a* = 3.11 Å, *c* = 5.02 Å
$Mg_{0.65}Ti_{0.35}$[62]	MA of Ti, Mg powders	Steel/Non	HCP *a* = 3.17 Å, *c* = 5.15 Å BCC *a* = 3.42 Å
$Mg_{0.65}Ti_{0.35}$[62]	MA of Ti, Mg powders	Zirconia/Non	HCP *a* = 3.19 Å, *c* = 5.20 Å FCC *a* = 4.23 Å,

3.2 DFT calculation on Ti-Mg structure

3.2.1 Calculation parameters

The unit cells used for DFT calculation are displayed in Figure 3-5 and Figure 3-6. Perdew–Burke–Ernzerhof (PBE) [82] generalized gradient approximation (GGA) was used for the exchange and correlation potential. Transition metal Ni was treated with spin polarized. Ultrasoft pseudo potentials

[83] in reciprocal space were used to replace core electrons. Dependence of total energy on the energy cutoff values and the k-point sets was tested in advance, which shows that when the cutoff energy is higher than 380 eV or the k-point set is larger than 6 × 6 × 6 (and 10 × 5 × 5 for HCP), change in total energy is less than 1.64 meV/atom. Therefore, all geometry optimization calculations were performed with 380 eV cutoff energy and 6 × 6 × 6 (10 × 5 × 5 for HCP) k-points sets. Convergence criteria were as follows: 5.0×10^{-6} eV/atom for energy change, 0.01 eV/Å for maximum force, 0.02 GPa for maximum stress and 5.0×10^{-4} Å for maximum displacement.

Enthalpy of formation for all alloys is defined as:

$$\Delta_f H = E_{tot}(Ti_xNi_yMg_z) - [xE(Ti, HCP) + yE(Ni, FCC) + zE(Mg, HCP)]$$

where $\Delta_f H$ and E_{tot} refer to the enthalpy of formation and total energy per unit cell of the compound respectively. E(Ti, HCP), E(Ni, FCC), and E(Mg, HCP)] are the single atomic energies of the pure element in their stable solid states. Zero-point-energy (ZPE) contributions are not considered since no hydrogen molecules were involved in these simulations [82]. Finally, favored structures are decided by comparing the enthalpy of formation per atom, the indicator of thermodynamic stability.

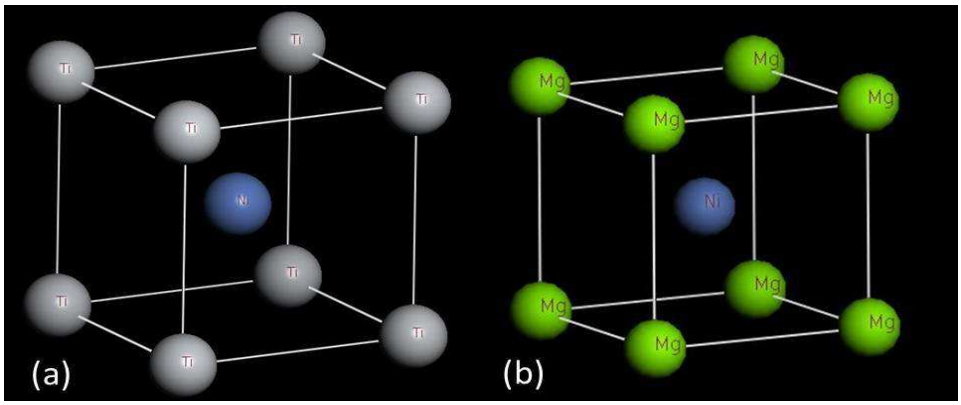

Figure 3-5 Unit cells of TiNi BCC (a), and MgNi BCC (b), initial lattice constant *a* at 3.015 Å.

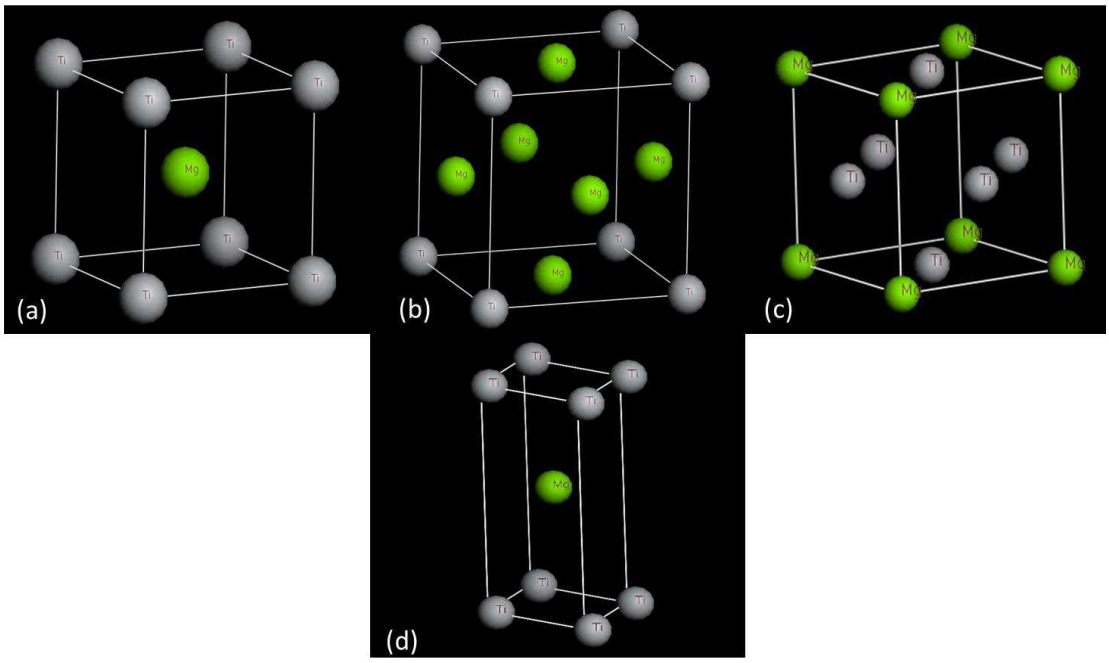

Figure 3-6 Unit cell of TiMg BCC (PM-3M) (a), $TiMg_3$ FCC (PM-3M) (b), Ti_3Mg FCC (PM-3M) (c) and TiMg HCP (P-6M2) (d).

3.2.1 Thermodynamics of the Ti-Mg-Ni structures by DFT

As shown Figure 3-6 (b) and (c), the $AuCu_3$ structure is chosen as the Ti-Mg FCC structure candidates with the composition of $TiMg_3$ and Ti_3Mg respectively. Other hypothetical structures include TiMg BCC (Pm-3m) (Figure 3-6 (a)), and TiMg HCP (P-6m2) (Figure 3-6 (d)) structures. The initial geometry parameters are chosen following the parameters of the Ti-Mg structures reported by other research groups (references can be found in Table 3-3). The lattice parameters of the $AuCu_3$ structured $TiMg_3$ were based on the final FCC phase obtained in the sample $(TiNi)_{0.7}Mg_{0.3}$.

Geometry optimizations were performed with full optimization before energy calculations. Table 3-3 lists both calculated and experimental values. It is found that the discrepancies of lattice constants between the calculated values and experimental data after geometry optimization are below 5% for all results. Especially, the difference in lattice constant *a* is less than 0.9% for the $AuCu_3$

structured $TiMg_3$. Therefore, calculations on enthalpy of formation were continued with above configurations.

Table 3-3 Experimental and calculated lattice parameters for Ti-Ni-Mg compounds

Structures	Lattice constant (Å)	
	Experimental	Calculated
TiNi BCC	3.015	3.016
Ti(Ni, Mg) BCC	3.044	N/A
TiMg BCC	3.39 [65]	3.366
MgNi BCC (hypothetical)	N/A	3.059
Ti-Mg FCC	4.325	$TiMg_3$ 4.366
		Ti_3Mg 4.164
TiMg (HCP)	a =3.11, c = 5.02 [60]	a = 2.908, c = 5.265

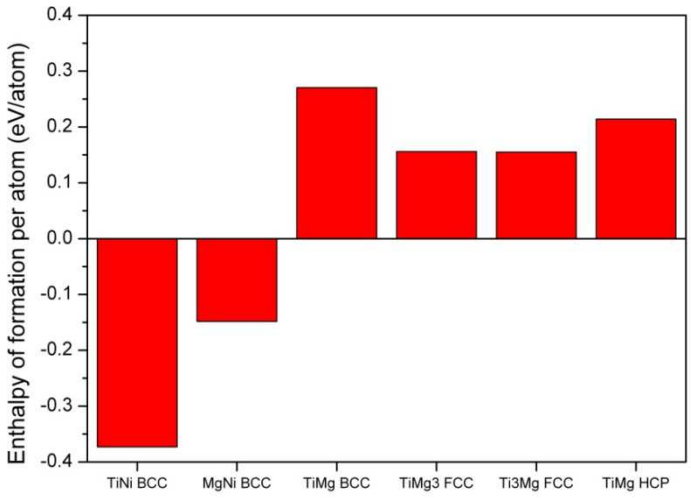

Figure 3-7 Enthalpies of formation per atom for TiNi BCC, MgNi BCC, TiMg BCC, $TiMg_3$ FCC, Ti_3Mg FCC and TiMg HCP.

Figure 3-7 illustrates the enthalpy of formation per atom for each alloy for comparison. From high to low, the thermodynamic stability is in the following order: TiNi BCC (-0.373 eV/atom), MgNi BCC (-0.148 eV/atom), Ti_3Mg (0.155

eV/atom), $TiMg_3$ (0.156 eV/atom), TiMg HCP (0.214 eV/atom), TiMg BCC (0.270 eV/atom). Expectedly, all Ti-Mg structures have positive values regarding enthalpy of formation, since Ti-Mg phase does not exist in their binary phase diagram. Nonetheless, the disconcerting fact is that during most milling practices concerning Ti-Ni-Mg, Ti favors Mg instead of Ni when alloying, whereas both TiNi and Mg_2Ni should be more predictable products compared to the Ti-Mg alloys. This has to be explained by the nature of mechanical alloying, which is known for producing metastable phases. Even after exceedingly long milling time, the final product is not necessarily the most stable phase available. Yavari et al. [83] measured the departure energy from equilibrium in one of their ball milling experiment and reported a 30 kJ/mol (~ 0.311 eV/atom) offset to the equilibrium state.

By comparing the geometry parameters of two Ti-Mg FCC structures, clearly the major FCC phases obtained in the present work consist of $TiMg_3$ instead of Ti_3Mg. The difference in enthalpies of formation between the two structures is extremely small (0.001 eV/atom) and can be disregarded. As for TiMg BCC and TiMg HCP, they were not detected in the samples from the present work. And their much higher enthalpies of formation compared to the Ti-Mg FCC structures may require much more departure energy to be produced.

3.3 Electrochemical capacities on cycling for $(TiNi)_{1-x}Mg_x$

The electrochemical discharge capacity against cycle number for Ti50-Ni50 is shown in Figure 3-8. The current density of charging/discharging is fixed at 40 mA/g. In general, discharge capacity increases with milling time from 10 h to 20 h, reaching the highest capacity at 131.7 mAh/g, but decreases when milling time is extended to 40 h. The sample milled only 10 h excels at first but the capacity drops soon after the third cycle. As it was stated earlier, the

recrystallization process takes place at 20 h of milling time, when α phase (TiNi BCC) forms and becomes the dominant phase. The highest discharge capacity is credited to the abundant TiNi phase. When milling is prolonged to 40 h, the grain size of TiNi can be significantly reduced as a result of repeatedly fracturing until an amorphous phase is finally developed. While amorphous TiNi facilitates hydrogen diffusion in respect to charging/discharging process, it leaves fewer hydrogen storage sites as a side effect, which causes overall capacity loss. Besides the different discharge capacities, it shows that the samples milled 20 h and 40 h exhibit an activation process in the first few cycles on contrary to the sample milled only 10 h. The activation process is usually caused by oxidation on the surface of the sample. This is consistent with the fact that longer milled samples possess larger surface due to finer particles.

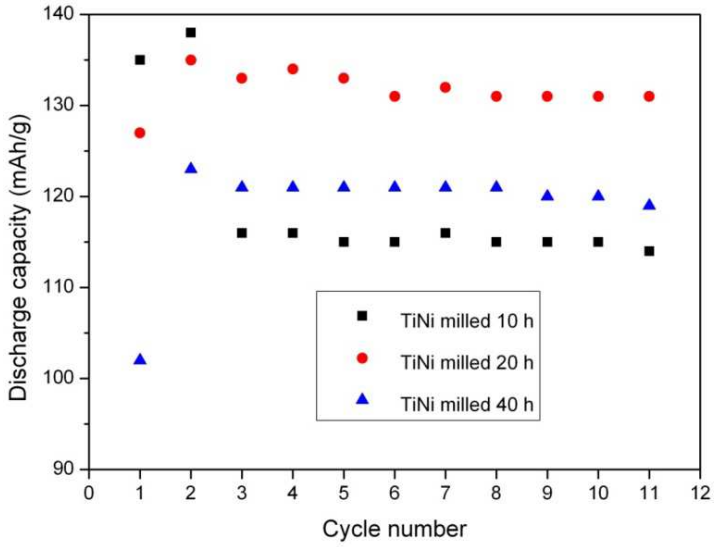

Figure 3-8 Discharge capacities against cycle numbers for Ti50-Ni50 milled 10 h, 20 h, and 40 h.

For the Mg doped Ti-Ni samples (Figure 3-9), the discharge capacities decrease monotonically with increasing Mg content, and witnesses a drop to mere 20 mAh/g when x = 0.3 (Figure 3-9) while maintaining cyclic stability. As

the proportion of Mg content is still relatively small in the composition, the negative influence of additional Mg to the electrochemical performance should be considered substantial. It is conclusive that the doping of Mg is deteriorative to the discharge capacity.

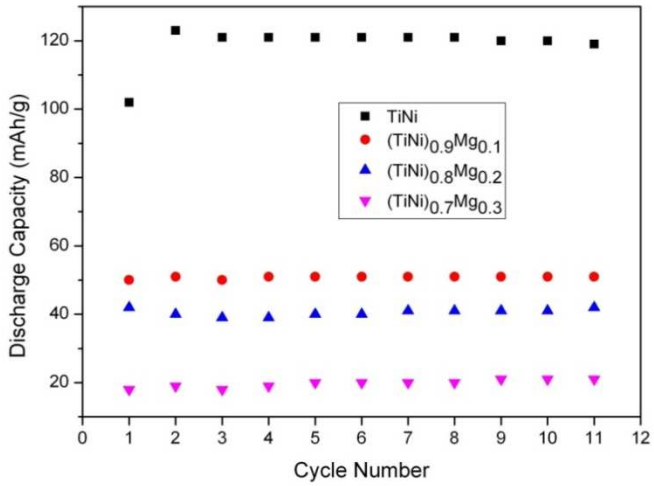

Figure 3-9 Discharge capacities against cycle numbers for $(TiNi)_{1-x}Mg_x$ (x = 0, 0.1, 0.2, 0.3) milled 40 h.

3.4 Discussion of Ti-Mg structure and its influence on hydrogen capacity

Evidences suggest that the new Ti-Mg β phase hardly contribute to discharge capacity, or even worse, since it covers on the surface of the TiNi phase, it has become the barrier to hydrogen transport. The discharge capacity contribution for the Mg doped samples may be ascribed solely to the TiNi phase, which has an unexceptional but rather stable discharge capacity in electrochemical cycling. In the study of Kalisvaart et al. [58], they saw two FCC structures by milling Ti-Mg, the lattice constants *a* of which are 4.25 Å and 4.44 Å respectively, and they both merged into one with the lattice constant *a* 4.33 Å with extended milling time. They concluded that only one of the FCC structure (with the larger lattice constant *a* (4.42 Å)) should contribute to the discharge capacity. In the present work however, only one FCC structure with the lattice

constant *a* of 4.365 Å is seen, which is quite close to that of the final product from the work of Kalisvaart et al. [58]. Unfortunately, the true structures of the two FCC structures before merging into one observed by them were not solved, and they neither fit perfectly with Ti_3Mg nor with $TiMg_3$, except that the $TiMg_3$ profile built by DFT calculation is almost identical to the final products of milling Ti-Ni-Mg in both this work and theirs. On the other hand, it is clear that the decrease in discharge capacity arises from the formation of $TiMg_3$ phase, which not only captures Ti and hence reduces the abundance of TiNi phase, but also blocks hydrogen transport. If we take inaccuracy of XRD data processing into consideration, it is reasonable to conclude that the $TiMg_3$ phase found in the present work corresponds mainly to the Ti-Mg FCC structure with the smallest lattice constant *a* at ~ 4.25 Å indexed by Kalisvaart et al. [58]. According to their findings, there should be another FCC Ti-Mg structure with a larger lattice constant which can provide hydrogen storage. It was reported earlier that it is a Ti-Mg HCP structure which can transform into an FCC structure upon hydrogenating Ti-Mg thin film ($Mg_{70}Ti_{30}$ and $Mg_{80}Ti_{20}$), and the lattice constant *a* for the hydrogenated Ti-Mg FCC is 4.66 Å [60]. Nonetheless, attempts on trying to build such Ti-Mg FCC structures with larger lattice constant seem to be impossible following DFT, as cell geometry optimization would always shrink the lattice constant *a* of $TiMg_3$ to 4.366 Å. Interestingly, with the study in the next part where the milling of $(TiH_2)_{1.5}Mg_{0.5}Ni$ is investigated, it does shed light on this Ti-Mg FCC problem.

3.5 Microstructures of the milled $(TiH_2)_{1.5}Mg_{0.5}Ni$

The Ti-Mg-Ni ternary alloys are continually studied with the mechanical milling of nominal $(TiH_2)_{1.5}Mg_{0.5}Ni$ for different duration, using TiH_2, Mg and Ni as the starting powders. Phase evolution with milling time is considerably revealing to the formation of the Ti-Mg FCC phase. Hydrogen properties

investigated is significant to the understanding of the hydrogenation behavior of the Ti-Mg FCC phase.

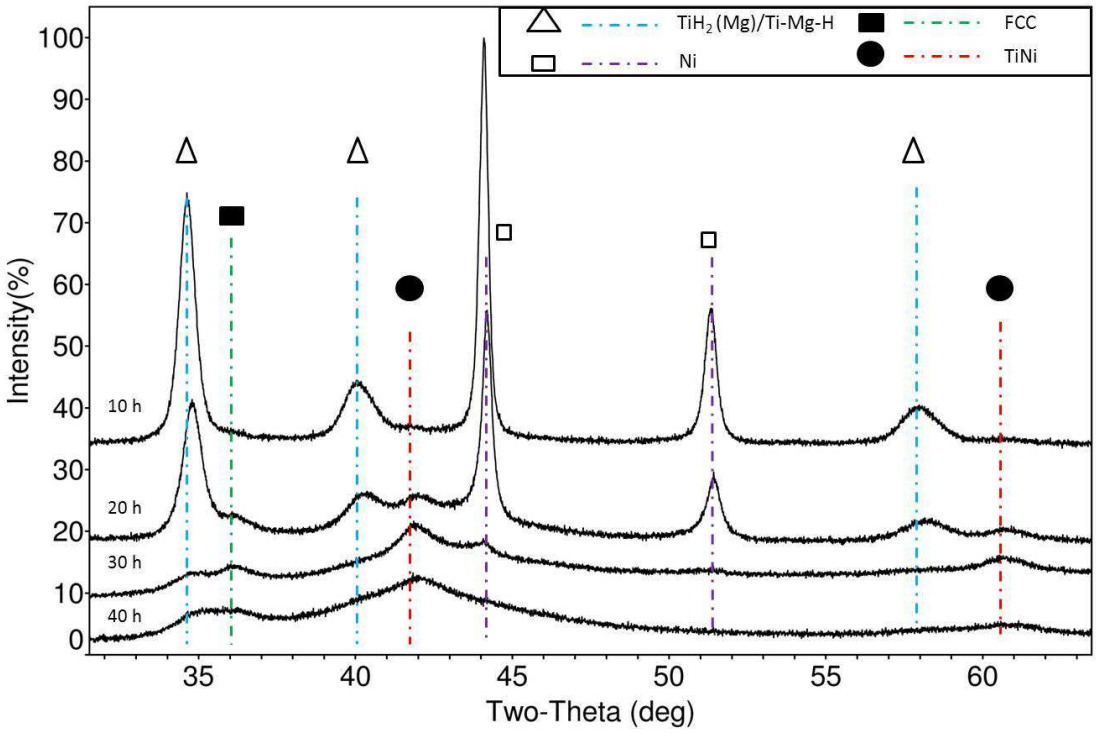

Figure 3-10 XRD patterns of $(TiH_2)_{1.5}Mg_{0.5}Ni$ milled 10 h, 20 h, 30 h and 40 h. Lines with colors are drawn to represent peaks at the same diffraction angles. Empty symbols correspond to the peaks of reactants and full symbols correspond to the new structures after milling.

Nominal $(TiH_2)_{1.5}Mg_{0.5}Ni$ was mechanically milled for 10 h, 20 h, 30 h and 40 h and the XRD patterns are presented in Figure 3-10. After only 10 h of milling, it is found that Mg peaks have disappeared despite its 16.7% weight account in the mixture, whereas peaks of TiH_2 (FCC) and Ni remain significant except for some broadening. It suggests that the alloying degree is still low at current stage, while Mg may have dissolved considerably fast in solid solution. There was previous report that Mg dissolves into TiH_2 lattice under milling condition [84]. With the increase of milling time, intensities of peaks become rather complicated. Firstly, a new FCC phase is slowly forming, notably starting

from the sample milled 20 h. This FCC phase with a lattice constant *a* 4.22 Å can be identified by its particular peak at 36.1° (2theta), which is also reported by several other authors in their millings of Ti-Mg alloy [36, 61, 64, 65]. As Mg peaks vanish completely, by comparing with the Ti-Mg FCC structure obtained by previous studies, it can be inferred that the new FCC phase is Ti-Mg with the lattice constant *a* 4.22 Å. According to our previous study, Ti-Mg FCC have the lattice constants at 4.37 Å for $TiMg_3$ and 4.16 Å for Ti_3Mg [36]. As 4.22 Å is closer to the value of Ti_3Mg, it shows that in this Ti-Mg FCC phase Ti shares the higher ratio, which is consistent with the initial powder composition that Ti is larger than Mg in quantity. It is found that the intensities of TiH_2 and Ni do not show obvious decrease until beyond 30 h. Considering the starting ratio of Ti, Mg, Ni being 3:1:2, one can infer that all Mg has been consumed in the reaction with TiH_2 in the 20 h time mark. The reaction between TiH_2 and Ni is assumed to start only after about 20 h of milling. As we examine the XRD pattern using the TiNi peak profile, their peaks are found to be overlapped heavily by the new Ti-Mg FCC phase. To illustrate this matter better, a singled out XRD pattern of $(TiH_2)_{1.5}Mg_{0.5}Ni$ milled 40 h is presented in Figure 3-11, in comparison with the sample $(TiNi)_{0.7}Mg_{0.3}$. The cubic TiNi (CsCl type) with the lattice constant *a* 3.015 Å is found to share the same peaks at 42.1°, 61.8°, 72.9°, which correspond to the (200), (220), (222) face of the FCC phase. Thus, determination of the existence of cubic TiNi phase is critically decided by the sudden intensity decline of Ni peaks. It is necessary to continue the discussion of the new FCC phase more, as one may argue that this FCC phase may as well be Ti-Mg-H rather than Ti-Mg. The lattice constant of the FCC phase obtained from different authors are listed in Table 1-2. Apparently, Ti-Mg-H all have a larger lattice constant. Moreover, according to the DFT (density functional theory) calculations, the Ti-Mg-H FCC structure is suggested to have a lattice constant *a* of 4.59 Å ($TiMg_3$) [85], while Ti-Mg FCC have smaller lattice

constants, 4.37 Å for $TiMg_3$ and 4.16 Å for Ti_3Mg [36]. As shown in Table 1, the group of Asano et al. reported that the lattice constant *a* for $Ti_{0.75}Mg_{0.25}H_{1.62}$ synthesized via milling was 4.46 Å [89]. Interestingly, in the milling of Ti + MgH_2, TiH_2 + Mg, and TiH_2 + MgH_2, Rousselot et al. [87] observed two FCC phases with the lattice constants of ~4.47 Å and ~4.25 Å. In the current study, the sample milled 40 h contains two FCC phases with the lattice constant *a* of 4.22 Å and 4.44 Å. It is therefore decided that the FCC structure with the lattice constant a 4.44 Å to be the Ti-Mg-H phase after comparison with the report of ~ 4.46 Å [89] and ~ 4.47 [87]. When one compares Ti-Mg-H peaks in Fig. 1 with different milling time, a shift to the right of peaks with increased milling time can be observed, implying minor lattice constant decrease (from 4.46 Å to 4.44 Å). This phenomenon can be expected since Ti-Mg-H has already formed after merely 10 h of milling due to fast dissolution of Mg into the TiH_2 phase, while further milling induced gradual transformation of Ti-Mg-H to the Ti-Mg FCC phase. That the TiNi phase promotes the dissociation of hydrogen in the Ti-Mg-H phase is further discussed in the hydrogenation properties section in the following part of this study.

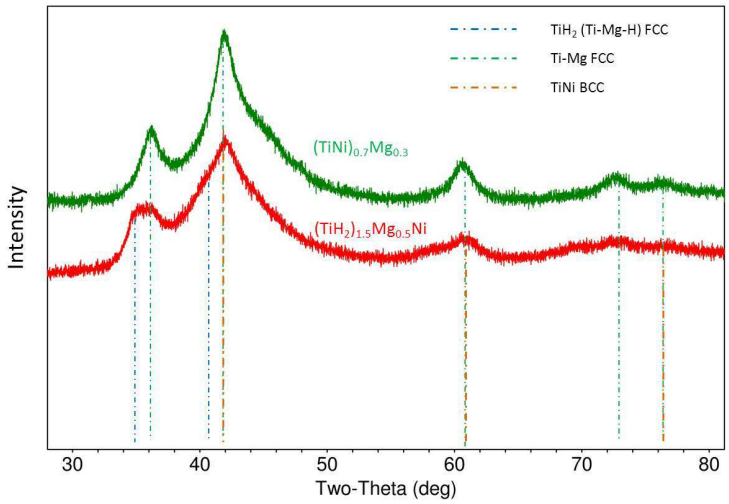

Figure 3-11 Comparison of XRD patterns between $(TiNi)_{0.7}Mg_{0.3}$ and $(TiH_2)_{1.5}Mg_{0.5}Ni$ milled 40 h.

To summarize, reactions took place with the following events: Mg starts to dissolve into the TiH_2 lattice at the early stage of milling (TiH_2 + Mg → Ti-Mg-H). With milling time, dehydrogenation accompanies the formation Ti-Mg-H as well which produces the new FCC phase of Ti-Mg with the lattice constant *a* of 4.22 Å. From 20 h to 30 h, almost all Mg has alloyed with TiH_2, whereas the remaining TiH_2 begins to alloy with Ni to form the cubic TiNi phase. After 40 h of milling, final phases present can be decided as the Ti-Mg FCC phase, TiNi cubic phase and residual TiH_2 phase. Note that the so-called TiH_2 phase in the final stage may contain Mg as well in the form of Ti-Mg-H phase, since the conversion proportion of Ti-Mg-H FCC to Ti-Mg FCC is not known.

From the thermodynamic perspective, this result again shows that Ti-Mg alloying is favored over Ti-Ni alloying under milling condition, which is consistent to our previous study where Mg and TiNi were milled together but the metastable Ti-Mg FCC phase was produced [36]. By comparing the products of Ti-Mg alloying practices, we found that two main factors play a critical role on the production of the Ti-Mg FCC phase. First, changing the material of milling ball from steel to ZrO resulted in the production of FCC phase (Table 3-2). Second, the use of PCA leads to the formation of Ti-Mg FCC phase [36]. In both current and our previous study [36], the obtained Ti-Mg FCC phase should be attributed to the use of process control agent (PCA).

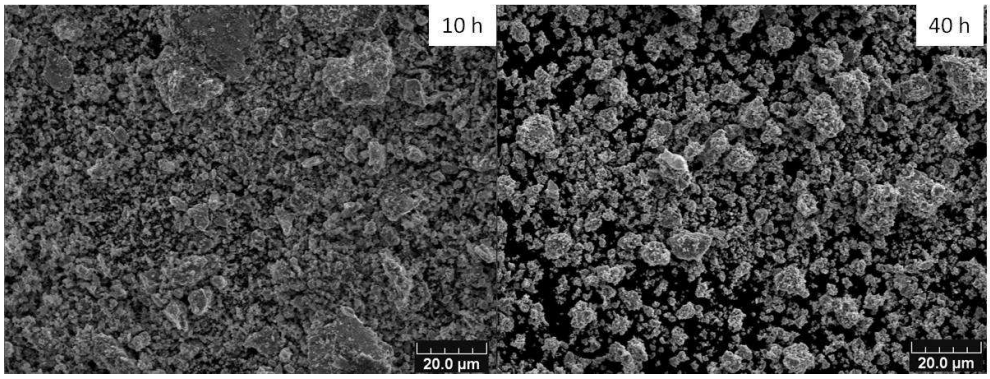

Figure 3-12 SEM micrographs for $(TiH_2)_{1.5}Mg_{0.5}Ni$ milled 10 h and 40 h.

Comparable SEM micrographs are shown in Figure 3-12: for the sample milled 10 h and 40 h. In general, two different kinds of morphologies can be seen for the 10 h sample. One kind is with cleavage fracture form and the other is much finer. Inhomogeneity in size distribution is apparent for the sample milled 10 h, which indicates that the milling is mainly on the fracturing stage. For the 40 h sample, amount of finer particles increases substantially, with sign of agglomeration and welding simultaneously. However, occasional presence of the bulkier particle which was seen in the 10 h sample is also present in the 40 h milled sample. To interpret this information with the help of the XRD result, it implies that the larger particle appeared in both images is TiH_2 that has not involved in a reaction with either Mg or Ni. Bright field TEM and SAED images obtained are shown in Figure 3-13 (a) and Figure 3-13 (b). It was however difficult to tell the crystallite size from the bright field TEM micrograph due to heavy amorphization. Similarly in the SAED image (Figure 3-13 (b)), where the Debye–Scherrer rings appear to be extremely blurred, a convincing index could not be achieved for these nearly amorphous samples unfortunately.

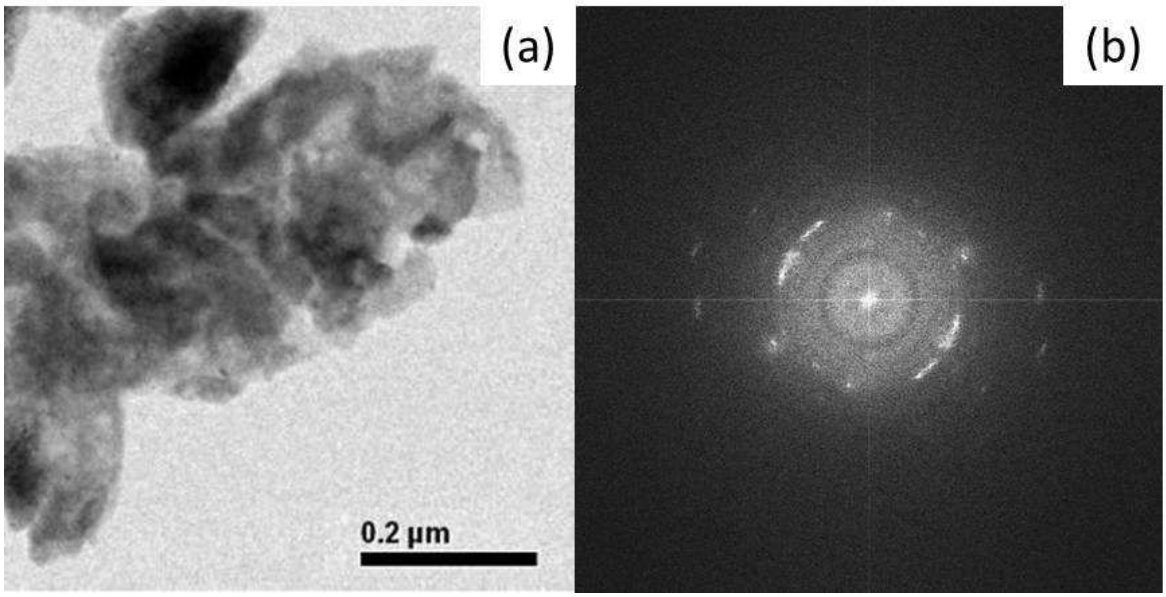

Figure 3-13 TEM micrographs for $(TiH_2)_{1.5}Mg_{0.5}Ni$ milled 40 h: (a) bright field TEM image (b) corresponding SAED pattern.

3.6 Hydrogen properties characterization of $(TiH_2)_{1.5}Mg_{0.5}Ni$

PCI curves at 298 and 473 K are shown in Figure 3-14 and Figure 3-15, respectively. Apparently, longer milling time increases hydrogen capacity, from approximately 0.07 H/f.u. to 0.45 H/f.u on average. For the sample milled 10 h, while showing a negligible amount of capacity, hydrogen content hardly changes with increase of pressure. Comparing the samples milled for different times, slopes of the curves are smaller for the sample milled longer, indicating a larger reversible hydrogen capacity. Plateau pressure is not observed for all samples, implying that the hydrogen storage here is in solid-solution. To examine the reversibility of hydrogen sorption, absorption curve is obtained for the sample milled 40 h. It can be seen that the adsorption and absorption curves are closely drawn on Fig. 3-14, which indicates that there is little hysteresis effect and that the hydrogen capacity happened is reversible in the solid-gas reaction with hydrogen. The absorption curve is drawn for the sample milled 40 h to examine hysteresis effect, which seems minor.

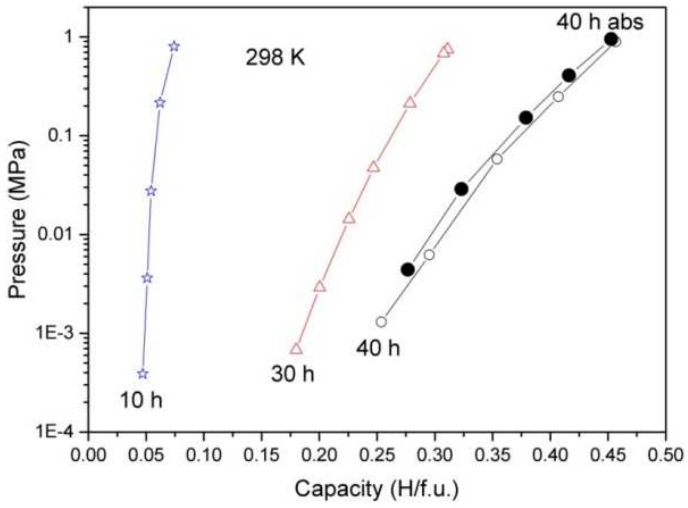

Figure 3-14 PCI curves for $(TiH_2)_{1.5}Mg_{0.5}Ni$ milled 10 h, 30 h, and 40 h at RT (298 K). Empty symbol and full symbol refer to desorption and absorption respectively. Both absorption and desorption capacity were measured only for the sample milled 40 h.

PCI curves tested at 473 K are shown in Figure 3-15. While the pattern is similar to the one at 298 K, the slopes of all samples are less steep, which means higher reversible hydrogen capacity is induced at higher temperature. Take the sample milled 40 h as example, hydrogen content change is about 0.2 H/f.u. at RT, while it is 0.3 H/f.u at 478 K under similar pressure variation. When comparing the Figure 3-14 and Figure 3-15, hydrogen content is found to be lower at higher temperature for all samples, which is evident that all hydrogen absorption occurs in solid solution.

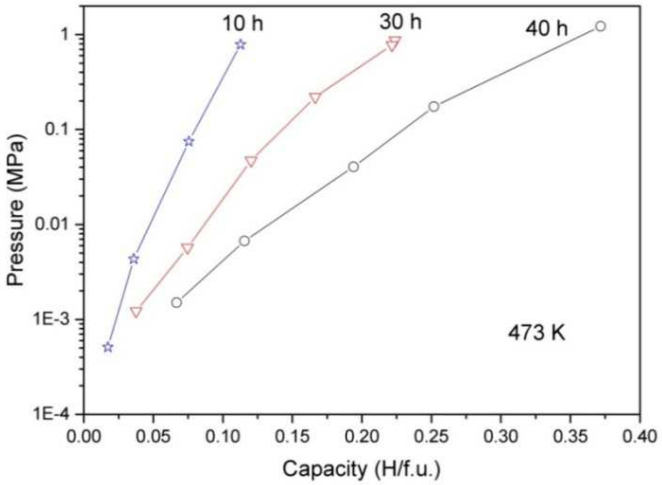

Figure 3-15 PCI desorption curves for $(TiH_2)_{1.5}Mg_{0.5}Ni$ milled 10 h, 30 h, and 40 h at 473 K.

Electrochemical cycling test under galvanostatic condition uses the milled sample as the negative electrode material. The discharge capacity against cycling number plot is shown in Figure 3-16. In general, discharge capacity increases with milling time and is consistent with the solid-gas reaction result presented in PCI curves. The characteristics of these curves can be simply summarized as: high capacity at starting cycle (no activation), fast capacity drop within a few cycles, and stable cycling performance afterwards. Except for the 10 h sample which hardly provides any capacity, discharge capacities of the

other samples all begin with their maximum value but decline drastically after around 5 cycles, and then they exhibit excellent cycling stability. The highest capacity is obtained by the sample milled 40 h at 100 mAh/g, as it suffers a drop of 30 mAh/g just in the second cycle. This behavior is quite comparable to the study of Rousselot et al. [87], where discharge capacity was highest during the first cycling but decrease continuously with cycling. The difference is however in the present study, discharge capacity can retain and stabilize a certain level of reversible capacity. They attributed the high initial capacity to the structural transition between HCP/BCC and FCC structure as they suggest FCC phase does not undergo a structural transition. In the present study, this behavior should be ascribed to the TiH_2 FCC phase which Mg is dissolved into (known as the Ti-Mg-H phase in the study of Rousselot et al. [87]). Particularly, the capacity drops more severely during the first few cycles for the sample milled for longer time (~45 mAh/g drop for 40 h milled sample milled compared to 10 mAh/g drop for 20 h milled sample) despite their higher initial capacity. Since the irreversible capacity is contributed by the Ti-Mg-H phase, it is tempting to attribute this phenomenon to the different amount of Ti-Mg-H phase in each sample. However, we can see in the XRD results that Ti-Mg-H has formed at the very early stage of the milling, except that the formation of TiNi is during and after 20 h of time mark. Therefore, it is inferred that it is the content of TiNi that has activated the discharge capacity of Ti-Mg-H, and played the role of gateway for the release of hydrogen from the Ti-Mg-H phase. This effect can be compared to the study of Cuevas et al. where TiH_2 was reported to improve hydrogen dissociation and diffusion through Mg phase [84]. For the Ti-Mg FCC phase with the lattice constant 4.22 Å, it has been suggested that it does not contribute discharge capacity at room temperature [36]. At last, the excellent cycling stability is credited to the cubic TiNi phase. Higher capacities exhibited by the sample milled longer time are credited to the larger amount of the TiNi

phase proved by the XRD results. The discharge electrochemical isotherm obtained by GITT shown in Figure 3-17 for the sample milled 30 h at RT agrees with the PCI curve as it does not exhibit a plateau potential either.

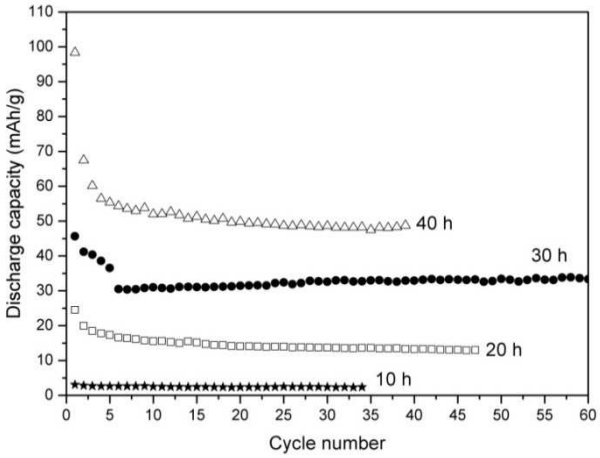

Figure 3-16 Discharge capacity against cycle number at C/5 regime and room temperature.

These hydrogenation characteristics of the milled $(TiH_2)_{1.5}Mg_{0.5}Ni$ evaluated by both PCI and electrochemical cycling are explained by two contributors of the hydrogen capacity: the TiH_2(Mg)/Ti-Mg-H phase and the cubic TiNi phase except the also existing Ti-Mg FCC phase. It shows that the Ti-Mg-H FCC owns a temporary H storage as its release of hydrogen is not reversible once Ti-Mg FCC is produced. However, in the current study the conversion proportion of Ti-Mg-H to Ti-Mg during milling is not known. Rietveld analysis may solve this issue in our future work. On the other hand, the cubic TiNi phase is credited to the reversible capacities, especially obvious after the cycling stabilize. Its solid-solution nature of hydrogenation behavior has been reported as characteristic for the austenitic type TiNi [42, 45, 90]. Additionally, as mechanical milling resulted in severe amorphization of the sample, the amorphous phase is also known for cycling stability and poor capacity. A comparative study of synthesizing methods shows that reversible

hydrogen intake occurs in solid solution when the sample is mechanically alloyed in amorphous phase, whereas the same sample synthesized by casting exhibits a plateau pressure [90].

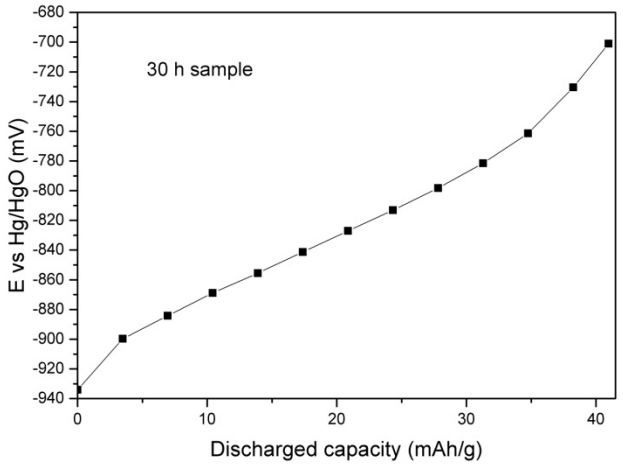

Figure 3-17 Discharge electrochemical isotherms for $(TiH_2)_{1.5}Mg_{0.5}Ni$ milled 30 h at RT

3.7 Summary

In this chapter, the milling of Ti(H), Mg and Ni reveals a major discovery of a favored Ti-Mg FCC structure under certain milling conditions. Although there were reports of other Ti-Mg structures, it shows that we obtained the Ti-Mg FCC with the identical lattice constant *a* ~4.22 Å under same milling parameters, especially the PCA use of ethanol, which may have played a critical role. DFT calculation confirmed that all Ti-Mg structures are thermodynamically unstable, we can only however explain that it is the alloying technique we applied MA being responsible for the production of the metastable phase. The mechanism of the relationship between the Ti-Mg FCC formation and certain milling conditions require further study. While the findings of the study of $(TiNi)_{1-x}Mg_x$ shows that this Ti-Mg structure is deteriorate to the hydrogen capacity of the milled samples, the study of $(TiH_2)_{1.5}Mg_{0.5}Ni$ explained

the issue as it shows the irreversibility of the Ti-Mg-H FCC phase, which shrinks its lattice constant *a* from ~4.45 Å to 4.22 Å upon dehydrogenation. In the same time, we find that nanocrystalline/amorphous phase enhances the activation process and cyclic stability of the sample.

Chapter 4 H-properties of $Ti_{2-x}Zr_xNi$ Synthesized by MA

In this chapter, Zr substitution for Ti in Ti_2Ni is studied as the element powder were milled with the formula of $Ti_{2-x}Zr_xNi$ (x = 0, 0.1, 0.2). It is intended to obtain an amorphous phase of $Ti_{2-x}Zr_xNi$, inspired by the work where amorphous Ti_2Ni was reported to improve cycling stability [51], and the work where it was reported Zr substitution for Ti increased discharge capacity in TiNi [5].

4.1 Microstructure of milled $Ti_{2-x}Zr_xNi$

Figure 4-1 shows the XRD patterns of Ti_2Ni as a function of milling time. Comparing the patterns with the ones obtained by ball milling Ti_2Ni [55], the prominent and broadened peak presented in all samples at ~ 42° corresponds to Ti_2Ni phase, which shows 20 h of milling has already yielded the amorphous/nanocrystalline Ti_2Ni while leaving element peaks in the meantime. After 40 h of milling, the main Ti_2Ni peak (42°) broadens even more while the intensity of element peaks decreases significantly, indicating further alloying progress. When milling time reaches 60 h, the peak centered at 42° becomes even smoother and element peaks disappear. This implies that the formation of amorphous Ti_2Ni has completed.

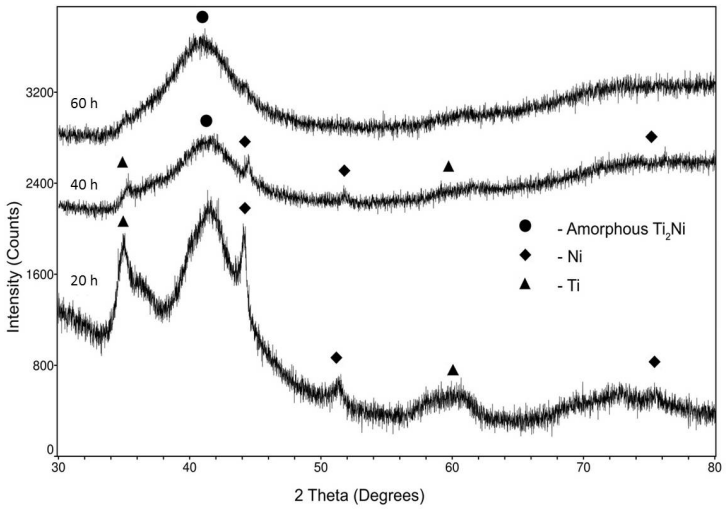

Figure 4-1 XRD patterns of mechanically alloyed Ti_2Ni for 20 h, 40 h, 60 h.

In comparison, the XRD patterns of $Ti_{2-x}Zr_xNi$ (x = 0, 0.1, 0.2) mechanically alloyed 60 h is presented in Figure 4-2. It is interesting to see that as Zr is introduced to the initial powders, the peaks are narrower. With further analysis, it is found that the pattern consists of two main phases. One is the BCC structured TiNi phase, which was reported to be formed during ball milling [91]. As shown in Figure 4-2, peaks that correspond to (Ti, Zr)Ni shift slightly left to the ordinary TiNi austenitic pattern (PDF card 18-0899). This is the sign of Zr substitution of Ti in the TiNi cubic structure, which caused the increase of lattice constant. That Zr substitution for Ti leads to cell-volume expansion was reported by Cuevas et al. [45]. The other major phase has an FCC structure with a lattice constant *a* ~4.35 Å. There was doubt that FCC was TiO who also has the same structure with a lattice constant *a* 0.429 Å, as later the EDX assisted TEM did find trace of oxidation, which is nonetheless too small to contribute a significant FCC phase seen in Figure 4-2. Moreover, the FCC structure has been previously studied by Bera et al. [92], who concluded that Zr can induce the HCP to FCC transformation of Ti. They excluded the possibility of TiO or other impurity for the cause of the FCC phase. It is particularly interesting to see that this phenomenon persists when Ni is present.

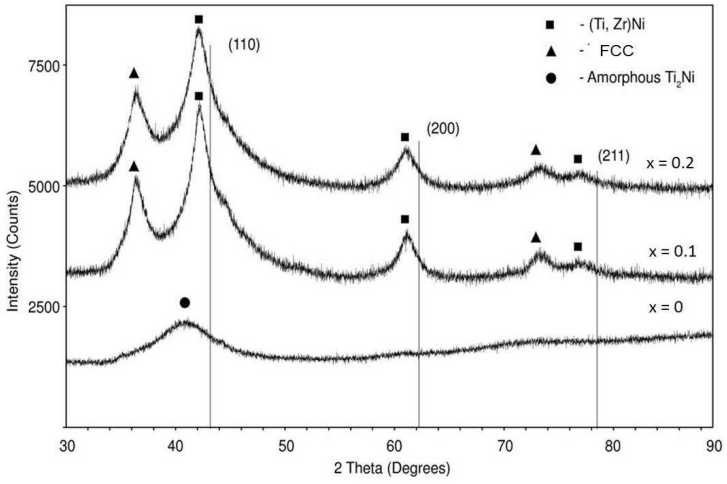

Figure 4-2 XRD Pattern of $Ti_{2-x}Zr_xNi$ (x = 0, 0.1, 0.2) with a fixed milling time 60h.

The result obtained by XRD characterization shows that Zr decreases the stability of amorphous Ti_2Ni. The mechanism of amorphization during mechanical milling is however of great complexity. There are two known models that seek to predict the possibility of formation of amorphous phase for two given elemental powders as shown in Table 4-1 [74].

Table 4-1 Comparison of the predicted and observed glass-forming ranges in mechanically alloyed Ti-Zr-Ni

System	Amorphous-phase-forming range		
	Miedema model	CALPHAD	Observed
Ti-Ni	23-76Ti		28-72Ti
Ni-Zr	22-63Zr	17-67Zr	24-85Zr

The possibility of forming amorphous phase for binary systems Ti-Ni and Ni-Zr is listed in Table 4-1. It can be seen that although the compositions of Ti-Ni in $Ti_{1.8}Zr_{0.2}Ni$ and $Ti_{1.9}Zr_{0.1}Ni$ are 60 Ti (at%) and 63 Ti (at%), which are in the range that the Table 4-1 indicates (in both Miedema and CALPHAD models), the ratios of Ni-Zr don't fit (as Zr at% is 9). Furthermore, it is confirmed experimentally that additional Zr decreases the stability of amorphous Ti_2Ni [55]. From using the XRD data, average crystallite sizes for samples with Zr were estimated at around 5 nm.

Figure 4-3 is the SEM micrographs of $Ti_{2-x}Zr_xNi$ that were milled 60 h. It can be seen that the morphologies changes greatly with increase of Zr content. All the samples in Figure 4-3 are milled 60 h, but as Zr has an effect of slowing down the amorphization process, the morphologies of (a), (b), (c) appear to be in the different stages of milling (chronologically backward). It is known that milling involves two major processes, namely cold welding and fracturing [74].

The dominating process between the two is largely decided by particle sizes. In Figure 4-3 (a), the amorphous phase looks like a result of cold welding, which indicates that very fine particles had been once obtained but were cold welded afterward. In comparison, samples milled equally 60h in Figure 4-3 (b) (c) (d) exhibit flaky and inhomogeneous in size distribution, which implies the outcome of fracturing. However, the obvious agglomeration still suggests the inclination of cold welding. To conclude, if milling were prolonged, fracturing would continue until finer crystalline is much more common, which is the prerequisite for amorphous phase. In other words, by comparing Figure 4-3 (a) and (b) (c) (d), Zr apparently decelerated the progress of amorphization. In Figure 4-3 (c) (d), where x = 0.2, large particles is found and size distribution is more inconsistent than when x = 0.1 as well. An EDX analysis was followed to quantify the chemical compositions in different zones. As shown in Table 4-2, large particle (zone 1 in Figure 4-4 as an example) contains generally more Zr than small ones (zone 2 in Figure 4-4 as an example). This is yet the other evidence that Zr is counterproductive for the refining process.

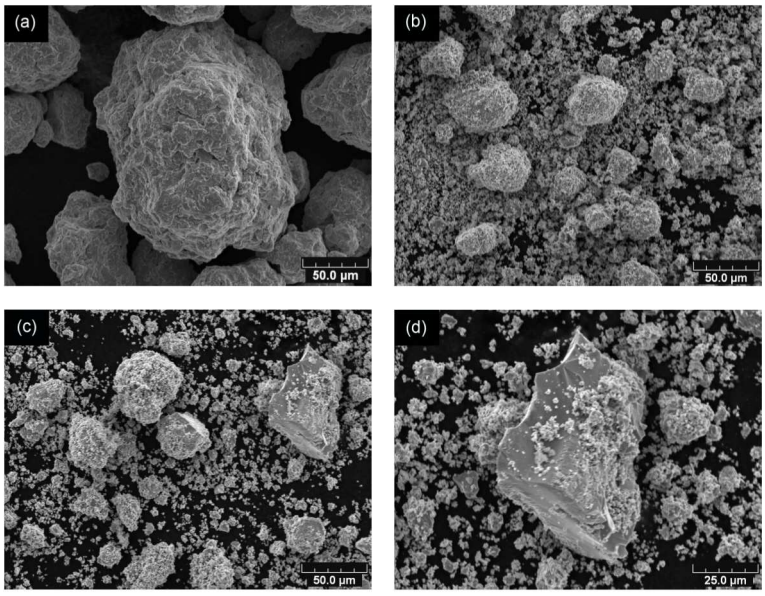

Figure 4-3 SEM micrographs of $Ti_{2-x}Zr_xNi$ milled 60h: (a) x = 0, (b) x = 0.1, (c) x = 0.2, × 500, and (d) x = 0.2, × 1000.

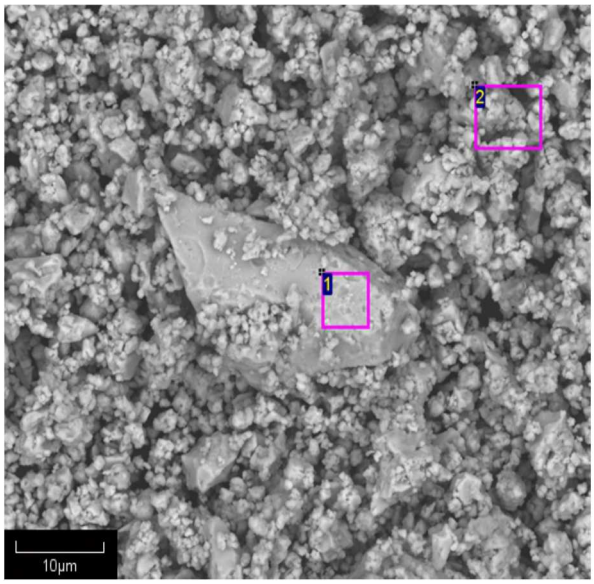

Figure 4-4 SEM with EDX analysis
focusing on different zones.

Table 4-2 Quantitative analysis on the element compositions of different zones

Spectrum	Content (at%)		
	Ti	Ni	Zr
Zone 1 (large particle)	61.07	33.37	5.56
Zone 2 (fine particles)	61.51	34.52	3.97

Figure 4-5 (a) illustrates the bright field TEM image of $Ti_{1.9}Zr_{0.1}Ni$ milled 60h and the corresponding selected area electron diffraction (SAED) pattern is shown in Figure 4-5 (b). From the bright field TEM image Figure 4-5 (a) combining the HRTEM image Figure 4-5 (c), it can be seen that crystallite size is in the range of 4-10 nm, which is in agreement with estimation using the XRD data (5 nm). The Debye-scherrer rings are indexed according to the interplanar distances. (200) with d = 1.538 Å and (110) with d = 2.170 Å reflections were found as originated from (Ti, Zr)Ni (space group *Pm3m*). By comparing them with the parameters of TiNi in space group *Pm3m*, an increase of d ((200) with d = 1.496 Å and (110) with d = 2.111 Å from PDF card 18-0899) is found again, which is ascribed to the increase of lattice constant a as the result of Zr

substitution for Ti. These results obtained from TEM investigation are consistent with the analysis by XRD.

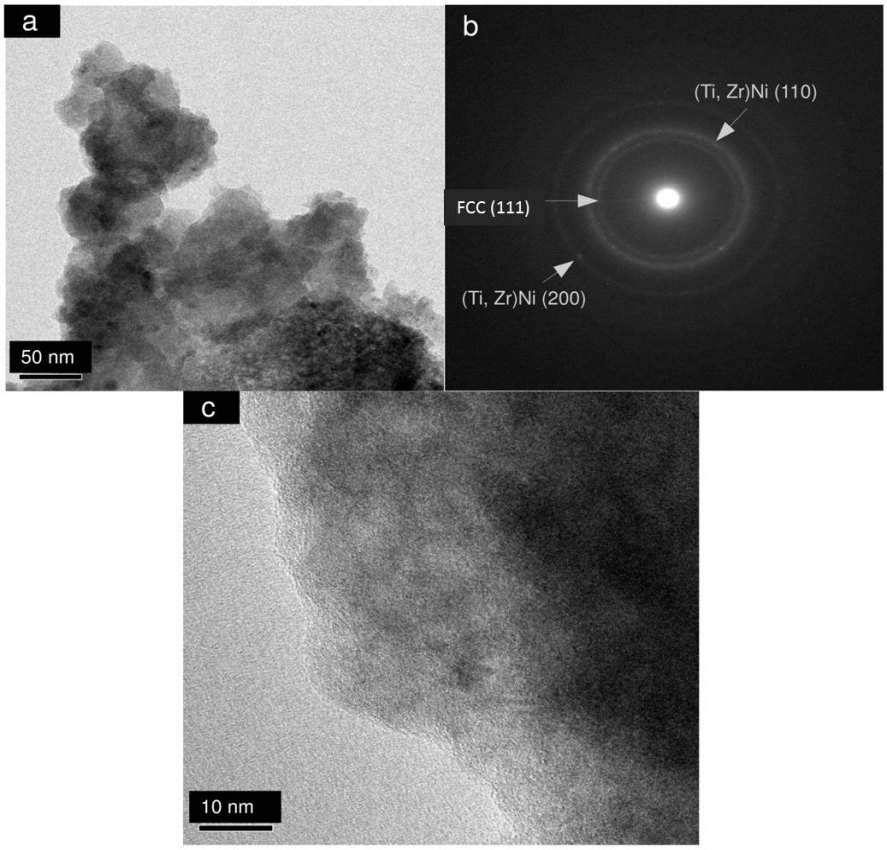

Figure 4-5 TEM micrographs of $Ti_{1.9}Zr_{0.1}Ni$: (a) bright field TEM image, (b) corresponding SAED pattern, and (c) HRTEM image.

4.2 DFT calculation on the cubic Ti-Zr-Ni structures

First principle calculations were done on the obtained BCC and FCC structures of Ti-Zr-Ni structures, which mainly include the austenitic TiNi with Zr substitution (Ti(Ni, Zr)), Ti FCC structure, and the Ti-Zr FCC structure. This is reminiscent of the Ti-Mg FCC studied in the previous chapter.

The parameters used in this calculation can be referred to 3.2.1 in the chapter 3. The calculated structures are displayed in Figure 4-6. The lattice

constant used in the calculation and the value after geometry optimization are listed in Table 4-3.

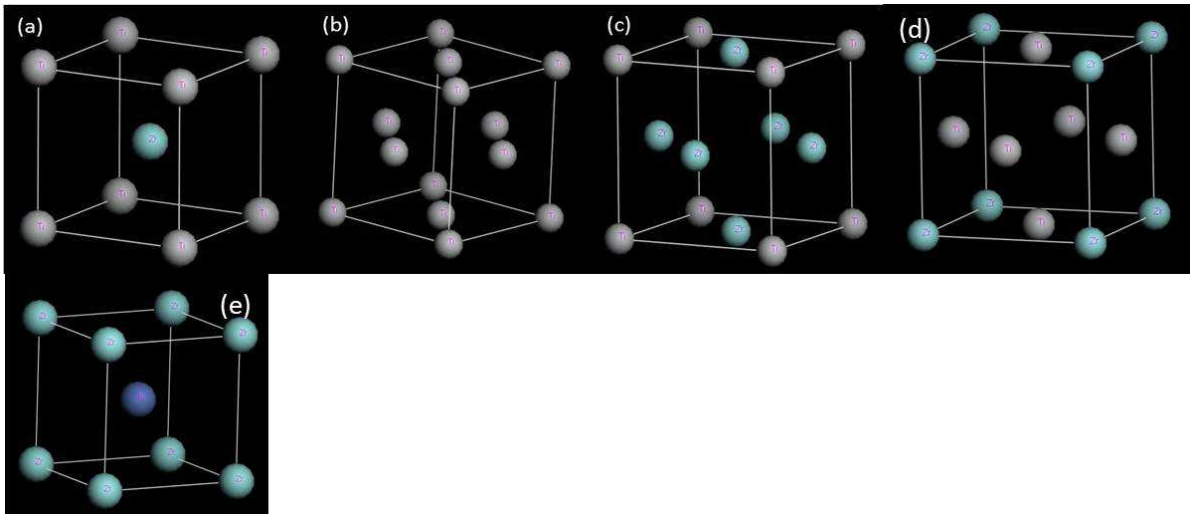

Figure 4-6 Structures calculated with DFT: (a)Ti-Zr BCC, (b)Ti FCC, (c)$TiZr_3$ FCC, (d)Ti_3Zr FCC, (e) ZrNi BCC.

	Initial lattice constant (Å)	Calculated lattice constant (Å)	Enthalpy of formation per atom (eV/atom)
TiZr BCC	a = 3.2	a = 3.421	0.201
Ti FCC	a = 4.2	a = 4.117	0.192
$TiZr_3$ FCC	a = 4.46 [90]	a = 4.429	0.058
Ti_3Zr FCC	a = 4.21 (XRD result)	a = 4.225	0.079
ZrNi BCC	a = 3.015	a = 3.213	-0.398

Table 4-3 Lattice constant of calculated structures and their enthalpy of formation per atom

The initial lattice constant for TiZr BCC is based on the TiNi BCC structure that has the value a = 3.015. It can be seen that its lattice constant is indeed increased compared to TiNi BCC. Nonetheless, its relatively high enthalpy of formation indicates the structure is rather unstable. On the other hand, ZrNi BCC has a negative enthalpy of formation, which implies that substitution of Zr for Ti in TiNi is theoretically applicable, as it also increases the lattice constant of the TiNi cubic structure. For Ti FCC, the initial lattice

constant is based on previous studies, in which 4.42 Å [92] and 4.11 Å [93] were reported. For Ti FCC, our calculation of the lattice constant is identical with the calculation by the other group [93]. For Ti-Zr FCC, the calculated value 4.429 Å is between the reports of Bera et al. (4.459 Å) [92] and our result (4.35 Å). This can be explained by the difference in Ti:Zr ratio, as in our work Ti is considerably more than in the work of Bera et al. The more the content of Ti, the smaller the lattice constant is. Finally, by comparing the enthalpy of formation per atom, it is found that the Ti-Zr FCC structure has obviously a lower value, which has made it a favorable structure among the three. This explains well why Zr induces the transformation of Ti to the FCC structure. A more profound study using Gibbs free energy calculation shows that, Ti phase transformation is both size and temperature induced. Ti FCC is a small size stable phase, while its BCC and HCP structures are high-temperature and low-temperature stable, respectively [95]. It can be inferred that this Ti-Zr FCC is the product of the Zr solution into the Ti FCC lattice.

4.3 Electrochemical capacity on cycling

Figure 4-7 shows the discharge capacities for Ti_2Ni mechanical alloyed by ball milling 20 h, 40 h, and 60 h respectively as a function of cycle number (at current density of 40 mA/g). Two characteristics can be concluded from the curve. First, the discharge capacities apparently increase with milling time. This seems to contradict to Zhao et al.'s result [55], in which longer milling time decreases the discharge capacities of the alloy. However, the difference is in that they ball milled the Ti_2Ni synthesized by solid-state sintering, while our samples were alloyed by ball milling from elemental powders. Longer milling time means more content of alloy produced. In Figure 4-1, Ti and Ni peaks are discernible for both (a) (milled 20 h) and (b) (milled 40 h). This denotes incomplete alloying. However, 40 h milled sample obtained more alloy since its

element peaks are vague and weaker than the ones milled 20 h. Second, the mechanical alloyed Ti_2Ni exhibits prominent cycling stability and excellent activation properties. The samples milled 20 h and 60 h hardly need activation to attain their stable discharge capacities except for the sample milled 40 h, which was activated immediately after the first cycle. In other words, the mechanical alloyed Ti_2Ni exhibits outstanding electrochemical activation. The result is consistent with the one from Zhao et al. [55], in which the amorphous Ti_2Ni showed favorable easy activation and steady cycling stability. The advantage of amorphous Ti_2Ni is ascribed to greater surface area provided by ball milling. However, it should be noted that the maximum discharge capacities are not as high as the Ti_2Ni alloyed by the as-sintered sample (278 mAh/g in the first cycle) [9], which unfortunately has the problem of severe capacities loss during cycling. These evidences suggest that the capacity loss of Ti_2Ni is not caused by the formation of irreversible $Ti_2NiH_{0.5}$ as Luan et al. [96] concluded. The good electrochemical kinetic but lower initial capacity are attributed to the structure of amorphous Ti_2Ni that provides efficient paths for the transportation of hydrogen, while it is in lack of storage sites for hydrogen compared with as-sintered Ti_2Ni.

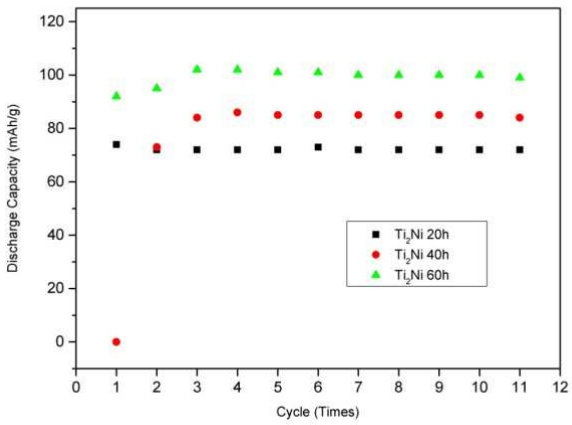

Figure 4-7 Cycling stabilities of Ti_2Ni alloy milled 20 h, 40h , and 60h.

Table 4-4 Cycling stabilities for $Ti_{2-x}Zr_xNi$ with different milling time and content of Zr

Milling time (h)	20	40	60		
C_{max} (mAh/g)	74	86	102	39	39
Retaining rate (R_{11})	97.3%	97.7%	97.1%	87.2%	100%
Standard deviation (mAh/g)	0.6	25.5	3.1	3.2	2.7
Content of Zr	x = 0	x = 0.1			x = 0.2

Figure 4-8 compares the cycling discharge capacities of $Ti_{2-x}Zr_xNi$ (x = 0, 0.1, 0.2) with a fixed milling time of 60 h. Substantial decrease in discharge capacities occurred when Zr is added to the binary Ti-Ni system, but the cycling stability remains in good shape. As shown in Table 4-4, the retaining rate for $Ti_{1.8}Zr_{0.2}Ni$ reaches as high as 100%, and the small standard deviation figure suggests considerable steady discharge capacity in the cycling test (capacity retaining rate calculated as introduced in Ref. [97]. $R_h = C_n/C_{max} \times 100\%$). It should be noted that despite decrease of capacity as Zr is introduced, when x increases from 0.1 to 0.2, the discharge capacity increases again in general. From the XRD pattern in Figure 4-2, it can be seen that austenitic TiNi is the only phase that serves as the hydrogen carrier. Moreover, it is reported that $Ti_{50-x}Zr_xNi_{50}$ has merely a maximum discharge capacity of 85 mAh/g at a discharging rate of C/10 (8.5 mA/g), but it does not suffer capacity loss in cycling [44]. Therefore, the steady performance in cycling for TiNi is expected. The introduction of Zr has caused substantial capacity drops even for the sample $Ti_{1.9}Zr_{0.1}Ni$. Secondly, the capacity difference between Zr = 0.1 and Zr = 0.2 is minor and should be ignored on account of experimental inaccuracies. This result should be largely explained by the structural change Zr has raised rather than the amount of Zr content to be the cause of the capacity loss, which is the

formation of the FCC phase instead of Ti_2Ni amorphous phase. The capacity exhibited from the sample with Zr substitution is credited to the TiNi austenite phase. The FCC phase which is mainly Ti FCC and partly Ti-Zr is unfavorable to either hydrogenation or dehydrogenation. As studied in the previous chapter, it showed that the Ti-Mg-H FCC phase was easily formed during milling, it however has the difficulty to absorb hydrogen during electrochemical cycling. As for the case of Ti (Zr) FCC, further research is required to reveal the obstacle to the electrochemical cycling performance.

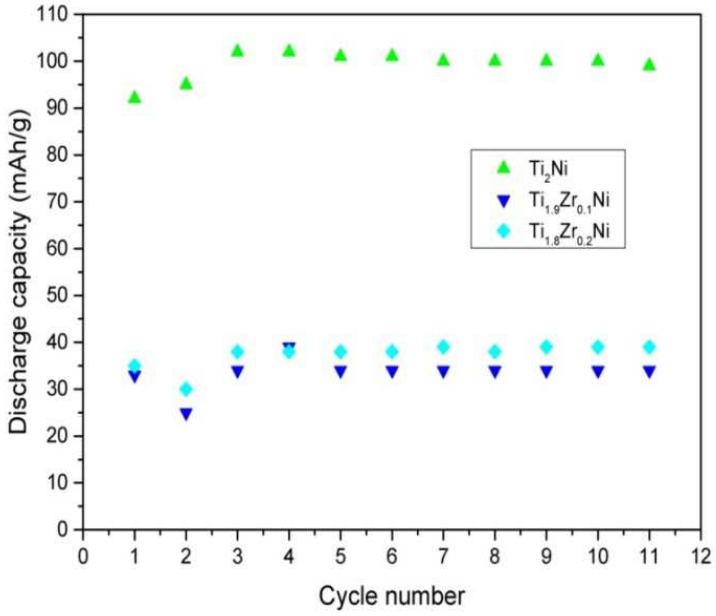

Figure 4-8 Cycling stabilities of $Ti_{2-x}Zr_xNi$ (x = 0, 0.1, 0.2) milled 60 h.

In summary, all samples for $Ti_{2-x}Zr_xNi$ exhibit outstanding cycling stability. The stability for Ti_2Ni is ascribed to the amorphous phase obtained by mechanical alloying. As for $Ti_{2-x}Zr_xNi$ (x = 0.1, 0.2), the electrochemical properties is in fact a reflection of the austenitic TiNi phase, which is characteristic of stable cycling performance and mediocre discharge capacity.

4.4 Summary

In this chapter, we intended to study the substitution effect of Zr for Ti in highly amorphous Ti_2Ni. Amorphous Ti_2Ni was realized by 60 h of ball milling from pure elemental powders. With Zr substitution, the threshold of amorphization for Ti_2Ni increases as the sample with Zr exhibit a crystalline trend, with average grain size of 4 - 5 nm. The products were mainly cubic TiNi and the Ti (Zr) FCC phase when Zr is present. DFT calculation shows a considerable enthalpy (of formation per atom) decrease when Zr is dissolved in the Ti FCC lattice. Both amorphous Ti_2Ni and (Ti, Zr)Ni exhibit appealing stable cycling performances. The amorphous Ti_2Ni by ball milling 60 h reached a maximum discharge capacity of 102 mAh/g at a current density of 40 mA/g under room temperature. The discharge capacity during the electrochemical cycling is believed to be contributed by the TiNi phase. Formation of the FCC phase induced by Zr deteriorates electrochemical performance measured at RT.

Chapter 5 Concluding Remarks and Outlook

In this thesis work, we have applied mechanical alloying as the synthesis technique on the alloying of Ti-Ni system. With partial element substitution/doping to the system, the potential of the alloyed sample to be used as the negative electrode materials in Ni-MH batteries is examined. Specifically, in chapter 3, we studied the Mg influence on the mechanically alloyed TiNi system, and in chapter 4, effect of Zr substitution for Ti in Ti_2Ni was investigated. The experimental study is also aided and complemented by first principle calculation, which further demonstrates the structural results of the experiment. Important findings and conclusions by this research are summarized as the followings:

- It is shown that Ti-Ni alloy can be achieved via mechanical alloying. In the present work, where similar milling parameters were applied, the final product of milling Ti and Ni element powders is essentially the cubic TiNi phase (CsCl type), which is also called the austenitic type of TiNi. This result is unrelated to the initial atomic ratio of Ti and Ni, as we have found prevalent cubic TiNi phase in both products of milled $(TiH_2)_{1.5}Mg_{0.5}Ni$ and milled $Ti_{2-x}Zr_xNi$. With prolonged milling, the TiNi phase develops to a much refined nanocrystalline with the grain size averaged at 5-10 nm, and eventually amorphous, which presents a distinct broadened peak at 42° (2theta) in their XRD patterns.

- The hydrogenation properties of TiNi show that the cubic TiNi stores hydrogen in solid solution, which exhibit mediocre discharge capacity but extreme stable cyclic performance under room temperature. The highest discharge capacity is reached for Ti50-Ni50 milled 20 h at 135 mAh/g (discharge current density 40 mA/h). Discharge capacity decreases for longer milled samples, due to amorphization of the sample.

- It is found that high energy ball milling induces re-crystallization, which

happens at around 20 h of milling under present milling condition. After 20 h of milling, the alloying of the element may have completed, while prolonged milling only produces nanocrystalline phase or amorphous phase of the existing alloys. This is especially observed for the milling of Ti50-Ni50. In the case of the milling of Ti_2Ni, the least milled sample was milled 20 h, the element peaks observed in XRD patterns can already be a product of re-crystallization. To solve this ambiguous possibility, one can reduce the milling time to less than 20 h and investigate the phase change with milling time.

- Both Zr and Mg doping/substitution hinder the process of amorphization of TiNi. It can be seen that all samples with element doping substitution present widened but pointy peaks in their XRD patterns. Especially for Zr, after 60 h of milling the phase composition of $Ti_{1.9}Zr_{0.1}Ni$ is more crystalline like than amorphous, while the 60 h milled Ti_2Ni is present in amorphous phase.

- Both Mg and Zr were found to induce the formation of the Ti-based FCC phase, which has a lattice constant a ~4.22 Å and 4.21 Å respectively. DFT calculation shows that the Ti-Zr FCC structure has a positive yet extremely low enthalpy of formation per atom compared to the FCC Ti structure. It is however especially interesting to find that Ti-Mg alloying is favored to the alloying of Ti-Ni in our milling, since Ti and Mg are immiscible according to their binary phase diagram. Comparison of enthalpy of formation per atom does not give much of an advantage for alloying priority to the Ti-Mg FCC structure (against TiNi) either. By comparing the milling products of Ti-Mg with other research groups [59, 62, 63], it is inferred that the formation of the FCC structure is closely related to the choice of PCA (ethanol) or milling media (steel ball).

- It is found that Mg can dissolve into the TiH_2 phase extremely fast and form

a Ti-Mg-H FCC structure which has a lattice constant *a* (4.44 Å) slightly larger than the Ti-Mg FCC phase. The hydrogenation properties shows that Ti-Mg-H can release hydrogen in both low hydrogen pressure condition or discharging time during electrochemical cycling with the help of TiNi gateway function, but it is not able to absorb hydrogen once it is released at room temperature. This has caused major capacity loss when Mg is added on the milling of Ti and Ni, where Ti-Mg FCC takes the priority to form over TiNi.

- According to the DFT calculation, both MgNi and ZrNi with the BCC structures are relatively stable phases, however Ti-Mg or Ti-Zr BCC are not likely to be obtained due to their high positive enthalpy of formation.

In the meantime, there are several issues that are particularly interesting to the current study, which can be further investigated:

- It is worthy to find out the milling conditions or mechanisms of the production of the Ti-Mg BCC phase. Once Ti-Mg BCC can be obtained, its hydrogen properties should be studied.

- The hydrogenation properties for Ti-Mg-H should be further studied, as it is found that the dehydrogenation of Ti-Mg-H can be achieved with a gateway mechanism (TiNi as an example) under room temperature, the hydrogenation for the Ti-Mg FCC is the culprit which damage its cycling performance under RT.

- DFT calculations demonstrated that Ti-Zr FCC is a relatively stable phase. In chapter 4, it was found the sample with Zr substitution did not perform well in electrochemical cycling. However it only proved that the majority phase Ti FCC could not provide hydrogen capacity. As a matter of fact, when the content of Zr increase from x = 0.1 to x = 0.2, a minor increase of discharge

capacity was observed. This improvement had to be ignored due to consideration of measurement inaccuracy. However, the hydrogen properties of the Ti-Zr FCC phase should be further studied.

- We have found that Mg and Ti both hinder the amorphization process of TiNi, and promote the Ti-based FCC phase. It is not known yet if other foreign elements would play the same role in the formation of the FCC phase. Since the Ti-based FCC phase is not favored to hydrogen storage, an element that hinders the formation of the FCC phase is especially a target to find.

References

References

[1] Sakintuna, B.; Lamaridarkrim, F.; Hirscher, M. Int. J. Hydrogen Energy 2007, 32, 1121.

[2] Huang, H.; Li, G.; Zhuang, S. J. Braz. Chem. Soc. 2013, 24, 1339.

[3] Burch, R.; Mason, N. J. Less Common Met. 1979, 63, 57.

[4] Gutjahr, M.A.; Buchner, H.; Beccu, K.D.; Säufferer, H. Power Sources 1973,4,79.

[5] Szajek, a.; Makowiecka, M.; Jankowska, E.; Jurczyk, M. J. Alloys Compd. 2005, 403, 323.

[6] Wang, C.; Lei, Y.; Wang, Q. J. Power Sources 1998, 70, 222.

[7] Deying, S.; Xueping, G.; Yunshi, Z. J. Alloys Compd. 1993, 199, 161.

[8] Buchner H, Gutjahr MA, Beccu KD, Saufferer H. Z Metalkunde. 1972, 63, 497.

[9] Zhao, X.; Ma, L.; Yao, Y.; Ding, Y.; Shen, X. Energy Environ. Sci. 2010, 3, 1316.

[10] Luan, B.; Cui, N.; Zhao, H.; Zhong, S.; Liu, H. K. K.; Dou, S. X. X. J. Alloys Compd. 1996, 233, 225.

[11] Luan, B.; Cui, N.; Zhao, H. J.; Liu, H. K.; Dou, S. X. Int. J. Hydrogen Energy 1996, 21, 373.

[12] Li, X. D.; Elkedim, O.; Nowak, M.; Jurczyk, M.; Chassagnon, R. Int. J. Hydrogen Energy 2013, 38, 12126.

[13] Anani, A.; Visintin, A.; Petrov, K.; Srinivasan, S.; Reilly, J. J.; Johnson, J. R.; Schwarz, R. B.; Desch, P. B. J. Power Sources 1994, 47, 261.

[14] Zaluski, L.; Zaluska, A.; Ström-Olsen, J. J. Alloys Compd. 1997, 254, 70.

[15] Zhao, X.; Ma, L. Int. J. Hydrogen Energy 2009, 34, 4788.

[16] Hamilton, C. W.; Baker, R. T.; Staubitz, A.; Manners, I. Chem. Soc. Rev. 2009, 38, 279.

[17] Silambarasan, D.; Vasu, V.; Iyakutti, K.; Surya, V. J.; Ravindran, T. R. Phys. E Low-dimensional Syst. Nanostructures 2014, 60, 75.

[18] Dixit, M.; Maark, T. A.; Pal, S. Int. J. Hydrogen Energy 2011, 36, 10816.

[19] Huang, L. W.; Elkedim, O.; Moutarlier, V. J. Alloys Compd. 2010, 504, S311.

[20] Tousignant, M.; Huot, J. J. Alloys Compd. 2014, 595, 22.

[21] Kircher, O.; Fichtner, M. J. Alloys Compd. 2005, 404-406, 339.

[22] Schlapbach, L.; Zuttel, A. Nature 2001, 414, 353.

[23] Lee, G.-J.; Shim, J.-H.; Whan Cho, Y.; Sub Lee, K. Int. J. Hydrogen Energy 2007, 32, 1911.

[24] Hsu, W.-C.; Yang, C.-H.; Tan, C.-Y.; Tsai, W.-T. J. Alloys Compd. 2014, 599, 164.

[25] Reshak, a. H. Int. J. Hydrogen Energy 2013, 38, 11946.

[26] Tsuchiya, T.; Yasuda, N.; Sasaki, S.; Okinaka, N.; Akiyama, T. Int. J. Hydrogen Energy 2013, 38, 6681.

[27] Kleperis, J.; Wójcik, G.; Czerwinski, A.; Skowronski, J.; Kopczyk, M.; Beltowska-Brzezinska, M. J. Solid State Electrochem. 2001, 5, 229.

[28] Aguey-Zinsou, K.-F.; Ares-Fernández, J.-R. Energy & Environmental Science, 2010, 3, 526.

[29] Mintz M.; Zeiri, Y. J. Alloys Compd. 1995, 216, 159.

[30] Barkhordarian, G.; Klassen, T.; Bormann, R. Journal of Alloys and Compounds 2006, 407, 249.

[31] Otsuka, K.; Kakeshita, T. MRS Bulletin, 2002, 27, 91–100.

[32] Hara, T.; Ohba, T.; Otsuka, K.; Nishida, M. Mater. Trans. JIM 1997, 38, 277.

[33] Reilly, JJ.; Metal Hydride Technology. Brookhaven National Lab., Upton, NY (USA); 1979.

[34] Szajek, a.; Makowiecka, M.; Jankowska, E.; Jurczyk, M. J. Alloys Compd. 2005, 403, 323.

[35] Cuevas, F.; Latroche, M.; Ochin, P. J. Alloys Compd. 2003, 357, 730.

[36] Li, X. D.; Elkedim, O.; Nowak, M.; Jurczyk, M. Int. J. Hydrogen Energy

2014, 39, 9735.

[37] Schmidt, R.; Schlereth, M.; Wipf, H.; Assmus, W.; Mullner, M. Journal of Physics: Condensed Matter. 1999, 1, 2473.

[38] Otsuka, K.; Ren, X. Prog. Mater. Sci. 2005, 50, 511.

[39] Burch, R.; Mason, N. B. J. Chem. Soc, Faraday Trans. 1. 1979, 75, 578.

[40] Soubeyroux, J. L.; Fruchart, D.; Lorthioir, G.; Ochin, P.; Colin, D. J. Alloys Compd. 1993, 196, 127.

[41] Gutjahr, MA.; Buchner, H.; KD, Beccu.; H, Säufferer. J Power Sources 1973, 4, 79.

[42] Emami, H.; Souques, R.; Crivello, J.-C.; Cuevas, F. J. Solid State Chem. 2013, 198, 475.

[43] Drenchev, B.; Spassov, T. J. Alloys Compd. 2009, 474, 527.

[44] Cuevas, F.; Latroche, M.; Ochin, P. J. Alloys Compd. 2002, 332, 250.

[45] Cuevas, F.; Latroche, M.; Percheron-Guégan, A. J. Alloys. Compd. 2005, 404-406, 545.

[46] Guiose, B.; Cuevas, F.; Décamps, B.; Leroy, E.; Percheron-Guégan, A. Electrochim. Acta 2009, 54, 2781

[47] Guiose, B.; Cuevas, F. Int. J. Hydrogen Energy 2008, 33, 5795.

[48] Buchner, H.; Gutjahr, MA.; Beccu, KD.; Saufferer, H. Z Metalkunde 1972, 63, 497.

[49] Luan, B.; Cui, N.; Zhao, H.; Liu, HK.; Dou, SX. J. Power sources. 1995, 55(1), 101.

[50] Zhao, X.; Ma, L.; Qu, X.; Ding, Y.; Shen, X. Energy & Fuels 2009, 23, 4678.

[51] Zhao, X.; Ma, L.; Ding, Y.; Shen, X. Trans Nonferrous Met. Soc. China 2011,21,512.

[52] Takeshita, H. T.; Tanaka, H.; Kiyobayashi, T.; Takeichi, N.; Kuriyama, N. J. of Alloys and Compds. 2002, 330-332, 517.

[53] Zhao, X.; Zhou, J.; Shen, X.; Yang, M.; Ma, L. Int. J. Hydrogen Energy

2012, 37, 5050.

[54] Hu, W.; Wang, J.; Wang, L.; Wu, Y.; Wang, L. Electrochim. Acta 2009, 54, 2770.

[55] Hsieh, S. F.; Wu, S. K. J. Alloys Compd. 1998, 266, 276.

[56] Zhao, X.; Zhou, J.; Shen, X.; Yang, M.; Ma, L. Int. J. Hydrogen Energy 2012, 37, 5050.

[57] Huang, L. W.; Elkedim, O.; Nowak, M.; Chassagnon, R.; Jurczyk, M. Int. J. Hydrogen Energy 2012, 37, 14248.

[58] Kalisvaart, W. P.; Wondergem, H. J.; Bakker, F.; Notten, P. H. L. J. Mater. Res. 2011, 22, 1640.

[59] Kalisvaart, W. P.; Notten, P. H. L. J. Mater. Res. 2011, 23, 2179.

[60] Vermeulen, P.; Graat, P.; Wondergem, H.; Notten, P. Int. J. Hydrogen Energy 2008, 33, 5646.

[61] Asano, K.; Enoki, H.; Akiba, E. J. Alloys Compd. 2009, 478, 117.

[62] Asano, K.; Enoki, H.; Akiba, E. J. Alloys Compd. 2009, 480, 558.

[63] Rousselot, S.; Bichat, M.; Guay, D.; Roué, L. ECS Trans. 2009, 16, 91.

[64] Rousselot, S.; Gazeau, A.; Guay, D.; Roué, L. Electrochim. Acta 2010, 55, 611.

[65] Rousselot, S.; Guay, D.; Roué, L. J. Power Sources 2011, 196, 1561.

[66] Drenchev, B.; Spassov, T. J. Alloys Compd. 2007, 441, 197.

[67] Yavari, A. R.; Desre, P. J. Mater. Sci. Eng. A. 1991, 134, 1315.

[68] Froes, FH.; Suryanarayana, C.; Russell, K.; Ward-Close, CM. Singh J, Copley SM, editors. 1994, 1.

[69] Song, M. Y.; Ivanov, E. I.; Darriet, B.; Pezat, M.; Hagenmuller, P. International Journal of Hydrogen Energy 1985, 10, 169.

[70] Zaluski, L.; Zaluska, A.; Ström-Olsen, J. J. Alloys Compd. 1995, 217, 245.

[71] Wang, J.-Y. Int. J. Hydrogen Energy 2009, 34, 3771.

[72] Nouri, A.; Wen, C. Crit. Rev. Solid State Mater. Sci. 2014, 39, 81.

[73] C. Suryanarayana, Prog. Mater. Sci. 46 (2001).

[74] ETH Zürich. The Electron Microscopy Site. http://www.microscopy.ethz.ch/bragg.htm

[75] Egerton, R. F. Physical principles of electron microscopy: An introduction to TEM, SEM, and AEM; Springer US, 2005; pp. 1–202.

[76] Broom, D. P. Hydrogen Storage Materials: The Characterisation of Their Storage Properties; Springer Science & Business Media, 2011.

[77] Clark, SJ.; Segall, MD.; Pickard, CJ.; Hasnip, PJ.; Probert, MJ.; Refson, K. et al.. Z Kristallogr 2005, 220, 567.

[78] Denys, R. V.; Zavaliy, I. Y.; Berezovets, V. V.; Paul-Boncour, V.; Pecharsky, V. K. Intermetallics 2013, 32, 167.

[79] Williamson G, Hall W. Acta Met 1953, 1, 22-31.

[80] Perdew, JP.; Burke, K. Ernzerhof M. Phys Rev Lett. 1996, 77, 3865.

[81] Vanderbilt, D. Phys Rev B. 1990, 41, 7892.

[82] Van, Setten, MJ.; de, Wijs, GA.; Brocks, G. Phys Rev B. 2007, 76, 075125.

[83] Yavari, AR.; Desre, PJ. Mater Sci Eng A. 1991, 134, 1315.

[84] Cuevas, F.; Korablov, D.; Latroche, M. Phys. Chem. Chem. Phys. 2012, 14, 1200.

[85] Tao, S. X.; Notten, P. H. L.; van Santen, R. a.; Jansen, A. P. J. J. Alloys Compd. 2011, 509, 210.

[86] Asano, K.; Akiba, E. J. Alloys Compd. 2009, 481, L8.

[87] Rousselot, S.; Guay, D.; Roué, L. J. Power Sources 2010, 195, 4370.

[88] Emami, H.; Cuevas, F.; Latroche, M. J. Power Sources 2014, 265, 182.

[89] Asano, K.; Kim, H.; Sakaki, K.; Page, K.; Hayashi, S.; Nakamura, Y.; Akiba, Etsuo. J. Alloys Compd. 2014,593,132.

[90] Cuevas, F.; Villeroy, B.; Leroy, E.; Olier, P.; Latroche, M. J. Alloys Compd. 2007, 446-447, 218.

[91] Tria, S.; Elkedim, O.; Hamzaoui, R.; Guo, X.; Bernard, F.; Millot, N.;

Rapaud, O. Powder Technol. 2011, 210, 181.

[92] Bera, S.; Manna, I. J. Alloys Compd. 2006, 417, 104.

[93] Van Heerden, D.; Josell, D.; Shechtman, D. Acta materialia 1996, 44, 297.

[94] Aguayo, A.; Murrieta, G.; de Coss, R. Phys. Rev. B 2002, 65, 092106.

[95] Xiong, S.; Qi, W.; Huang, B.; Wang, M.; Li, Y.; Li, Z.; Liang, S. EPL (Europhysics Letters) 2011, 93, 66002.

[96] Luan, B.; Cui, N.; Zhao, H.; Liu, H.; Dou, S. J. Power Sources 1995, 55, 101.

[97] Zhang, Y.; Ren, H.; Li, B.; Guo, S.; Pang, Z.; Wang, X. Int J Hydrogen Energy 2009, 34, 8144.

Appendix

Appendix 1 :

Methods of Preparing Hydrogen Storage Materials

Appendix 2:

Publications and Conferences

Appendix 1 Methods of Preparing Hydrogen Storage Materials

Methods of preparing Hydrogen Storage Materials

Introduction

The method for preparing hydrogen storage materials evolves with the development of alloying techniques. It also varies according to the type of hydrogen storage material. There are several hydrogen storage systems up to date, such as metallic compounds[1], complex hydrides [2], nano materials (nanotube [3], nanofibers [4], nanoparticles [5], nanohorns [6]), metal organic frameworks [7], calthrate hydrides [8], molecular sieve [9] and so on. They however share common goals of hydrogen storage materials: (I) cost efficient, (ii) high volumemetric and gravimetric density of hydrogen, (iii) fast kinetics and appropriate thermodynamic properties, (iv) long-term cycling stability and high degree of reversibility. These properties have been significantly improved through chemistry modifications and conventional thermal, mechanical processing methods. Nonetheless, current found materials cannot offer all demand properties. For example, the theoretical hydrogen storage of $LiBH_4$ is 18 wt.%, but the high temperature of decomposition limits its application. $LaNi_5$ as a hydrogen storage material has excellent thermodynamic properties and fast kinetic, and is easy to activate. Although it decomposes fast at room temperature, but its hydrogen storage capacity is only 1.4 wt%, and is not cost efficient. Besides the ongoing exploration of new ideal materials for hydrogen storage, researchers have also been exploiting different ways to improve properties of known materials that have the potential.

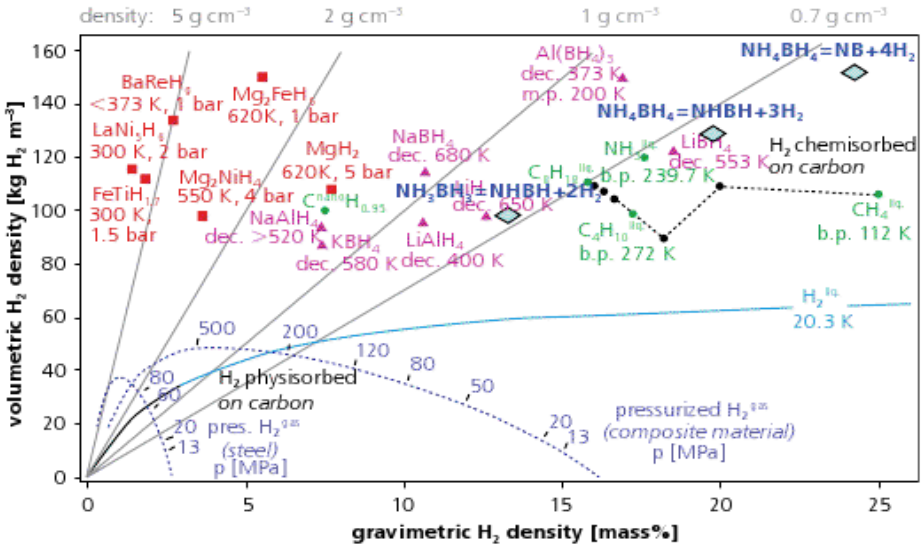

Figure 1 Comparison of gravimetric and volumetric densities of various hydrogen storage materials

In this chapter, we will introduce and discuss some of the most used methods for the preparation of hydrogen storage materials: 1). melting 2). mechanical milling 3). chemical synthetic method 4). combustion synthesis 5). plasma synthesis 6). vapor deposition 7). spark plasma sintering.

Hydrogen storage materials preparation methods

Alloying method: Melting

Melting is the most common and traditional method used on metallic compound system. Arc melting [10], induction melting [11], melt spinning [11] have all been applied on the preparation of hydrogen storage alloys.

Arc melting (Figure 2 [11]) and induction melting are actually conventional alloying methods. They were used often on early researches and preparations for hydrogen storage materials.

Normally, arc melting is carried out in an electric arc furnace that heats charged material by means of an electric arc. It differs from induction melting in that the charge material is directly exposed to an electric arc, and the current in

the furnace terminals passes through the charged material. In induction melting process, the heat is applied by induction heating (Figure 2.) of melting. The advantage of this technique is that the process is cleaner and easier to control compared to most other means of metal melting.

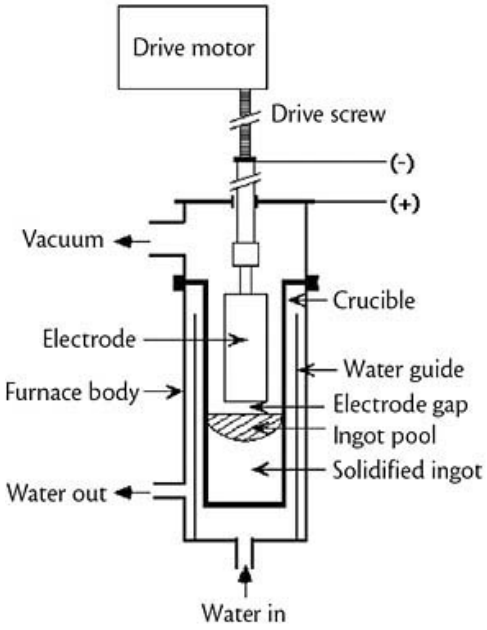

Figure 2 An arc melting furnace

Itoh et al. [12] compared on the micro-structure influence on the hydrogen absorption properties of the Ti-Cr-V and Ti-Cr-V-Fe prepared by arc melting and induction melting. They found that melting methods and thermal history affected the hydrogen absorption properties of Ti-Cr-V system BCC alloy greatly. For the alloy prepared by arc-melting, the micro-structure and lattice constant were extremely different between the surface side and the crucible side, which lead distinct resulting PCT characteristic. For the alloy prepared by VIM (Vacuum Induction Melting), the micro-structure and lattice constant were only slightly different, and consequently the PCT characteristic is not as discernable as for the alloy prepared by arc melting. In addition, they pointed out that heat treatment after melting process at high temperature could improve homogeneity,

and fast cooling rate during casting make the structure fine grained while an enlarged lattice constant.

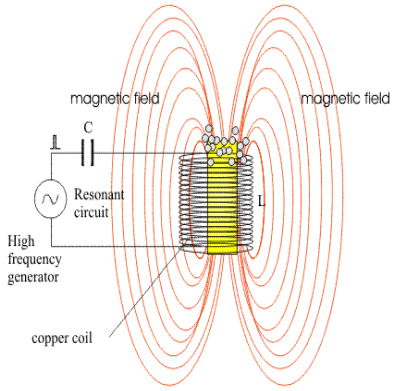

Figure 3 Induction heating

Melt spinning is a relatively novel post melting technique that has drawn more and more attentions nowadays. In melt spinning, liquids were “poured” on a rotating wheel that is cooled internally by water or liquid nitrogen, and a thin stream of liquid drips onto the wheel. This cooling process makes rapid solidification. The cooling rates is so high (104-107 kelvins per second [13]) that it can form metallic glasses (non-equilibrium phases), or polymer.

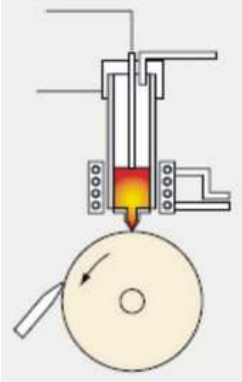

Figure 4 Melt spin scheme

Mg_3LaH_9 is a Mg-base hydride that has a theoretical hydrogen storage capacity of 4.1 wt. %. Several experiments were conducted with $Mg_3RENi_{0.1}$

alloys by induction melting method. The dehydrogenation temperature was lowered by 20 K [14][15], and hydrogen absorption/desorption rate was faster [16]. Tanaka [17] produced a Mg-Ni-La nanocrystalline alloy transforming from the amorphous phase demonstrated a reversible hydrogen storage capacity of 4.6 wt. % at 240 ºC. And Wu. et al. reported that the melt-spun version of Mg-10Ni-2Mm alloy offers higher hydrogen storage capacity (4.2 wt. %) than the ball-milled one (3.2 wt. %), and also has a superior absorption rate [18]. Lin et al. [19] recently prepared $Mg_3LaNi_{0.1}$ by a single roller melt-spun method. Samples of $Mg_3LaNi_{0.1}$ were firstly melted by a line-frequency induction melting method with the starting powders of Mg (99.9% purity), La (99.9%) and Ni (99.9) purity). The ingots were then broken into smaller sizes for subsequent melting spinning. Before the molten alloy was injected to proceed for melting spinning, they were re-melted completely by an intermediate frequency induction heating. The copper wheel rotated at a linear velocity of 23.55 m/s (1500 rpm). The distance between the nozzle and the wheel remained ~2 mm. The melt-spun ribbons were treated by an aging treatment under argon atmosphere for 14 days at room temperature. Microstructure characterization shows that the melt-spun $Mg_3LaNi_{0.1}$ alloy was composed of Mg_3La phase, and fine $LaMg_2Ni$ grains were precipitated after an aging treatment at room temperature. The melt-spun alloy shows excellent hydrogen absorption kinetics and lowered desorption temperature compared with the induction-melted alloy. Maximum hydrogen storage capacity reached 3.1 wt. % and hydrogen desorption was possible at 224 ºC. The improvement was attributed to the catalytic role of *in-situ* formed nanocrystalline Mg_2Ni and LaH_2.

As already been used in commercialized Ni-MH batteries, $LaNi_5$ is one of the most popular metallic complex type materials for hydrogen storage, its variations have been extensively researched by different groups [20-24]. The drawback of $LaNi_5$-based compounds is that its hydrogen capacity is only 1.4 wt%

at moderate temperature. The parent compound absorbs 1.5H atoms per 1 $LaNi_5$. Different approaches have been tried to increase its capacity, including element substitutions [25], novel preparation methods [26], or surface treatment [27].

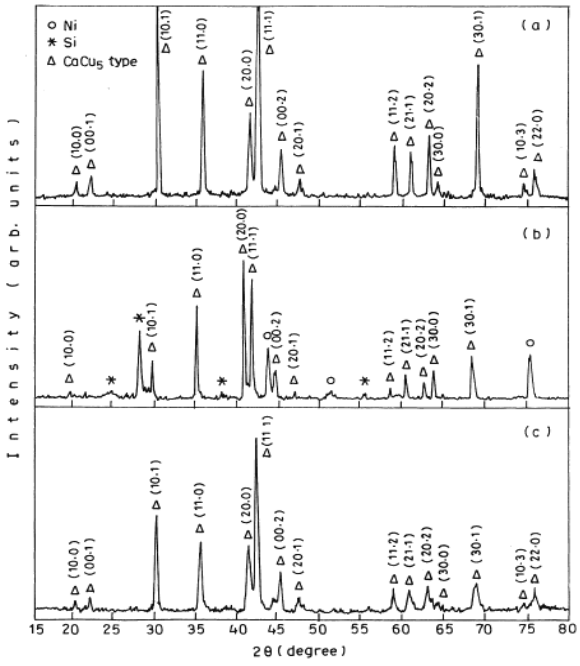

Figure 5 XRD patterns of $LaNi_{4.7}Si_{0.3}$ (a) bulk, (b) melt-spun versions, (c) after hydrogenation

Srivastava et al. [11] conducted a research on the synthesis, characterization and hydrogenation behavior of both the spin- and thermal-melted versions of $LaNi_{5-x}Si_x$ compound. La, Ni, Si was mixed in stoichiometric ratio, palletized and then melted in an induction furnace in argon ambient. They melted the pellets three times for homogeneity. The ingots formed were then subjected to rapid solidification by pouring them on a copper wheel, rotating at a speed of ~5000 rpm, which leads to cooling rates of 10^2 to 10^3 KS^{-1}. (The ribbons produced are ~8 in length, ~4 in width and ~1/10 mms in thickness.) For comparisons reasons, the identical samples were also synthesized through a normal induction melting. They found that special growth occurred in the direction perpendicular to the c-axis for melt-spun $LaNi_{4.7}Si_{0.3}$, and resulted in

improved kinetics and faster activation. In the melt-spun version, the hk0-type peaks have higher intensities which can be seen in the XRD pattern shown in Figure 5. This suggests that preferential grain growth has taken place in a direction perpendicular to the c-axis. The structural difference leads to different hydrogenation properties, which are illustrated in Figure 6. On the left, PCI curves at 300 K shows the bulk version of the sample provide slightly higher capacity. While on the right, the melt-spun version $LaNi_{4.7}Si_{0.3}$ has 60% faster kinetics than its bulk form.

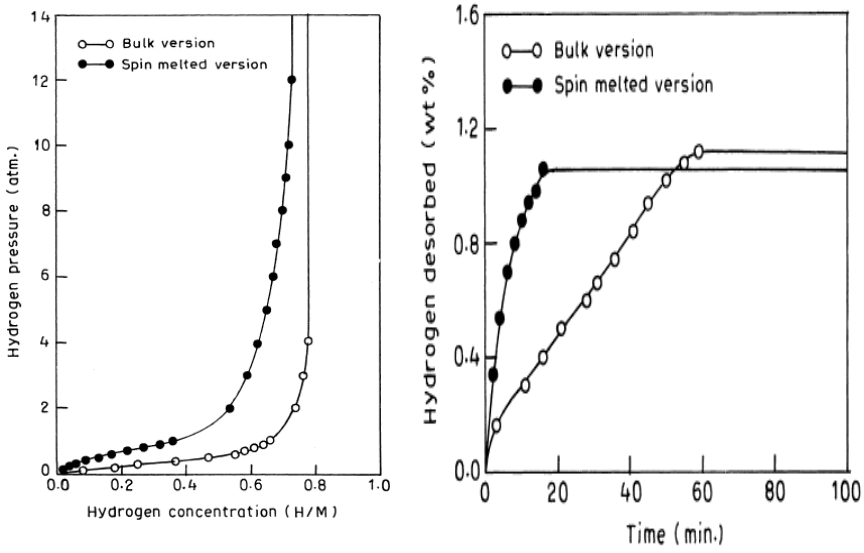

Figure 6 Hydrogenation properties of the melt-spun version and bulk version of $LaNi_{4.7}Si_{0.3}$. On the left are the PCI curves at 300 K. On the right are the kinetics curves.

Mechanical Milling

Mechanical milling is a mechanical alloying method, which was originally used to reduce particle size and to produce nanocrystallines. Today, it has also been extensively applied to obtain both equilibrium and non-equilibrium phases in materials fabrication or for properties improvement.

The process of MM is simple: stoichiometric powders are mixed and loaded into the mill with grinding medium. After a period of desired milling

time, the powder reaches a steady state. Optionally, the milled powder can then be heat treated if desired. A schematic milling platform is displayed in Figure 7.

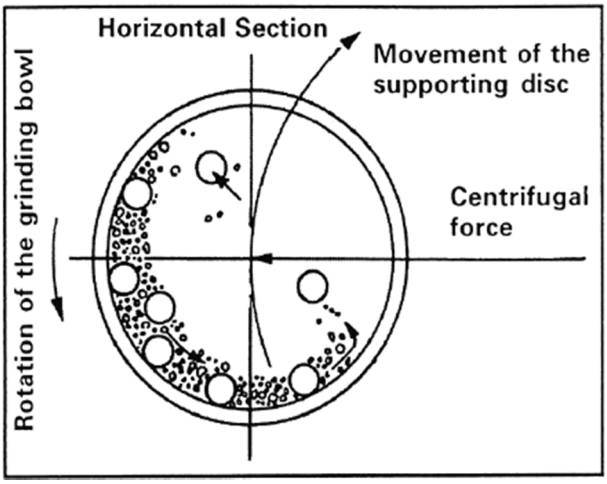

Figure 7 Schematic depicting the ball motion inside the ball mill.

The key parameters that influence the result of ball milling include milling time, milling speed, ball-to-powder (B/P) weight ratio [28]. Generally speaking, the longer the milling time, the higher the milling speed, and the higher the ball-to-powder weight ratio, the higher the energy would be put into the powder. Also, other variables like type of mill, milling container, grinding medium, extent of filling the vial, milling atmosphere, process control agents (PAC), and temperature of milling can also play a critical role in deciding the milling products [28].

Besides the economic advantage, mechanical milling can also overcome the phase diagram obstacle when alloy normally immiscible elements. It has been employed to produce a variety of compounds, including Mg–based [29], $LaNi_5$ based [30], and many other metallic compounds [31][32].

Zaluski et al. [29] first investigate the hydrogen storage absorption properties of Mg_2Ni prepared by mechanical alloying. They found that Mg_2Ni in nanocrystalline state obtained by ball milling shows superior hydrogen absorption characteristics to that of the conventional crystal phase, and the

activation is also much easier because of very active powder surface created in the ball milling process. Many researches then followed the work of Zaluski groups with Mg_2Ni as a potential hydrogen storage material [33-35].

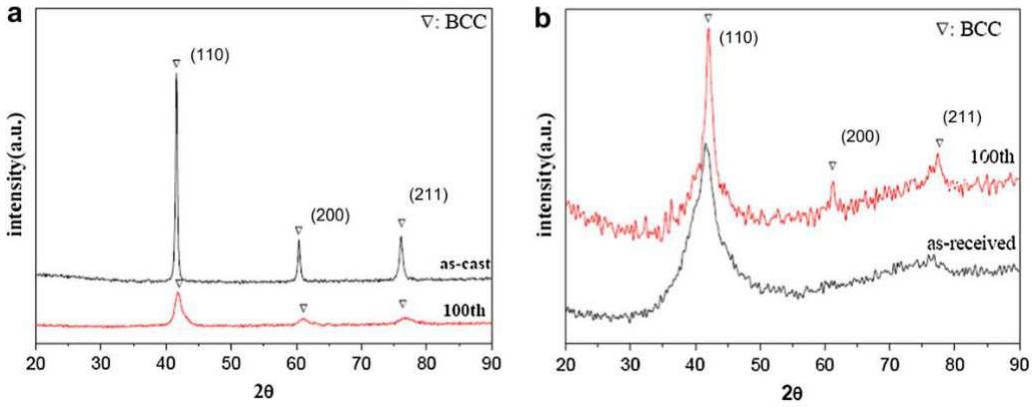

Figure 8 The XRD pattern of $Ti_{0.37}V_{0.38}Mn_{0.25}$ Prepared by arc melting (a) and mechanical alloying (b) after hydrogen absorption-desorption for 100 times.

Jian-Yih Wang [36] compared the hydrogen storage properties of $Ti_{0.37}V_{0.38}Mn_{0.25}$ prepared by mechanical alloying and vacuum arc melting. He found that the alloy prepared by vacuum arc melting has a single phase BCC crystal structure, and the maximum hydrogen absorption is 3.62 wt%, compared to samples prepared by mechanical alloy which has an amorphous crystal structure, with a maximum hydrogen absorption of 1.76%. However, although the hydrogen storage powders prepared by mechanically alloyed samples show better cyclic performance, the total hydrogen-absorption capacity of vacuum arc samples remained higher than that of the mechanically alloyed samples. The explanation for the mechanism is given by the XRD patterns from the two powders. It indicates that the mechanical alloyed powders prepared samples (amorphous phase) did not become as severely pulverized as the arc-melt prepared samples after many absorption-adsorption cycles.

A complex hydrides $NaNH_2$-$NaBH_4$ was synthesized via ball milling by Wu et al. [37] They used $NaBH_4$ and $NaNH_2$ as the starting materials with the molar ratio of 2:1. The diameter of the ball for milling is 8 mm, and the ball to

powder ratio is 20:1. The rotate speed is set to 300 rpm. The planetary mill stops for 12 minutes every 1 hour of milling. The milling time are 1, 2, 4, 8, 16, 32 hours. To prevent oxidation, the whole process (excluding ball milling) is conducted in a glove box filled with high purity argon. The compositions and hydrogen generation characteristics are investigated by XRD and thermo gravimetric-differential thermal analysis (TG-DTA).

From analysis of XRD patterns, a new phase of $Na_3(NH_2)_2BH_4$ is found to be produced by ball milling and mechanical energy accumulated in the ball milling process. There are two thermal decomposition stages of the composite $NaBH_4$-$NaNH_2$: below 400 ºC, hydrogen is released with Na_3BN_2 as by-product, and the amount of hydrogen release reaches 6.85 wt%; above 400 ºC, the previous by-product Na_3BN_2 continues to decompose to produce metal Na gradually. The first stage indicates that the composite $NaNH_2$-$NaBH_4$ can be a good candidate of hydrogen storage material.

Doi et al. [31] recently synthesized lithium silicon by mechanical alloying method. According to their study of this Li-Si-H system, this alloy can reversibly store 5.4 wt.% hydrogen with smaller reaction enthalpy than metal Li.

Combustion synthesis

Combustion synthesis is a relatively new synthesis method. As a highly exothermic reaction, the temperature can reach 3000 K. This synthesis method permits to synthesize a wide variety of advanced materials, including intermetallics solid solutions and metal-matrix composites. The materials produced by this method often demonstrate unique mechanical properties, physical properties and chemical properties.

Although combustion is generally under the environment of oxygen, the solid-state combustion reaction without oxygen has drawn much attention as a

new popular approach for producing advanced materials. Combustion synthesis in solid-state is often a self-propagating process. Once one end of the sample is ignited, the heat it generates sustains the reaction to continue and finally complete the final product. Compared to other synthesis method, combustion synthesis is economic, fast and effective.

For producing hydrogen storage materials, the process is also called hydriding combustion synthesis. It was first researched and published in the literature by Akiyama et al. [38]. They successfully synthesized Mg_2NiH_4 using this method. In their study, a powder of magnesium and nickel was mixed and compacted to a cylindrical shape under the various conditions of powder size, mixing method and loading pressure. The compact obtained was heated under an atmospheric pressure of nitrogen (0.1 MPa). The other compact obtained was then heated at 2.0 MPa hydrogen (800 K) to see whether it can form Mg_2NiH_4 directly. From XRD observation, they found the compact under hydrogen pressure showed a strong peak of Mg_2NiH_4 without Mg_2Ni peak. They concluded that it was possible to synthesize magnesium nickel hydride Mg_2NiH_4 directly from the compact of magnesium and nickel mixture at pressurized hydrogen, and also that combustion synthesis is both energy and time efficient for preparing hydrogen storage alloy compared to conventional method [38].

TiFe alloy as a hydrogen storage material was also successfully synthesized using the combustion method [39]. In the experiment, two-layered raw materials Ti powders was put in the upper layer as heat source, and a mixture of Fe and Ti in the molar ratio of 1:1 was put in the lower layer. The system is called self-ignition combustion synthesis (SICS). The schematic diagram is show in Figure 9. [39]

The device heated the sample to 1500 °C. under high pressure hydrogen up to 1.0 MPa and reached homogeneity.

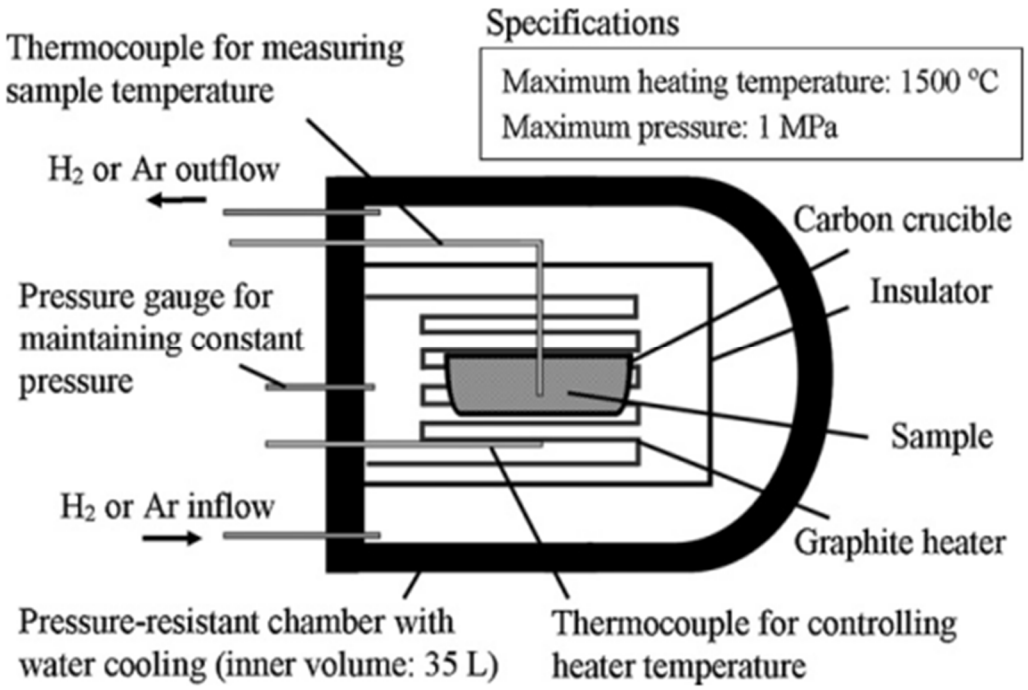

Figure 9 Schematic diagram of SICS reactor.

XRD results show that the reactions take place in the following order:

1). $Ti+H_2=TiH_2+144kJ$ (reversible)

2). $Ti+Fe=TiFe+40kJ$

3). $TiFe+0.03H_2=TiFeH_{0.06}$ - 0.69kJ

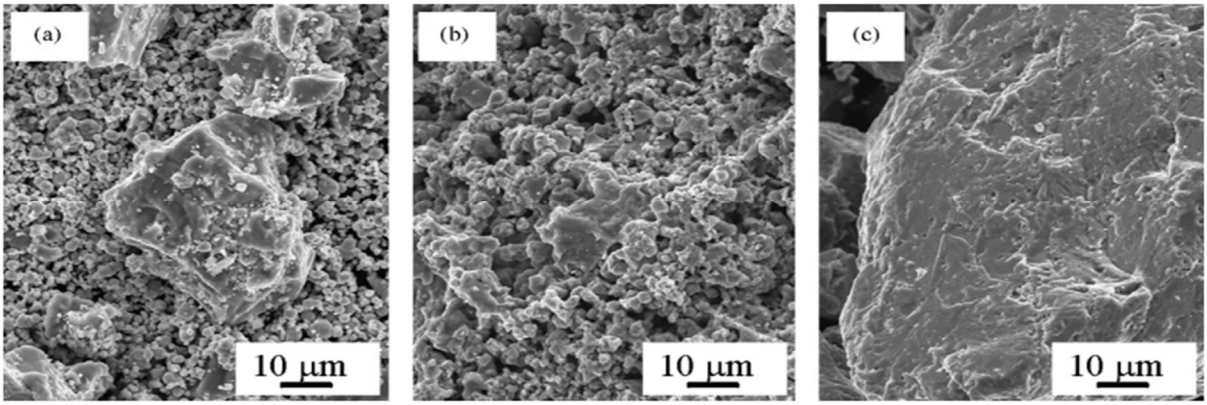

Figure 10 SEM images of (a) raw material, (b) TiFe synthesized by SICS, and (c) commercially available TiFe.

They reported that during SICS, the ignition takes place at a temperature lower than the melting point, and because of the formation of eutectic composition (partially liquid phase) of Ti and Fe, the reaction rate was drastically accelerated. Furthermore, the product obtained by SICS can be easily pulverized and has sufficiently high reaction rate [39]. The cycling performance was however not discussed in the article.

Later, Yasuda et al. [40] synthesized $TiFe_{1-x}Mn_x$ using SICS. All alloyed sample including TiFe without Mn doping absorbed hydrogen at 298 K smoothly at an initial pressure of 4.1 MPa.

Zhu et al. [41] did a study of Mg-La-Ni prepared by hydriding combustion synthesis (HCS) and mechanical milling. In their first paper of this study [42], they reported that the Mg_2NiH_4 prepared by HCS could be destabilized by MM, leading to a sharp decrease in the decomposition temperature that changed from 560 to 370 K. They considered that this improvement was credited to the process of MM and the unique structure features of HCS. In the later study of this ternary alloy [42], Mg-La-Ni, Mg, La_2Mg_{17} and Ni powders at the weight ratio of 11:6:3 were synthesized by combustion synthesis (CS) or hydriding combustion synthesis (HCS). Then samples of each composite was treated by mechanical milling (MM). SEM and hydriding/dehydriding measurements of samples prepared by four different methods of CS, CS+MM, HCS and HCS+MM with XRD were compared. Results show that sample prepared by HCS+MM exhibited the best hydrogen storage properties both in capacity and hydriding/dehydriding kinetics. For the HCS+MM product, LaH_3 and Mg_2Ni phases were homogeneously distributed on the surface of the Mg phase, and some of the Mg_2Ni phase showed laminar structures. The enhancement of the hydriding/dehydriding properties was explained as the result of favorable micro structure and the co-catalysis effect of the LaH_3 and Mg_2Ni phases.

Chemical synthetic method

Chemical synthetic method is a method to prepare certain types of hydrogen storage materials, such as MOF (Metal Organic Framework), Mg based alloy.

MOF is a new direction for hydrogen storage materials. They usually have low density, high surface area and very large porous volume. Various types of MOF with nanometer scale periodicity are being researched. These types of materials are synthesized by chemical method.

As an example, Li et al. [43] synthesized a MOF-5 type micro-porous material with a high surface area and large pore volume. The raw materials were $Zn(NO_3)_2 \cdot 6H_2O$, 1,4-benzenedicarboxylic acid (H_2BDC), N,N-dimethylformamide, and TEA. These synthesis compared different approaches.

1) Direct mixing of TEA.

$Zn(NO_3)_2 \cdot 6H_2O$ and H_2BDC were first dissolved in DMF with mild stirring, then TEA was added to the solution under agitation. The whole system was sealed and stirred at room temperature for 2h. The white products were collected by centrifugation, washed with DMF and dried at 373 K for 3-4 h.

2). Slow diffusion of TEA

The synthesis solution that contains $Zn(NO_3)_2 \cdot 6H_2O$, H_2BDC and DMF was placed in a large beaker, while TEA was placed in a smaller beaker, which was placed in the center of the larger beaker. The system was sealed with film and kept static for two days at room temperature. The white products were collected by centrifugation and washed with DMF. Finally, they were dried at 373 K for 3–4 h.

3). Solvothermal synthesis

$Zn(NO_3)_2 \cdot 6H_2O$, H_2BDC were dissolved in DMF. The solution was then transferred into a Teflon-lined autoclave, which was heated at 373 K for 24 h afterward. The reaction products were cooled to room temperature, and the solids were collected by centrifugation, washed with DMF, and dried at room temperature.

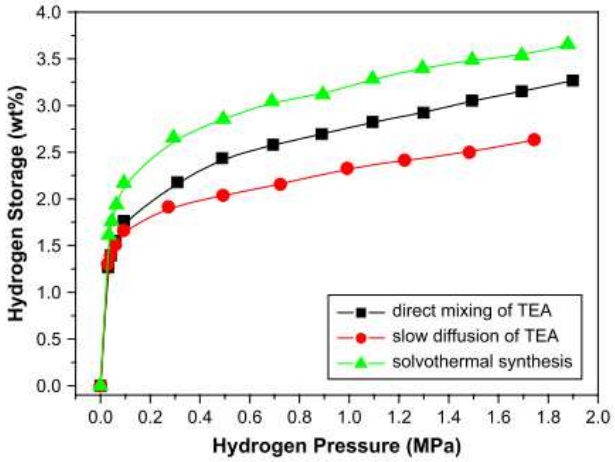

Figure 11 Hydrogen desorption isotherms at 77 K of the MOF-5 samples synthesized by the three different methods.

Figure 11 shows the hydrogen-storage capacities of MOF-5 samples synthesized by the three different methods. The samples of all MOF-5 exhibit high hydrogen-storage capacities: 2.63 wt% for MOF-5 produced by the slow-diffusion method, 3.20 wt% for the direct-mixing method, and 3.60 wt% for the solvothemal method at 1.74 MPa and 77K. Characterization analysis indicates that the surface area and pore volume of MOF-5 materials are correlated with their hydrogen-storage capacities.

Hydrogen Plasma Metal Reaction

HPMR (Hydrogen Plasma Metal Reaction) can be a solution for the synthesis of nano particles of various metals, alloys, hydrides, nitrides and carbides. The concept of this method is hydrogen plasma arc melting, which was first developed by Uda and his coworkers [44-46]. The scheme is shown in Figure 12.

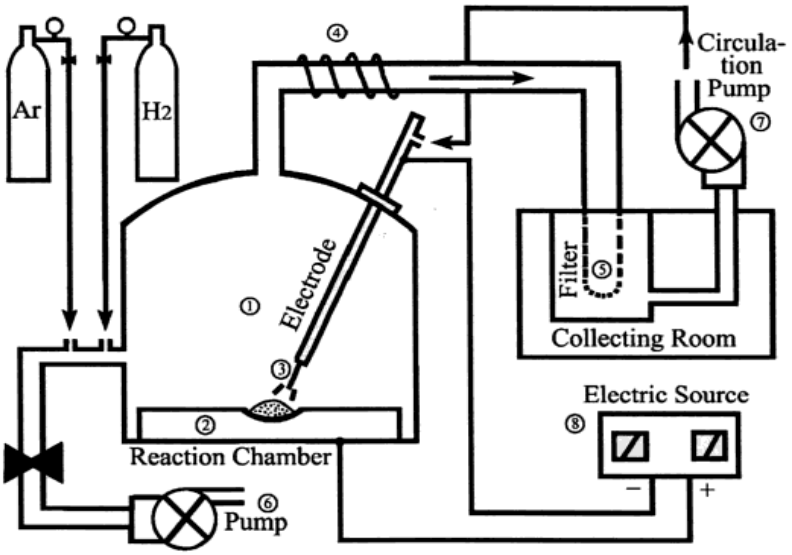

Figure 12 Schematic diagram of the equipment for synthesis of nanoparticles by HPMR; (1) arc melting chamber, (2) water-cooled copper hearth, (3) tungsten electrode, (4) heat exchanger, (5) particle collector, (6) vacuum pump, (7) gas circulation pump and (8) DC source.

In HPMR, the sample was melted and nano particles were yielded when the arc plasma was generated in a current from 100 to 300 A. For developing nano particles, the parent alloy bulks should be melted many times in advance to insure homogeneity. Nano particles were then prepared by HPMR with the pre-alloyed bulks in Ar atmosphere mixed with H_2. They alloy melted rapidly when struck by arc. With intense production of smoke begins, nano particles were emitted as vapors. A gas flow carries these particles out, which were then trapped on a membrane filter [47].HPMR have several advantages compared to the conventional gas-phase evaporation method in which the process takes place in vacuum or under a reduced inert-gas pressure. This is because it can offer better reaction kinetics, and enhance impurity removal. The rapid quenching (10^6 K/s) is also able to produce materials in non-equilibrium phase.

Shao et al. [48] used HPMR to synthesize Mg_2Cu alloys, and studied the hydrogen absorption and PCI curves of the obtained Mg_2Cu. Mg (Cu) nano particles were produced by arc melting with ~50 g bulk metal (purity>99.5%) in a mixture of 50% Ar and 50% H_2 atmosphere of 0.1MPa. The arc plasma was generated in a voltage of 25V and a current of 200-300 A. A mixture of Mg and Cu nano particles in 2:1 molar ratio was then immersed in acetone and mixed by ultrasonic homogenizer for 30 minutes afterward. The metal mixture was pressed into pellets under a pressure of about 75 MPa for 30 s. The compressed pellets were crushed into some pieces for alloy synthesis. Thereafter, Mg_2Cu alloys were prepared following two different routes. One is annealed to 673 K under argon atmosphere (0.1 MPa), while the other is annealed under hydrogen atmosphere (4.0 MPa) [48].

In TEM observation, the average particle size of Mg_2Cu prepared by HPMR in argon is about 300 nm, and in high pressure hydrogen atmosphere it is about 100 nm. Figure 13 shows the hydrogen absorption of the obtained Mg_2Cu alloy annealed under hydrogen atmosphere. It shows that the sample prepared in hydrogen can absorb much hydrogen without any activation process at 523, 548, 573, 598 and 623 K under a starting hydrogen pressure of 3.0 MPa.

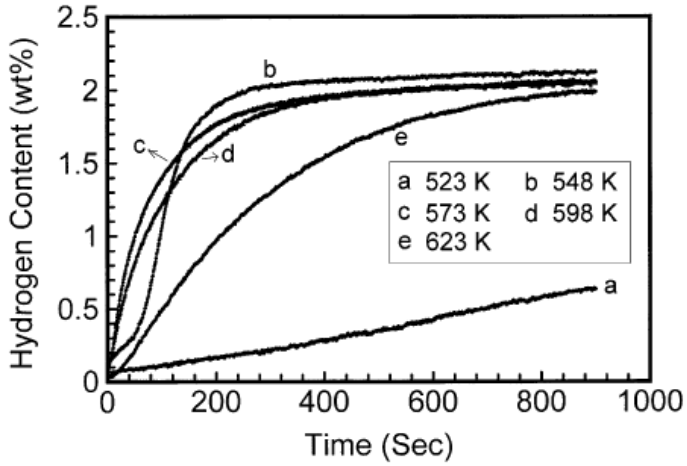

Figure 13 Hydrogen absorption curves of the nanostructured Mg_2Cu alloy under a starting hydrogen pressure of 3.0 MPa at 523, 548, 573, 598 and 623 K.

Vapor deposition

Chemical vapor deposition (CVD) is a chemical process which can produce high purity solid materials.

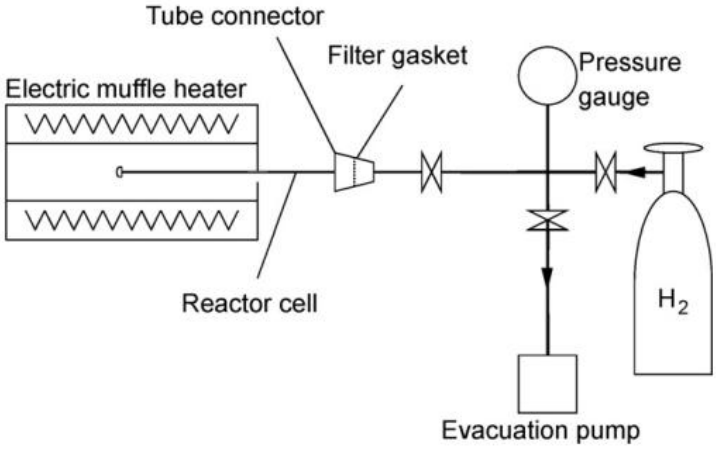

Figure 14 Scheme of CVD reactor

Take magnesium fiber produced by this method as an example [49]. The apparatus consist of an electric muffle furnace and a reactor tube. The synthesis was under 5 MPa hydrogen gas using Mg heated at 900 K. After the reactor was cooled naturally, it was detached from the gas line and transferred to a glove box filled with purified Ar. The sample synthesized was found to be pure MgH_2. After they measured the hydrogen absorption, they analyzed both the absorption kinetics of Mg powder and Mg fiber. The result is that the initial reaction rate of the Mg fiber was larger than that of the Mg powder. When temperatures are higher and pressures are lower, the reaction became close to the ideal nucleation and growth model, so hydride nuclei can keep generate on the Mg surface and grow three dimensionally.

Carbon nanotube is another ideal hydrogen storage materials, as nano structured materials have the unique features such as surface adsorption, inter- and intra-grain boundaries, as well as bulk absorption [50][51]. A report on hydrogen storage in carbon nanotubes by Dillon et al. [52] lead a worldwide research on carbonaceous.

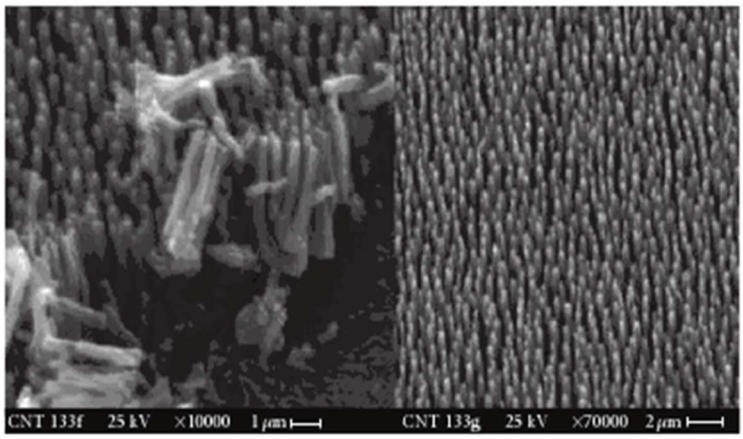

Figure 15 SEM micrographs of carbon nanotubes
grown by MPECVD

Microwave Plasma Enhanced Chemical Vapor Deposition (MPECVD) is a well-established method to grow carbon nanotubes [53], which can be used to produce carbon nanotubes for hydrogen storage materials with its advantage of processing at lower temperatures. As an example, Figure14 [54] shows the as-grown carbon nanotubes on a substrate using optimized processing conditions such as temperature, gas flow, gas concentrations and pressure.

Thermal plasma processing

As a method for processing powder and nano powder, thermal plasma synthesis is a relatively new method which is similar to the thin film deposition in concept. It is gaining momentum not only in research, but also in industrial applications. The temperatures in thermal plasma processing are sufficiently high to vaporize the starting material, and the supersaturation of vapour species forces the particle to condense, resulting in the production of extremely fine particles by homogeneous nucleation [55].

Çakmak et al. [56] did an experiment on synthesizing Mg-Ti with two different methods: mechanical milling and plasma synthesis. The starting powders were Mg (99.5%) and Ti (99.5%) with an average particle sizes (d_{50}) of 47 and 32 μm respectively. The volume ratio of Mg and Ti is 1:9.

MM was carried out in a planetary ball mill under argon atmosphere with 1 wt% graphite added as anti-sticking agent. The milling used 15 mm stainless steel balls and ball to powder ratio was 10:1. The milling speed was at 700 rpm and was programed have a 30 min rest time after every 30 min milling.

The thermal plasma processing of the powder mixture was carried out in an RF system that consists of a plasma torch, an RF generator, a powder feeding system, reaction chamber connected to a filter system and a vacuum pump. The plasma torch uses five turn induction coil, a water cooled ceramic tube with 36 mm inner diameter and another ceramic tube with 40 mm diameter that separates plasma gas from the sheath gas. Plasma gas was a mixture of Ar (15~23 slpm) and He (5~8 slpm) and sheath gas was Ar mixed with H_2 (4~5 slpm). Mixed powders were fed with a carrier gas He (6 slpm) and injected into the Ar-He plasma via a water cooled stainless steel probe. The probe was positioned axially into the torch down to the first turn of the coil. Reaction chamber, water cooled, was cylindrical in shape 200 mm in diameter and 1005 mm in length and contains viewing ports for *in-situ* process observations. The system and the reaction chamber were maintained at a pressure of 0.09 MPa. Where necessary, quenching was done by feeding He gas of 60 slpm at a position ~ 70 mm below the fifth (last) turn of the coil. The amount of powders processed in each experiment was typically 15 g. As a result, powders were collected from the wall of the reaction chamber instead of the filter system.

In comparison, they concluded that 1) mechanical milling yields large Mg aggolorates, with embedded Ti fragments uniformly distributed within the agglomerates. 2) Mg agglomerates that arise as a result of mechanical milling are made of coherently diffracting volumes of small size. 3) Plasma processing yields extremely small Mg powders of less than 100 nm. Both Mg and Ti do not dissolve in each other, and plasma processing yields relatively defect free crystals.

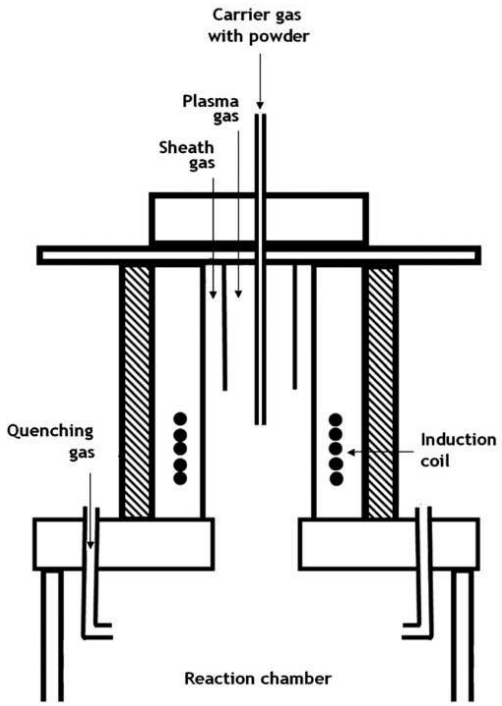

Figure 16 Schematic diagram of an RF plasma torch
used inthe synthesis of Mg-Ti nanopowders.

Spark plasma sintering

Spark plasma sintering is also known as field assisted sintering technique (FAST) or pulsed electric current sintering as a sintering technique.

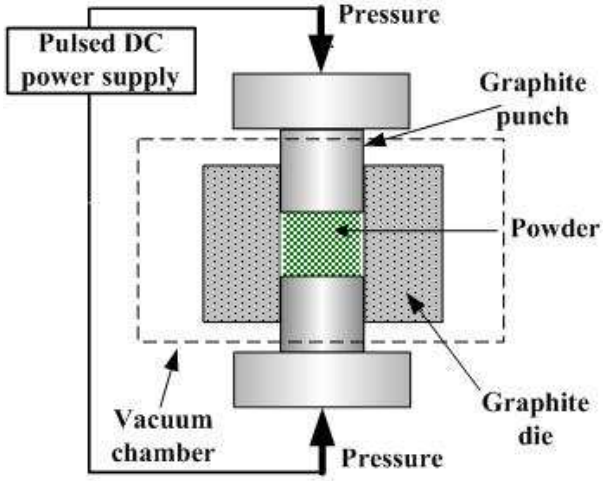

Figure 17 Spark Plasma Sintering (SPS)

The pulsed DC current directly passes through the graphite die and the powder compact. Not like the conventional hot pressing, where heat is provided by external heating elements, the heat is generated internally in SPS. Thus the heating or cooling rate is very high, which shortens the sintering process. This fast speed insures that during the densifying process, the powders are able to maintain nano size or nano structure while avoiding coarsening which accompanies standard densification routes.

Pei et al. [57] recently used SPS to prepare a laves phase related BCC solid solution alloy. $V_{35}(Ti, Cr)_{51}(Zr, Mn)_{14}$ was prepared by two methods: arc melting and SPS. For arc melting method, the alloy elements were arc melted under argon atmosphere based on the nominal chemical composition. For the SPS preparation, $V_{35}(Ti, Cr)_{65}$ BCC solid solution alloy and $ZrMn_2$ Laves phase alloy were mixed together evenly in the molar ration of 86:14 and then synthesized by SPS at a temperature of 1000 °C and pressure of 40 MPa.

After close inspection of the microstructures of both obtained alloy and examination of the hydrogen storage properties, they found that SPS could preserve the alloy with a large hydrogen storage capacity similar to the BCC solid solution single phase alloy, and maintain good activation and hydrogen absorption kinetic properties in the same time. They explained that the formation of sintered interface between the Laves phase and the BCC solid solution during SPS allows the Laves phase to contribute its intrinsic effects to the activation and kinetics properties of the alloys. Therefore they concluded that SPS is an efficient method for the preparation of Laves phase related BCC solid solution alloys [58].

Summary

Among the methods we have introduced above, we can see that many advanced materials were synthesized under non-equilibrium conditions. Rapid

solidification from the liquid state, mechanical alloying, vapor deposition, plasma processing, have all been receiving special attention due to their ability to produce meta-stable phases that undergo an “energizing and quenching” procedure (Figure 18 [28]).

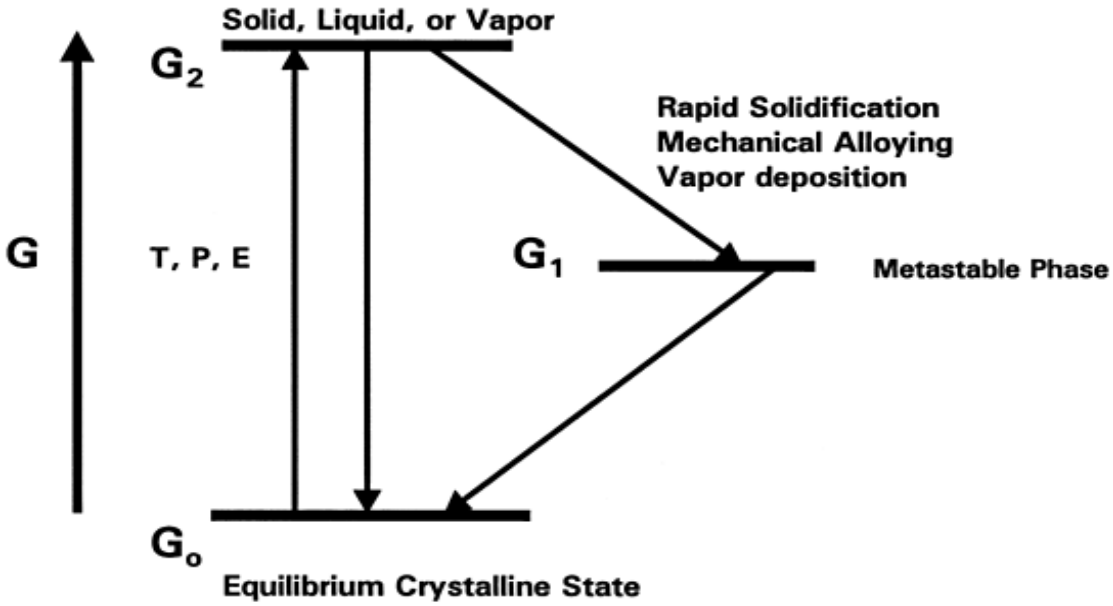

Figure 18 The basic concept of “energize and quench” to synthesize non-equilibrium materials.

Table 1. summarizes the energy gaps between equilibrium state and non-equilibrium state for different processing techniques.

Table 1 Departure energy from equilibrium state [59]

Technique	Maximum gap (kJ/mol)
Solid state quench	16
Rapid solidification	24
Mechanical alloying	30
Condensation from vapor	160

It should be noted that most advanced material synthesis method improve the activation and cycling properties of hydrogen storage materials, as hydrogen storage capacity is inherently limited by the theoretical capacity of the material itself.

Nowadays, new method for the preparation of hydrogen storage materials is developing to several directions: 1). modifying and improving existing processing method as there are many parameters and condition to adjust in the synthesis process that can influence the results significantly. 2). Combining the existing methods in the synthesis process, e.g, combustion synthesis and mechanical milling [60]. 3). Coating [61]. New methods of preparing hydrogen storage materials have never stopped being improved and discovered. Firstly, new materials which may need special preparation method are being found as suitable hydrogen storage candidates. Secondly, different methods to synthesize hydrogen storage materials bring about different physical and chemical properties, that in favor to improve general hydrogen storage performance.

REFERENCES

[1] Szajek, a.; Makowiecka, M.; Jankowska, E.; Jurczyk, M. J. Alloys Compd. 2005, 403, 323.

[2] Wu, C.; Bai, Y.; Yang, J.; Wu, F.; Long, F. Int. J. Hydrogen Energy 2012, 37, 889.

[3] Koh, G.; Zhang, Y.-W.; Pan, H. Int. J. Hydrogen Energy 2012, 37, 4170.

[4] Li, Q.; Chen, Y.; Lee, D. J.; Li, F.; Kim, H. Energy 2012, 38, 144.

[5] Singh, S. K.; Iizuka, Y.; Xu, Q. Int. J. Hydrogen Energy 2011, 36, 11794.

[6] Zhao, B.; Hu, H.; Yu, A.; Perea, D.; Haddon, R. C. J. Am. Chem. Soc. 2005, 127, 8197.

[7] Marco-Lozar, J. P.; Juan-Juan, J.; Suárez-García, F.; Cazorla-Amorós, D.; Linares-Solano, A. Int. J. Hydrogen Energy 2012, 37, 2370.

[8] Cuevas, F.; Korablov, D.; Latroche, M. Phys. Chem. Chem. Phys. 2012, 14, 1200.

[9] Huang AS, Bux H, Steinbach F, Caro J, ANGEWANDTE CHEMIE-INTERNATIONAL EDITION 2010, 49, 4958

[10] Jian-Yih Wang. Int. J. Hydrogen Energy 2009, 34, 3771.

[11] Srivastava, S.; Srivastava, O. N. J. Alloys Compd. 1998, 267, 240.

[12] Itoh, H.; Arashima, H.; Kubo, K.; Kabutomori, T. J. Alloys Compd. 2002, 330–332, 287.

[13] Cahn, R.W. Physical Metallurgy, Third edition, Elsevier Science Publishers B.V 1983.

[14] Ouyang, L.Z .; Qin, F.X. ; Zhu, M. ; Scr. Mater. 2006, 55, 1075.

[15] Ouyang, L.Z. ; Yang, X.S. ; Dong, H.W. ; Zhu M. Scr. Mater. 2009, 61, 339.

[16] OuYang, L.Z.; Yao, L. ; Yang, X.S. ; Li, L.Q. ; Zhu, M. Int. J. Hydrogen Energy 2010, 35, 8275.

[17] Tanaka, K. J. Alloys Compd. 2008, 450, 432.

[18] Wu, Y.; Han, W.; Zhou, S.X.; Lototsky, M.V.; Solberg, J.K.; Yartys V.A. J. Alloys Compd. 2008, 466, 176.

[19] Lin, H.J.; Ouyang, L.Z.; Wang, H.; Liu, J.W.; Zhu, M. Int. J. Hydrogen Energy 2012, 37,1145.

[20] Li, S.L.; Chen, W.; Luo, G.; Han, X.B.; Chen, D.M.; Yang, K.; Chen, W.P. Int. J. Hydrogen Energy 2012, 37, 3268.

[21] Zhong, C.; Chao, D.; Chen, Y.; Wang, W.; Zhu, D.; Wu, C. Electrochim. Acta 2011, 58, 668.

[22] Riabov, A.B.; Denys, R.V.; Maehlen, J.P.; Yartys, V.A. J. Alloys and Compd. 2011, 509, S844.

[23] Guo, PP.; Lin, YF.; Zhao, HH.; Guo, SH.; Zhao, DL.; J. Rare Earth 2011, 29, 574.

[24] Dong, XP.; Lu, FX.; Yang, LY.; Zhang, YH.; Wang, XL. Mater. Chem. Phys. 2008, 112, 596.

[25] Rożdżyńska-Kiełbik, B.; Iwasieczko, W.; Drulis, H.; Pavlyuk, V.V.; Bala, H. J. Alloys Compd. 2000, 298, 237.

[26] Liang, G.; Huot, J.; Boily, S.; Van Neste, A.; Schulz, R. J. Alloys Compd. 2000, 297, 261.

[27] Deng, C.; Shi, P.; Zhang, S.; Mater. Chem. Phys. 2006, 98, 514.

[28] Suryanarayana, C. Progress Mater. Sci. 2001, 46, 1.

[29] Zaluski, L.; Zaluska, A.; Ström-Olsen, J.O.; J. Alloys Compd. 1995, 217, 245.

[30] Simicic, MV.; Zdujic, M.; Jelovac, DM.; Rakin, PM. J. Power sources 2011, 92, 250

[31] Doi, K.; Hino, S.; Miyaoka, H.; Ichikawa, T.; Kojima, Y. J. Power Sources 2011, 196, 504.

[32] Staszewski, M.; Sierczyńska, A.; Kamińska, M.; Osadnik, M.; Czepelak, M.; Swoboda, P. J. Achiev. Mater. Manu. Engin. 2011, 44, 154.

[33] Liang, G.; Boily, S.; Huot, J.; Van Neste, A.; Schulz, R. J. Alloys Compd. 1998, 267, 302.

[34] Shang, C. X.; Bououdina, M.; Song, Y.; Guo, Z. X. Int. J. Hydrogen Energy 2004, 29, 73.

[35] Bobet, J.-L.; Akiba, E.; Darriet, B. Int. J. Hydrogen Energy 2001, 26, 493.

[36] Wang, J.-Y. Int. J. Hydrogen Energy 2009, 34, 3771.

[37] Bai, Y.; Wu, C.; Wu, F.; Yang, J.; Zhao, L.; Long, F.; Yi, B. Int. J. Hydrogen Energy 2012, 37, 12973.

[38] Akiyama, T.; Isogai, H.; Yagi, J. J. Alloys Compd. 1997, 252, L1.

[39] Wakabayashi, R.; Sasaki, S.; Saita, I.; Sato, M.; Uesugi, H.; Akiyama, T. J. Alloys Compd. 2009, 480, 592.

[40] Yasuda N.; Wakabayashi, R.; Sasaki, S.; Okinaka, N.; Akiyama, T. Int. J. Hydrogen Energy 2009, 34, 9122.

[41] Zhu, Y.; Liu, Y.; Gu, H.; Li, L. J. Alloys Compd. 2009, 477, 440.

[42] Liu, X.; Zhu, Y.; Li, L. J. Alloys Compd. 2006, 425, 235.

[43] Li, J.; Cheng, S.; Zhao, Q.; Long, P.; Dong, J. Int. J. Hydrogen Energy 2009, 34, 1377.

[44] Wada, N. Jpn. J. Appl. Phys. 1967, 6, 553.

[45] Wada, N. Jpn. J. Appl. Phys. 1968, 7, 1287.

[46] Wada, N. Jpn. J. Appl. Phys. 1969, 8, 551.

[47] Li, X.; Shao, H.; Liu, T. Tren. Nanotechnology. Res. p99.

[48] Shao, H.; Wang, Y.; Xu, H.; Li, X. J. Solid State Chem. 2005, 178, 2211.

[49] Matsumoto, I.; Asano, K.; Sakaki, K.; Nakamura, Y. Int. J. Hydrogen Energy 2011, 36, 14488.

[50] Baburaj, E. G.; Froes, F. H.; Shutthanandan, V.; Thevuthasan, S. Interfacial Chemistry and Engineering Annual Report, Pacific Northwest National Laboratory, Oak Ridge, Tenn, USA 2000.

[51] Schulz, R.; Boily, S.; Zalusky, L.; Zaluka, A.; Tessier, P.; Ström-Olsen, J. O. Innovations Metal. Mater. 1995, 529.

[52] Dillon, A. C.; Jones, K. M.; Bekkedahl, T. A.; Kiang, C. H.; Bethune, D. S.; Heben, M. J. Nature 1997, 386, 377.

[53] Costa, P. M.; Coleman, K. S.; Green, M. L. Nanotech 2005, 16, 512.

[54] Niemann, M. U.; Srinivasan, S. S.; Phani, A. R.; Kumar, A.; Goswami, D. Y.; Stefanakos, E. K. J. Nanomaterials 2008, 2008.

[55] Suresh, K.; Selvarajan, V.; Mohai, I. Vacuum 2008, 82, 482.

[56] Çakmak, G.; Károly, Z.; Mohai, I.; Öztürk, T.; Szépvölgyi, J. Int. J. Hydrogen Energy 2010, 35, 10412.

[57] Pei, P.; Song, X. P.; Liu, J.; Zhao, M.; Chen, G. L. Int. J. Hydrogen Energy 2009, 34, 8597.

[58] Froes, F. H.; Suryanarayana, C.; Russell, K.; Ward-Close, C. M.; Singh, J.; Copley, S. M. J. Singh and SM Copley 1994, 1.

[59] Suryanarayana, C.; Russell, K.; Li, C.-G. Mater. Sci. Engin. A 1995, 192, 612.

[60] Zhu, Y.; Yang, Y.; Wei, L.; Zhao, Z.; Li, L. J. Alloys Compd. 2012, 520, 207.

[61] Rao, D.; Lu, R.; Xiao, C.; Kan, E.; Deng, K. Chem. Commun. 2011, 47, 7698.

Appendix 2 Publications and conferences

Appendix 2 Publications and conferences

Publications:

Huang, L. W., Elkedim, Li, X. First principles investigation of scandium-based borohydride $NaSc(BH_4)_4$. Journal of Alloys and Compounds 536, Supplement 1, S546–S549 (2012).

X.D. Li, O. Elkedim, M. Nowak, M. Jurczyk, R. Chassagnon, Structural characterization and electrochemical hydrogen storage properties of $Ti_{2-x}Zr_xNi$ (x = 0, 0.1, 0.2) alloys prepared by mechanical alloying, Int. J. Hydrogen Energy. 38 (2013) 12126–12132.

X.D. Li, O. Elkedim, M. Nowak, M. Jurczyk, Characterization and first principle study of ball milled Ti–Ni with Mg doping as hydrogen storage alloy, Int. J. Hydrogen Energy. 39 (2014) 9735–9743.

B. Hosni, X. Li, C. Khaldi, O. ElKedim, J. Lamloumi, Structure and electrochemical hydrogen storage properties of Ti_2Ni alloy synthesized by ball milling, J. Alloys Compd. 615 (2014) 119–125.

X.D. Li, O. Elkedim, F. Cuevas R. Chassagnon, Structural and hydrogenation study on the ball milled TiH_2-Mg-Ni, Int J Hydrogen Energy. 40 (2015) 4212–4220.

Conferences:

LI, X. D., Elkedim O., Nowak, M., Chassagnon, R. & Jurczyk, The First European Early Stage Researchers' Conference on Hydrogen Storage: Structural characterization and electrochemical hydrogen storage properties of Ti_2Ni and $(Ti_{1-x}Zr_x)_2Ni$ (x=0, 0.05, 0.1) alloys prepared by mechanical alloying, oral presentation, 3-5th, Dec 2012, Belgrade, Serbia.

LI, X. D., Elkedim O, NANOSMAT-2013: $(TiNi)_{1-x}Mg_x$ (x = 0.06, 0.1, 0.2) alloys prepared by mechanical alloying for Ni-MH battery: experiments and

first principle calculations: oral presentation, 22-26th, Sept 2013, Granada, Spain.

LI, X. D., Elkedim O., Cuevas, F., Chassagnon, R, IDHEA, International Discussion on Hydrogen Energy and Applications: Micro-structure and electrochemical hydrogen storage properties of $(TiH_2)_{1.5}Mg_{0.5}Ni$ alloys prepared by mechanical milling, oral presentation, 12 - 14 May 2014 - Nantes Events Center.

Abstract:

Ni-MH (Nickel-Metal-Hydride) batteries have been a promising and extensively studied topic among clean and sustainable energy researches. Finding the ideal material for the negative electrode with high volumetric and gravimetric densities is the key to apply this technology on broader applications. Metal hydrides based on Ti-Ni have balanced properties between hydrogen capacity and electrochemical performances in cycling.

The objective of this thesis is to study the effects of element substitution/doping and mechanical alloying on the structural and hydrogen properties of Ti-Ni alloys. In this study, a series of Ti-Ni based systems with Mg or Zr doping/substitution have been systematically investigated.

The metallic compounds $(TiNi)_{1-x}Mg_x$, $(TiH_2)_{1.5}Mg_{0.5}Ni$, and $Ti_{2-x}Zr_xNi$ were synthesized by mechanically alloying from elemental powders. The milling time and effects of Mg, Zr substitution/doping were studied firstly in respect of their microstructures, using characterization techniques including XRD, SEM, TEM (EDX support), followed by the hydrogen properties measurements of the samples by hydrogen solid-gas reaction and electrochemical cycling.

A first principle calculation tool based on DFT (Density Functional Theory) was carried out to further investigate the enthalpy of formation in order to compare the thermodynamical stability of the obtained compounds. In the study, we have found the alloying priorities in the ternary alloys Ti-Ni-Mg and Ti-Ni-Zr under milling conditions.

A structure transformation of Ti to FCC induced by foreign elements is reported and investigated. Enthalpies of formation per atom of the compounds were obtained by DFT calculations, which helped interpret the experimental results.

PCI (Pressure Composition Isotherms) curves and discharge capacities as the function of cycling numbers revealed the hydrogen properties of the obtained compounds, including TiNi, Ti_2Ni (amorphous), Ti-Mg and Ti-Zr.

KEY WORDS: Ni-MH batteries, Ti-Ni, Metal hydrides, Mechanical alloying, Electrochemical hydrogen storage, DFT

Résumé :

Les accumulateurs Ni-MH (Nickel-Métal-Hydrure) sont un sujet prometteur et largement étudié dans les recherches d'une énergie propre et durable. Trouver le matériau idéal pour l'électrode négative à haute densité volumétrique et gravimétrique est la clé pour l'application de cette technologie. Les hydrures métalliques à base de Ti-Ni ont des propriétés équilibrées entre la capacité d'hydrogène et les performances électrochimiques.

L'objectif de cette thèse est d'étudier les effets de substitutions/additions d'éléments et de la mécanosynthèse sur la structure et les propriétés d'hydrogène des alliages Ti-Ni. Dans cette étude, une série d'alliages à base de Ti-Ni avec des substitutions/additions de Mg ou de Zr ont été systématiquement étudiés.

Les alliages $(TiNi)_{1-x}Mg_x$, $(TiH_2)_{1.5}Mg_{0.5}Ni$, and $Ti_{2-x}Zr_xNi$ ont été synthétisés par mécanosynthèse à partir de poudres élémentaires. Dans un premier temps, l'influence du temps de broyage et les effets de substitutions/additions sur les microstructures ont été caractérisés par des techniques telles que la DRX, le MEB et le MET. Dans un second temps, les propriétés d'hydrogénation des différents alliages ont été mesurées par des réactions solid-gaz et par cyclage électrochimique.

La théorie de la fonctionnelle de la densité (DFT) en utilisant le programme CASTEP a permis de calculer les enthalpies de formation afin de comparer la stabilité thermodynamique des alliages obtenus. Dans ces travaux de recherche, nous avons identifié les priorités d'alliage des ternaires Ni-Ti-Mg et Ti-Ni-Zr dans des conditions de broyage. La transformation structurale du Ti en phase CFC, induite par l'introduction d'éléments étrangers, a été mise en évidence.

Les courbes PCI (Pression-Composition-Isothermes) et les capacités de décharge en fonction du nombre de cycles indiquent les propriétés d'hydrogène des alliages obtenus, y compris TiNi, Ti2Ni (amorphe), Ti-Mg et Ti-Zr.

MOTS CLES : Accumulateurs Ni-MH, Ti-Ni, Hydrures métalliques, Mécanosynthèse, Stockage d'hydrogène électrochimique, DFT

SPIM

■ École doctorale SPIM - Université de Technologie Belfort-Montbéliard
F - 90010 Belfort Cedex ■ tél. +33 (0)3 84 58 31 39
■ ed-spim@univ-fcomte.fr ■ www.ed-spim.univ-fcomte.fr

utbm université de technologie Belfort-Montbéliard